BERGISCHE UNIVERSITÄT
WUPPERTAL

Fakultät für Elektrotechnik, Informationstechnik und
Medientechnik

Stimulated Emission and Lasing in Metal Halide Perovskites by Direct Thermal Nanoimprint

zur Erlangung des akademischen Grades eines Doktors der
Ingenieurwissenschaften (Dr.-Ing.) genehmigte
Dissertation von

M.Sc. Neda Pourdavoud

Referenten:
Prof. Dr. rer. nat. Thomas Riedl
Prof. Dr.-Ing. Hella-Christin Scheer

Mündliche Prüfung am: 19.06.2020

The PhD thesis can be quoted as follows:

urn:nbn:de:hbz:468-20200924-085950-5
[http://nbn-resolving.de/urn/resolver.pl?urn=urn%3Anbn%3Ade%3Ahbz%3A468-20200924-085950-5]

DOI: 10.25926/b4j1-zj06
[https://doi.org/10.25926/b4j1-zj06]

Acknowledgments

First of all, I want to thank almighty God who has taken care of me every moment; who has provided me with the best opportunities, who has supported me whenever I was in need, and who has been my best friend since I was born.

I would like to thank my doctoral supervisor Prof. Dr. rer. nat. Thomas Riedl for giving me the opportunity to carry out my Ph.D. thesis; for being available whenever I have needed help, for supporting me beyond research activities, and for sharing his outstanding knowledge and experiences with me.

I also want to give a special thanks to Prof. Dr.-Ing. Hella-Christin Scheer, and Prof. Dr.-Ing. Patrick Görn for their constructive advice throughout my Ph.D research.

Furthermore, I really appreciate my current and former colleagues, in the chair of Electronic Devices and the chair of Large Area Optoelectronics, namely K. Kraus, E.-M. Grimberg, Dr.-Ing S. Trost, Dr.-Ing. R. Heiderhoff, Dr.-Ing. D. Theirich, K. Brennecke, Dr.-Ing. A. Mayer, Dr.-Ing. S. Wang, Dr.-Ing. A. Behrendt, Dr.-Ing. A. Räupke, Dr.-Ing. K. Zilbeberg, Dr.-Ing. A. Polywka, Dr.-Ing. M. Fakhri, Dr.-Ing. L. Hoffmann, T. Häger, K. O. Brinkmann, I. Shutsko, M. Buchmüller, T. Becker, M. Theisen, C. Tückmantel, T. Gahlmann, M. Runkel, E. Shkura, T. Hasselmann, A. Henkel, T. Jakob, M. Leifels, M. Wolter, P. Teckhausen, M. Prior, J. Rond, and J. Staabs. I would like to thank them all for their helpful discussions; for providing me with a great atmosphere in both the laboratory and the office, and helping me to become familiar with Germany as an international student.

My warmest thanks also to our visiting scientists Dr. T. Hu, Dr. J. Zhao, and Dr. J. He from China, and C. Kocak from Turkey for their fruitful cooperation.

My special thanks to our project partner in Technische Universität Braunschweig; Prof. Dr. Wolfang Kowalsky, Dr. rer. nat. H. –H. Johannes, A. Marianovich, M. Cehovski, and Quacef Charfi.

I also want to express my gratitude to Prof. Dr. K. Meerholz, Dr. S. Olthof, Prof. Dr. rer. nat. Lützenkirchen-Hecht, Dr. D. Rogalla, Dr. A. L. Giescke, Dr. P. J. Cegielski, Prof. Dr.-Ing. M. C. Lemme, Dr. Stefan Zaeffer, Prof. Dr. Y. Vaynzof, D. Becker-Koch, Dr. S. Suckow, Dr. I. Päschke, J.-C. Gasse, and Prof. Dr. M. Koch for providing me with essential measurements and simulation data.

I acknowledge the German Federal Ministry for Education and Research (Grant No. 13N13819) and the DFG (Deutsche Forschungsgemeinschaft) (Grant No. RI1551/9-1) for financial support

Finally, my extraordinary thanks to my family, especially my parents to whom I owe all my success, and achievements in life, and also to my sisters Parastoo and Maryam and my dear niece Melika. They have always been supportive and encouraging during my Ph.D. research.

Wuppertal, May 04, 2020

Neda Pourdavoud

Contents

Abbreviations and Symbols

Symbols

α	Absorption coefficient	1/cm
E_g	Bandgap energy	eV
η	Photoluminescence quantum yield	
η_{ext}	External photoluminescence quantum yield	
η_{int}	Internal photoluminescence quantum yield	
h	Planck's constant	J.S
k	Extinction coefficient	
λ	Wavelength	nm
Λ	Grating's periodicity	nm
μ	Octahedral factor	
m	Bragg diffraction's order	
ν	Photon's frequency	Hz
n	Refractive index	
n_{eff}	Effective refractive index of the optical laser mode	
n_{med}^{eff}	Refractive index of the effective medium	
n_p	Refractive index of perovskite	
n_{air}	Refractive index of air	
P_{out}	Outcoupling probability	

r	Radius	
Å	Angstrom	
R_{diff}	Diffuse reflectance	%
R_{total}	Total reflectance	%
τ_{PL}	PL-lifetime	ns
T	Transmittance	%
f	Goldschmidt tolerance factor	

Abbreviations

AFM	Atomic Force Microscopy
AlGaInP	Aluminium Gallium Indium Phosphide
ASE	Amplified Spontaneous Emission
Br	Bromine
BZ	Brillouin Zone
$CaTiO_3$	Calcium Titanium Oxide
CdSe	Cadmium Selenide
CD	Compression Direction
$CH_3CH_2NH_3^+$	Ethylammonium ion
$CH_3NH_3^+$	Methylammonium ion
$CH_3NH_3PbBr_3$	Methylammonium Lead Bromide
$CH_3NH_3PbI_3$	Methylammonium Lead Iodide
Cl	Chlorine
Cs	Caesium
CsBr	Caesium Bromide
$CsPbBr_3$	3D-Caesium Lead Bromide

$CsPb_2Br_5$	2D-Caesium Lead Bromide
CW	Continuous Wave
DBR	Distributed Bragg Reflector
DFB	Distributed Feedback
DMF	Dimethylformamide
DMSO	Dimethylsulfoxide
DOS	Density of States
EA	Ethylammonium
EBSD	Electron Backscatter Diffraction
$FAPbI_3$	Formamidinium Lead Iodide
FDTD	Finite Difference Time Domain
FWHM	Full Width at Half Maximum
GaAs	Gallium Arsenide
GaN	Gallium Nitride
GBL	γ-butyrolactone
$HC(NH_2)_2^+$	Formamidinium ion
$HC(NH_2)_2PbI_3$	Formamidinium Lead Iodide
I	Iodine
InGaN	Indium Gallium Nitride
ITC	Inverse Temperature Crystallization
K	Potassium
LED	Light Emitting Diode
MA^+	Methylammonium ion
$MAPbBr_3$	Methylammonium Lead Bromide
$MAPbI_3$	Methylammonium Lead Iodide
NC	Nano Crystal
NIL	Nanoimprint Lithography
OD	Optical Density

Pb	Lead
$Pb(Ac)_2.3H_2O$	Lead Acetate Trihydrate
PbX_2	Lead Halide
PC	Photonic Crystal
PHP	Planar Hot Pressing
PL	Photoluminescence
PLQY	Photoluminescence Quantum Yield
QD	Quantum Dot
QW	Quantum Wire
Rb	Rubidium
RBS	Ratherford Bckscattering Spectrometry
SEM	Scanning Electron Microscopy
Si	Silicon
Sn	Tin
TE	Transverse Electric Mode
TEM	Transmission Electron Microscopy
THz	Terahertz
TOPO	Tri-n-octylphosphine
TRPL	Time-Resolved Photoluminescence
VCSEL	Vertical Cavity Surface Emitting Laser
V_{OC}	Open Circuit Voltage
XRD	X-ray Diffraction
ZnO	Zinc Oxide

Chapter 1

Introduction

The laser, standing for light amplification by stimulated emission of radiation, was first demonstrated by Maiman in 1960, and after passing a long way, today lasers are applicable in almost every science field such as medicine, research, telecommunications, astronomy, robotics, and even military systems respecting their highly coherent, focused, monochromatic, and directional emitted light.

Generally, a laser is composed of three fundamental elements:

1. The gain medium which can be made of different materials such as liquids, gases, solids, or semiconductors, and it is considered as part of the laser where specific optical waves get amplified through stimulated emission of radiation.
2. The pump source that can be optical, electrical, or chemical, and it provides energy to the gain medium.
3. The resonator which supplies the feedback of light.

Among all types of lasers, semiconductor lasers (laser diodes) have become the most promising class of lasers because of:

1. The possibility of electrical pumping with moderate voltages and achieving high efficiency.
2. The tunability of wavelength from near-ultraviolet to mid-infrared.
3. The compactness in size which leads to fast switching and optical power modulation.
4. Easy integration.

These laser diodes are based exclusively on epitaxially produced monocrystalline inorganic layer systems, but large processing costs associated with high temperatures, the use of costly coating systems, inflexibility, brittleness, and limitation in wavelength tunability are their significant disadvantages.

By contrast, organic materials considering their noticeable features such as high photoluminescence quantum efficiency, flexibility, simple fabrication, low cost in terms of both material and processing, easy tuning of chemical structures, and optimizing electrical and optical properties have become an attractive candidate as gain medium over the last decades. However, due to exciton and carrier induced losses, the electrically pumped organic laser diodes haven't been actualized yet.

Recently, the class of organometal halide and all-inorganic perovskite semiconductors have emerged as highly interesting and inexpensive active material for tunable thin-film lasers. For lasing applications, there is the vision that these perovskites may overcome the typical limitations and loss mechanisms imposed by organic gain media [1-3].

Moreover, by varying the organic/inorganic cation, metal or halide components, their band gap and thus their emission spectrum can be shifted over a broad spectral range. For example, semiconductor lasers in the green/yellow/orange wavelength region are of great interest, as established laser diodes (based on Indium Gallium Nitride (InGaN) etc.) experience severe limits in this spectral window.

Furthermore, these perovskites can be prepared by a number of facile and low-temperature techniques such as solution processes. Thus, these interesting perovskite

semiconductors seed new promises for the realization of an electrically operated diode laser prepared from a solution at low temperatures.

Up until now, optically pumped lasing has been reported for single crystalline perovskite nanowires [4, 5], and platelets [6], which form natural High-Q Fabry–Perot or whispering gallery mode resonators, respectively. Vertical cavities [7], micro-spherical silica resonators [8], and distributed feedback structures [9, 10] have been also considered. However, for the realization of High-Q photonic resonator structures and waveguides, the perovskite active material needs to be patterned on the nanoscale with utmost control. When the work of this thesis started, the tremendous potential of metal halide perovskites for optoelectronic and photonic applications had not been unlocked partially because of the lack of suitable versatile nanopatterning techniques, to create resonator structures, waveguides, etc. with a maximum level of control and precision directly into perovskite layers.

In this work, the above mentioned issues are addressed and it is demonstrated for the first time that photonic nanostructures can be prepared by thermal nanoimprint lithography (NIL) directly into different types of perovskite at temperatures as low as 100 °C—a futile endeavour in case of established inorganic semiconductors like Gallium Arsenide (GaAs) or Gallium Nitride (GaN).

After giving a brief description about the physics of perovskite semiconductors and their optoelectronic properties in **Chapter 2**, in **Chapter 3**, it is presented that perovskites which typically consist of nanocrystals (NCs) on the order of 100 nm are prone to defects that can severely affect the performance of devices based on these perovskites. Moreover, I demonstrate how the presence of defects/trap states can result in phenomena called fluorescence intermittency. The noticeable finding of my studies is that this fluorescence intermittency is observed for remarkably large NCs by the sizes of around 100 nm. It is shown that by increasing the size of perovskite NCs and illumination intensity, this fluorescence intermittency can be eliminated which shows the importance of the grain sizes of perovskite material which is applied for example as laser medium. It brings me to the point that for achieving perovskite-based lasers with low threshold lasing, one of

the most important parameters which should be taken into account is the size of the perovskite grains and the overall crystal quality.

In **Chapter 4**, the direct thermal imprinting of methylammonium lead iodide ($MAPbI_3$) perovskite active materials is shown. Thereby, 2D photonic crystals are patterned into the $MAPbI_3$ perovskite at a temperature as low as 100 ^oC for the first time. Interestingly, the imprint process decreases the number of surface defects, smoothens the perovskite surface, and also increases the perovskite grain sizes. The patterned $MAPbI_3$ supports lasing with a low threshold of 3.8 $\mu J/cm^2$ at room temperature.

As it has been difficult to fabricate InGaN-based laser diodes at room temperature in the spectral region known as the "green gap" in **Chapter 5**, I use thermal imprint for methylammonium lead bromide ($MAPbBr_3$), which has a bandgap in the green spectral regions, larger than that of $MAPbI_3$. Linear photonic gratings with periodicity of 300 nm are imprinted directly into $MAPbBr_3$, which result in the first directly imprinted $MAPbBr_3$-based Distributed Feedback (DFB) lasers with very low lasing thresholds of 3.4 $\mu J/cm^2$. In addition, in this chapter, a planar hot pressing process (PHP) is introduced, for which a flat silicon stamp is used during imprint.

As methylammonium (MA^+) is a volatile cation, MA-based perovskites lack intrinsic stability. To improve the stability, MA can be replaced by inorganic cations such as caesium (Cs^+). However, due to high defect density, and poor film formation resulting in a very low photoluminescence quantum yield (PLQY), there hasn't been any report showing Amplified Spontaneous Emission (ASE), and lasing in caesium lead halide ($CsPbX_3$) perovskite thin films at room temperature. In contrast to $CsPbX_3$ thin films, $CsPbX_3$ nanoparticles showed high PLQY and ASE at room temperature, which nurtured the paradigm that for efficient light emission from lead halide perovskites at room temperature, one needs to confine the charge carriers/excitons on the nanometer scale to prevent their migration to non-radiative defects. However, in **Chapter 6**, by applying my NIL process, I challenge this paradigm, and present the first caesium lead bromide thin-film DFB and vertical cavity surface emitting lasers (VCSELs) with ultralow threshold at room temperature which do not rely on the use of nanoparticles.

In **Chapter 7**, the conclusion to the main part and outlook for future research are presented.

Chapter 2

Basics of Perovskite Semiconductors and DFB Lasers

2.1. Perovskite structure

Perovskite semiconductors discussed in this thesis share the same type of crystal structure as calcium titanium oxide ($CaTiO_3$). It takes its name from $CaTiO_3$ mineral which is discovered in the Ural Mountains of Russia by Gustav Rose in 1839 and was named after the mineralogist L. A. Perovski (1792-1856). In general, perovskites have a crystalline structure with the chemical formula ABX_3, where A and B represent cations, and X indicates an anion. The perovskite crystal structure, as it is shown in **Figure 2.1.1**, consists of corner sharing BX_6 octahedra with a cation, situated in cubooctahedral interstices. Although plenty of A, B, and X ions can be incorporated into a perovskite structure resulting in an extensive variety of compounds, there are parameters such as the Goldschmidt tolerance factor, and octahedral factor which can be used to predict the formability, and stability of these perovskite compounds.

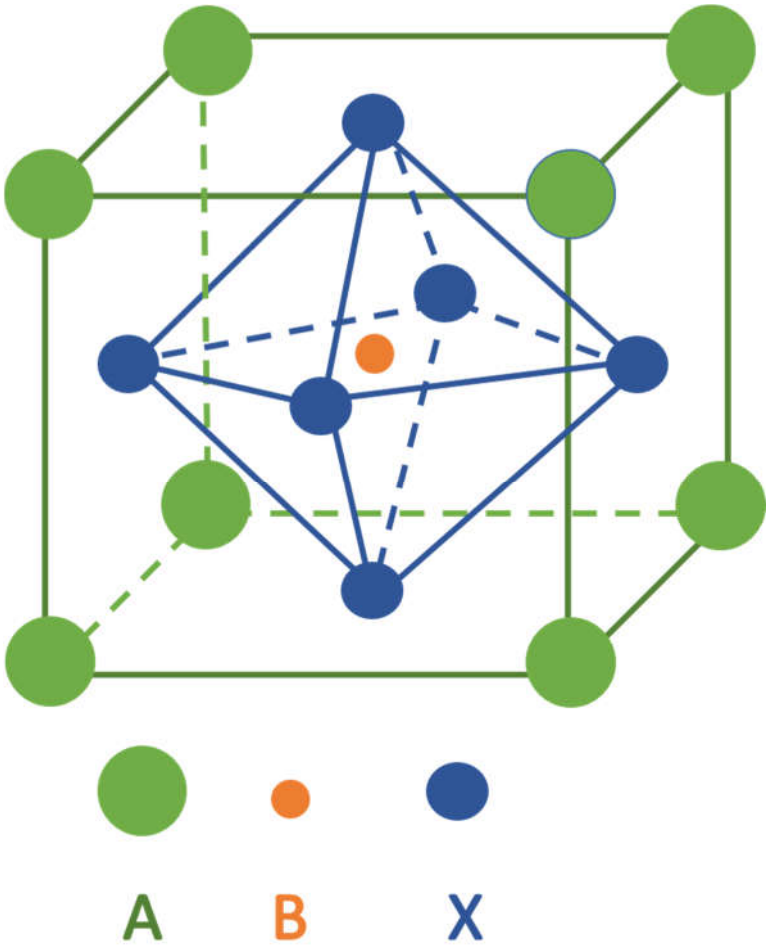

Figure 2.1.1. *Perovskite crystal structure.*

Goldschmidt tolerance factor (f)

In order to determine the stability and the distortion of the perovskite structure, the Goldschmidt tolerance factor (f) as a reliable empirical index can be applied:

$$f = \frac{r_A + r_X}{\sqrt{2}(r_B + r_X)} \qquad \textbf{2.1.1}$$

Where r_A, r_B and r_X represent the ionic radii of the A, B cations, and the X anion, respectively [11]. In ideal conditions, and in case of a 3D perovskite, when A, and B have ideal sizes, t falls between 0.9 and 1, and the perovskite has its cubic structure. When A

gets too small to fit into cubo-octahedral voids, the BX_6 octahedra tilts gradually to fill the voids, and the perovskite structure changes from cubic into orthorhombic, or rhombohedral ($0.8 < t < 0.9$). When t goes below 0.8, which happens when the A, and B cations have similar sizes, structures other than perovskite are formed. For too big A cations or too small B cations, hexagonal or tetragonal perovskite structures are formed.

Octahedral factor (μ)

Aside from the Goldschmidt tolerance factor, the octahedral factor could also be taken into consideration for investigating the stability of the BX_6 octahedron:

$$\mu = \frac{r_B}{r_X} \qquad \textbf{2.1.2}$$

The formation of a stable perovskite is possible when the octahedral factor is in the range of 0.442 to 0.895 [12, 13].

Considering both the Goldschmidt tolerance factor, and the octahedral factor, a parameter space (which will be explained later in **Section 2.2.2**) can be provided, with that perovskite formability, and stability can be characterised.

2.2. Metal halide perovskite

2.2.1. Introduction

In the past few years, metal-halide perovskite semiconductors have become of tremendous interest for a variety of optical applications regarding their fascinating features, including optical and electrical properties (high absorption coefficient, sharp optical band edge, low non-radiative emission, long carrier diffusion length, high carrier mobility, and etc.), low cost and abundance, and facile preparation at low temperature

which is favourable for flexible devices. Respecting these intriguing properties, these perovskites have been researched intensively over the last few years, and it is believed that this class of materials could revolutionise the world of both solar cells and light emitting devices. Considering the solar cell sector, in 2013, Science magazine rated these perovskite-based solar cells one of the year's top breakthroughs, and recently, just a few years after achieving an efficiency of only 3.8% in 2009 [14], solar cells based on a representative of this family have been certified with an efficiency of 25.2% [15], while it took more than 20 years for silicon-based photovoltaics to reach an efficiency over 20% [16].

Aside from their remarkable success in photovoltaics, metal-halide perovskites are likewise considered as highly promising for light emission, e.g. light emitting diodes (LEDs) or lasers [17-19]. LEDs based on the fruit-fly of these compounds, i.e. methyl-ammonium lead iodide ($CH_3NH_3PbI_3$ or $MAPbI_3$), and other related perovskites have been demonstrated and their efficiency is increasing rapidly [20, 21]. For lasers, there is the vision that these perovskites may overcome/avoid the typical limitations and loss mechanisms imposed by organic gain media, i.e. triplet-singlet annihilation or absorption due to triplet excitons and polarons [1-3]. As such, this class of perovskites are currently considered as an excellent candidate to actualize solution-processed electrically operated laser diodes on virtually any substrate. Perovskite lasers also bear the potential to cover the spectral region between 530-610 nm, known as the "green-gap" [22], which is difficult to address at room temperature with established inorganic semiconductor gain media, such as InGaN or aluminium gallium indium phosphide (AlGaInP).

2.2.2. Metal halide perovskite compounds

Like $CaTiO_3$, the general formula of a metal halide perovskite is ABX_3, where the A site is occupied by organic/inorganic cations such as methylammonium ($CH_3NH_3^+$, MA^+), formamidinium ($NH_2HCNH_2^+$, FA^+), ethylammonium ($CH_3CH_2NH_3^+$, EA^+), potassium (K^+), rubidium (Rb^+), and caesium (Cs^+), B is a divalent metal cation like lead (Pb^{2+}), and tin (Sn^{2+}), and X is a halide anion namely iodide (I^-), bromide (Br^-), and chloride (Cl^-).

The defined parameter space (discussed in **Section 2.1**) for metal halide perovskite compounds is presented in **Figure 2.2.2.1**, to determine their formability, and stability.

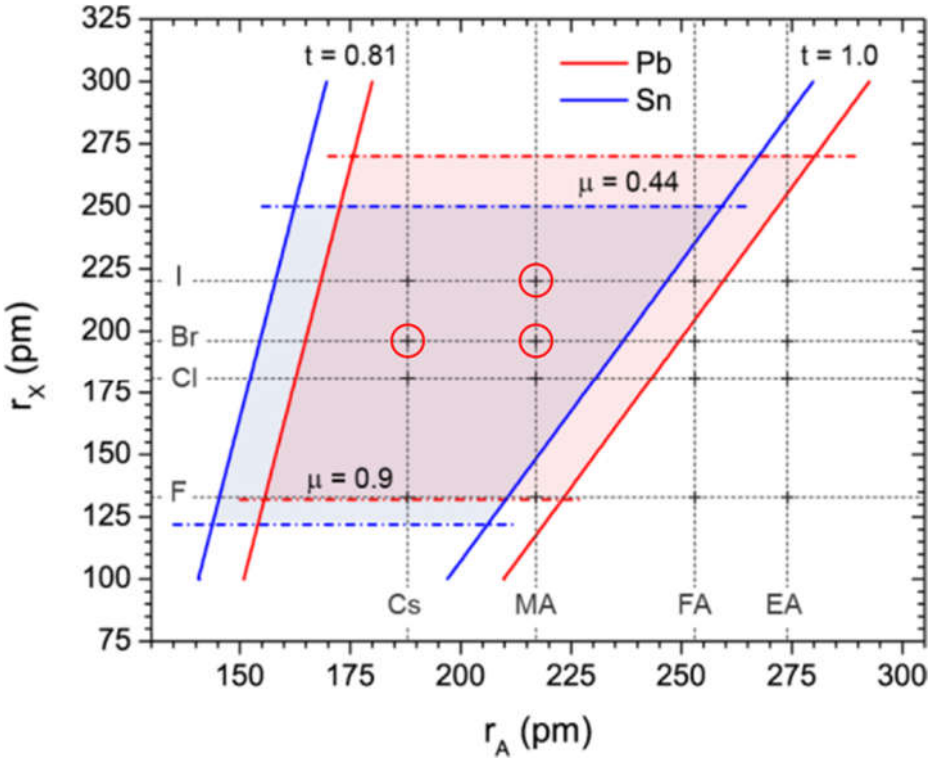

Figure 2.2.2.1. *Formability of 3D lead (red) and tin (blue) halide perovskites as a function of A-site cation and halide anion radii. Solid and dashed lines mark the bounds of the tolerance and octahedral factors, respectively [23]. Perovskite compounds used in this study are marked with the red circles.*

Depending on the A site which is occupied by either organic or inorganic cations, metal halide perovskites are divided into two different categories: organometal halide perovskites and all-inorganic metal halide perovskites.

Note, although this group of perovskites can be formed in different dimensionalities (3D, 2D, 1D, and 0D), in this work, I focus mainly on 3D perovskites. Therefore, when I talk about perovskite without pointing its dimension, I mean 3D perovskite, otherwise the dimension will be mentioned.

2.2.3. Metal halide perovskite deposition

The plethora of deposition methods such as one-step solution process, sequential deposition (two-step deposition), vacuum evaporation, coating and printing, and etc. have been reported for forming metal-halide perovskite compounds [24-30], some of which will be introduced in the following.

***One-step solution process**:*

In the one-step solution process, the precursors are dissolved in a same polar solvent such as dimethylformamide (DMF), Dimethylsulfoxide (DMSO), γ-butyrolactone (GBL), or a mixture of them, and spin-coated on selected substrates. After spin-coating, the layer should be post-annealed on a hotplate for evaporation of solvent and final crystallization of the perovskite film. The spin-coating parameters and the temperature and time of post-annealing can differ depending on the precursor composition and the solvent.

Although spin-coating is considered to be a facile and low cost process at low temperatures - it seems to be difficult to have control over the crystallisation. This is because it can be affected by various factors such as: the initial composition, the type of solvent, the spin-coating, the post-annealing parameters, the substrate surface, and the environment. This can lead to rough, and inhomogeneous perovskite formation as well as poor surface coverage and non-uniform thicknesses [31-37]. To tackle these issues, two methods including solvent engineering, and adding additives have been reported [24, 38-41].

Vapor deposition:

Vacuum thermal evaporation is an excellent method to obtain smooth and uniform perovskite films on large areas, especially for all-inorganic perovskites such as caesium lead bromide ($CsPbBr_3$), where the low solubility of caesium bromide (CsBr) in solvent results in poor surface morphology and coverage [42, 43].

Compared to the solution process method, by vapor deposition, the thickness of the perovskite film can be controlled more precisely. Moreover, vapor deposition paves the

way for forming perovskite heterostructures over a large area. However, the molar ratio of the two components needs to be precisely optimized.

Single crystal

The majority of perovskite devices have been based on polycrystalline thin films prepared through solution deposition methods. These polycrystalline films suffer extremely from surface defects, grain boundaries, and voids. Moreover, as small variations in the deposition conditions can have notable influence on the size of the crystallites, the layer morphology, and defects, which significantly change electrical and optical properties, these polycrystalline layers make the study of intrinsic properties of perovskite materials difficult. For tackling these obstacles, defect-free single crystals can be an ideal candidate.

Despite polycrystalline films, single crystals based on perovskite materials have been considered to possess remarkably low trap-state densities, long-carrier diffusion, and large absorption coefficients which mark them as a favourable semiconductor for optoelectronic applications [44-49]. Moreover, the methods used for perovskite single crystals' growth are fast and shape-controllable [44], which is essential for device applications. These perovskite single crystals can be grown by different methods, such as cooling the saturated precursor solutions [45, 46], anti-solvent diffusion [47], and inverse temperature crystallization (ITC) [48, 49].

2.2.4. Bandgap tuning

One of the most noticeable advantages of perovskites over other semiconductors is their bandgap tunability by chemical management applying facile, and cost-effective deposition methods such as solution process [50-52]. By tuning the bandgap, LEDs and lasers with tunable emission wavelengths, and colourful solar cells can be fabricated. Furthermore, there is a possibility to combine large bandgap perovskite solar cells with small bandgap ones in a tandem structure to get higher efficiencies. By substituting the A, B, and X ions, the perovskite emission wavelength can be tuned between around 350

nm to 1200 nm where the A site can be filled by cations such as FA^+, MA^+, Cs^+, or Rb^+. Pb^{2+}, or Sn^{2+} can sit in B cation sites, and the X anion is occupied by halogens such as I^-, Br^-, or Cl^-. Different cations and anions can also be incorporated together to tune the bandgap (for example in $MAPb_{1-x}Sn_xI_3$, the B cation is filled by a mixture of Pb and Sn) more precisely, but they should be combined by an appropriate ratio to make sure that perovskite structure will not be distorted (referring to Goldschmidt tolerance, and octahedral factors).

X anion substitution

The most prevalent substitution, having the most significant influence on optical properties of halide perovskites, is the exchange of the X anion. By only varying the halide anion from iodine to bromine and then chlorine (**Figure 2.2.4.1**), the absorption onset can be shifted from red, to green and finally to the blue region [50, 52- 54].

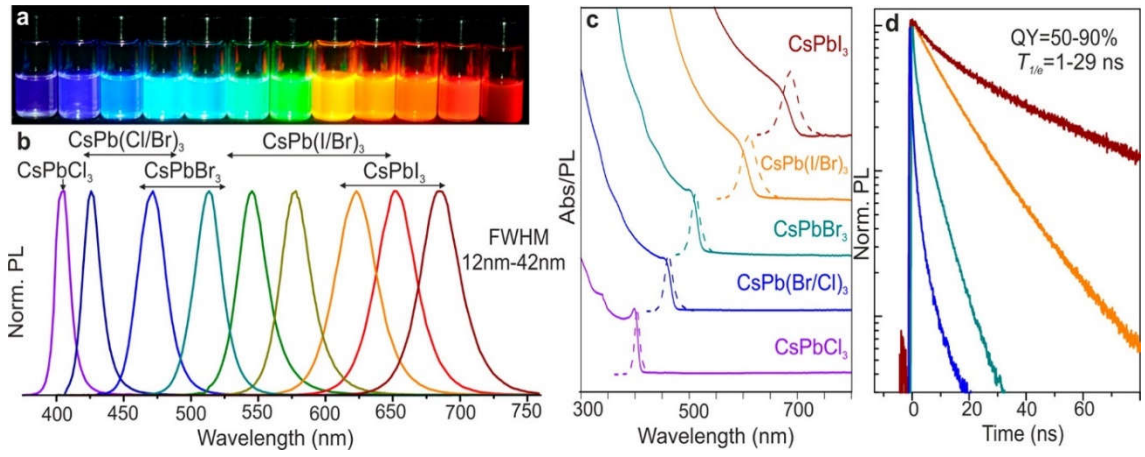

Figure 2.2.4.1. *Colloidal perovskite $CsPbX_3$ NCs (X = Cl, Br, I) exhibit composition-tunable bandgap energies covering the entire visible spectral region with narrow and bright emission: a) Colloidal solutions in toluene under UV lamp (λ = 365 nm); b) representative PL spectra (λ_{exc} = 400 nm for all but 350 nm for $CsPbCl_3$ samples); c) typical optical absorption and PL spectra, and d) time-resolved PL decays for all samples shown in (c) except $CsPbCl_3$ [50].*

B cation substitution

Generally, perovskite compositions are based on Pb^{2+} as B cation. However, on the one hand, the toxicity of Pb^{2+}–based perovskites prevents the practicality of perovskite-based devices, and on the other hand, they show poor response over 838nm, which prevents further efficiency increase of perovskite-based solar cells. For solving the issues related to toxicity and bandgap limitation of lead-based perovskites, Sn^{2+} can be a good candidate to replace Pb^{2+} [55].

A cation substitution

MA is the most common cation which fills the A sites in perovskite compounds. However, as MA is volatile, MA-based organic-inorganic halide perovskites have been considered to lack intrinsic stability, and devices based on this class of perovskites are prone to degradation over exposure to humidity, oxygen, heat, light, and etc., which substantially compromises their serious application [52, 56-60]. Moreover, MA-based perovskites, regarding their bandgap of 1.55 eV, restrict light absorption to wavelengths up to 800nm. To tackle stability issues and to lower the bandgap, the MA moiety can be replaced with cations such as FA [61, 62], Cs [63-66] and Rb or their combinations [67-74] (**Figure 2.2.4.2).**

2.2.5. Optical properties

Optical absorption

One of the outstanding features of perovskite semiconductors is their large absorption coefficient (one of the key parameters for increasing power conversion efficiency in solar cells, and also achieving low threshold lasing), which is much higher than other solution-processed semiconductors, and for example because of that several hundred nanometres of perovskite thin layer applied into solar cells can be as efficient as thick layers of traditional semiconductors which are on micrometre and even hundreds of micrometre scale [75, 76]. For instance, it is reported that the optical absorption coefficient of $MAPbI_3$

is up to 1 order of magnitude higher than that of GaAs within the visible light range [77-79].

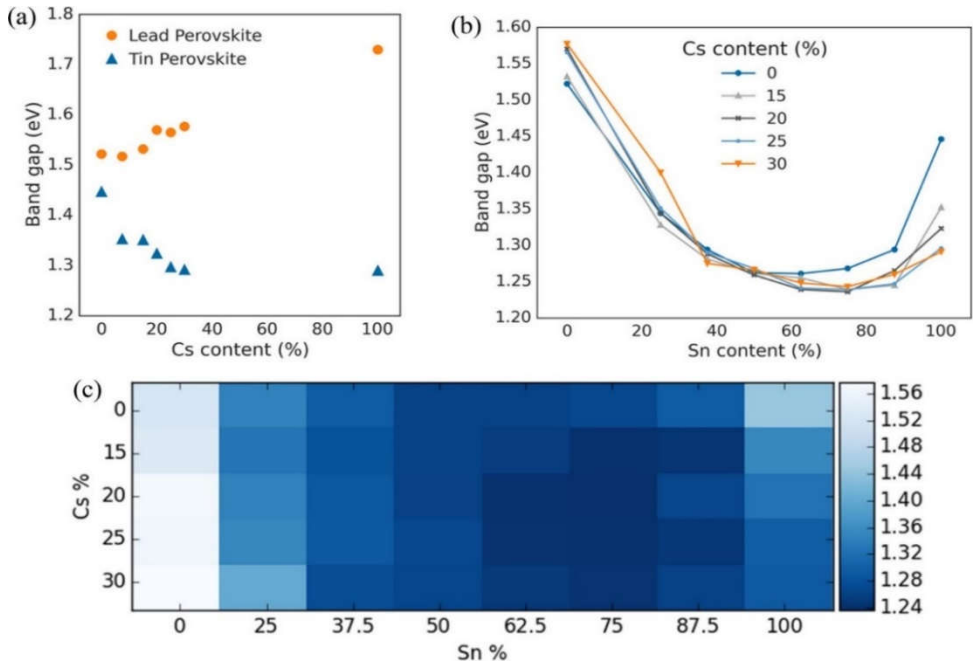

Figure 2.2.4.2. *a) Optical band gap of lead- and tin-based perovskites $FA_{1-x}Cs_xMI_3$ (M = Sn, Pb) as a function of caesium content. b) Band gap of five series of tin-lead mixed perovskites, corresponding to caesium fractions of 0,15, 20, 25, and 30%. c) 2-dimensional map of band gap (in eV) across the formamidinium-caesium and tin-lead compositional space studied [69].*

Furthermore, perovskites have been considered to be a class of semiconductors with a remarkably sharp absorption edge showing that they contain almost no defects, and therefore regarding SQ theory, these materials can be applied in light emitting devices, and solar cells with an outstanding performance. For example, as can be seen in **Figure 2.2.5.1**, organometal halide perovskite shows much sharper absorption edges than Si, and comparable to some other well-known semiconductors such as GaAs, and CdTe [80].

Photoluminescence spectrum (PL)

Another noticeable attribute of perovskite semiconductors is that their PL spectrum can be precisely tuned from the UV to the infrared region by just changing their composition

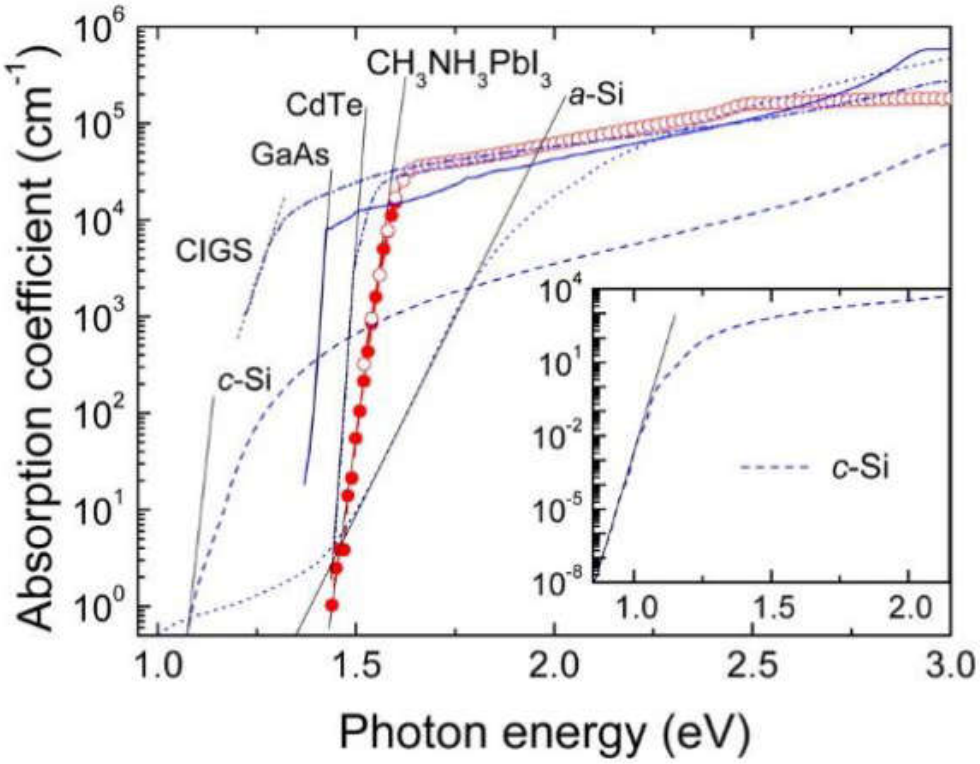

Figure 2.2.5.1: *Optical absorption coefficient of the perovskite material $MAPbI_3$ in comparison with other material, including amorphous silicon (a-Si), GaAs, CIGS, CdTe, and crystalline silicon(c-Si), all measured at room temperature [80].*

(explained in **Section 2.2.4**). This wavelength tunability by just changing the precursor composition in a low cost and low temperature solution process is considered to be unique for this class of materials when compared to other semiconductors such as silicon, for which expensive, and high temperature techniques are needed, while having less flexibility in bandgap tuning.

Photoluminescence quantum yield (PLQY)

Because of their high absorption coefficient, and limited non-radiative losses, perovskites exhibit high internal quantum efficiency (IQE) which is an important key for achieving high performance light emitting devices. However, due to possessing a high refractive

index, the outcoupling probability (P_{out}) may be very low in this class of materials [81], especially for smooth layers which give rise to waveguiding with low scattering, the external and internal efficiency may differ significantly, and a comparison of external PLQY (η_{ext}) may not be very informative. As detailed by Richter et al., photon-recycling has to be taken into consideration to determine the internal PLQY (η_{int}), and therefore this measurements needs to be performed in an integrating sphere. Taking P_{out} for the respective layer, a relation between η_{int} and η_{ext} can be derived as follows [82]:

$$\eta_{ext} = \eta_{int} \times P_{out}/(1 - \eta_{int} + \eta_{int} \times P_{out} + \eta_{int} \times P_{sub}) \qquad \textbf{2.2.5.1}$$

where P_{sub} is the portion absorbed by the substrate. Calculating η_{ext} will be explained in more details in **Section 6.4**.

2.2.6. Principle of the distributed feedback (DFB) laser

Stable single frequency diode lasers with narrow spectral linewidth are extremely favourable and essential for fabricating elements such as wavelength division multiplexing and coherent high bit rate optical communication systems which are indispensable for actualizing high speed information networks.

In order to realize a diode laser with a single wavelength operation, integrating a frequency selective component is required, that can be fulfilled by applying a Bragg reflecting grating which should be designed in a way that only the desired wavelength is reflected back into the laser cavity to get amplified.

Moreover, for improving heat dissipation, the volume of the laser's active region needs to be increased. However, the increase of cavity's volume can lead to multimode operation which is not desirable [83]. It is investigated that integrating Bragg reflecting grating makes it possible to achieve single mode oscillation even in larger cavities. This Bragg reflecting grating is placed either externally on either sides of the cavity which is called distributed Bragg reflector laser (DBR), or incorporated continuously along the entire length of cavity, named distributed feedback laser (DFB).

DFB lasers are more demanded as they can provide both longitudinal and transversal single mode emission at a precise wavelength with an extraordinary narrow line width. Furthermore, their emission wavelength can be tuned, their operation is mode-hope free which influences lasing stability, and they are also considered to be more thermally stable.

A typical structure of a DFB diode laser is shown in **Figure 2.2.6.1**, in which a Bragg grating, which functions as a mirror that selectively reflects only one wavelength, is fabricated on top of an active region (here perovskite).

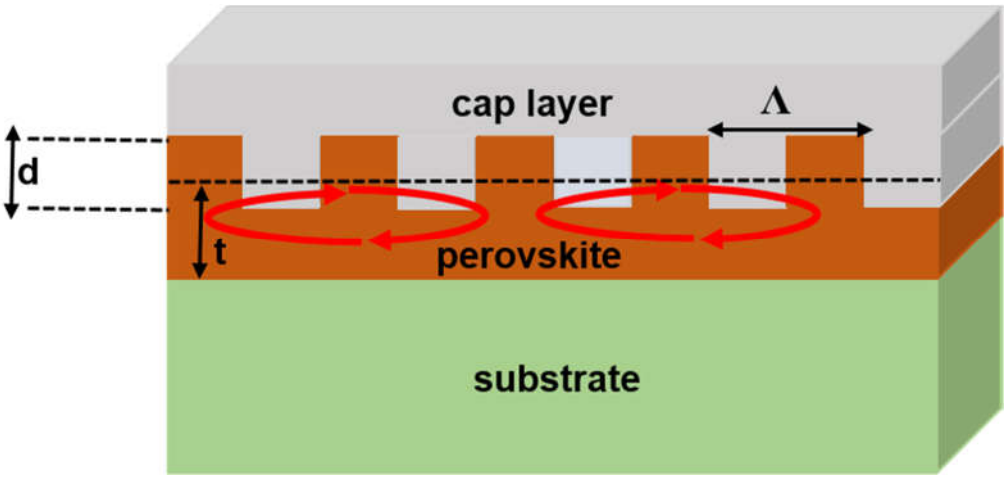

Figure 2.2.6.1. *Typical structure of a DFB diode laser.*

In fact, the coupling of waves propagating in forward and backward directions in the active medium occurs only for wavelengths satisfying [84]:

$$\Lambda = \frac{m\lambda}{2n_{eff}} \qquad \textbf{2.2.6.1}$$

Where λ is the free-space wavelength (perovskite wavelength), Λ is the grating's periodicity, n_{eff} is the effective refractive index of the optical laser mode, and m is the order of Bragg diffraction.

The refractive index (n_{med}^{eff}) of the effective medium (perovskite, cap layer) can be calculated, and tuned by knowing and varying the refractive index of the perovskite and that of the cap layer, the geometrical parameters of the effective medium, and the grating's periodicity. For example, regarding the grating in **Figure 2.2.6.1** with 50% duty cycle, and considering air as the cap layer which has a refractive index of one, I can extract the refractive index $\left(n_{med}^{eff}\right)$ of the effective medium through:

$$\left(n_{med}^{eff}\right) = \frac{(t * n_p + {}^{d}/_{2})}{t + {}^{d}/_{2}} = n_p - (n_p - 1) * \frac{{}^{d}/_{2}}{t + {}^{d}/_{2}} \qquad \textbf{2.2.6.2}$$

Where t, d, and n_p are the initial thickness of perovskite layer, the depth of the stamp, and the refractive index of the perovskite at the wavelength of λ, respectively.

By knowing the refractive indexes of the effective medium, the cap layer, and the substrate, the effective refractive index of the optical laser mode (n_{eff}) can be calculated through full optical simulation of the mode structure of the photonic crystal, using a transfer matrix alogorithm.

For obtaining light-amplification in the visible spectral range through first-order Bragg diffraction, it is essential to use a grating with a periodicity less than 200 nm which is difficult to be achieved with low-cost technologies. Therefore, a second- or even higher order Bragg diffraction grating is an option, while the first-order Bragg diffraction is considered to be easier applicable for longer lasing wavelengths.

In this work, concerning the effective refractive index of the perovskite compounds, the outcoupled wavelength, and a simple grating fabrication, all DFB lasers are fabricated by applying second-order Bragg diffraction (m=2), and the emitted light, resulting from first order diffraction, is coupled out in the direction normal to the surface. The geometrical parameters of the waveguide are designed in a way to support the fundamental transverse electric (TE0) mode.

Chapter 3

Fluorescence Intermittency in Perovskite Nanocrystals

3.1. Introduction

Over the past decade, organometal halide perovskites have emerged as a highly promising semiconductor to be applied as an active layer into optoelectronic devices, such as solar cells, light emitting diodes, photodetectors, and lasers. Typically, active layers in these applications consist of perovskite nanocrystals (NCs) sized on the order of 100 nm, with a critical importance of defects and trap states for charges [85, 86]. Therefore, having knowledge of these defects and trap states would be of particular interest as they may critically affect device performance. These trap states and defects have been linked to fluorescence intermittency that has been found in $MAPbI_3$ nanowires [87] and nanoparticles of $CsPbI_3$ [88] and $CH_3NH_3PbBr_3$ [89]. Interestingly, Wen et al. observed blinking in dense layers of $CH_3NH_3PbBr_3$ NCs, while single NC did not show fluorescence intermittency [90]. The basic mechanism of this phenomenon is under debate, and there exists no consensus as to the microscopic origin of blinking [91]. The colour tunable and narrow-band perovskite quantum dots have been identified to be promising

candidates for display applications [92]. This field of application would severely be affected by intermittent emission characteristics [93].

Fluorescence intermittency is a general phenomenon found in single molecules [94, 95] and semiconductor nanostructures, like quantum-dots (QDs) [96] and –wires (QWs) [97]. Under continuous illumination, these objects switch between an emissive "on" state and a non-emissive "off" state, which each are found to last up to minutes. II-VI semiconductor NCs (e.g. cadmium selenide (CdSe)) have been the "fruit-flies" for the study and the modelling of the underlying physics for more than 20 years. Their size typically varies between 1-8 nm. Based on the early work of Efros and Rosen, a photoinduced charging process of the NC was used to explain the blinking phenomenon [98]. Briefly, upon photo-excitation, an electron-hole pair (or exciton) is generated in the NC. Aside from regular radiative recombination, either the hole or the electron may become trapped in a surface state leaving a single charge inside the NC. Alternatively, auto-ionization in a NC which is occupied by more than one electron-hole pair may lead to the same charged state (Auger ionization) [99]. A further photo-excited electron-hole pair in this charged NC may now undergo non-radiative decay via Auger recombination – its energy is transferred to the single charge carrier in the NC. As Auger recombination in NCs has been shown to be significantly faster than the radiative decay, the NC will be essentially non-emissive ("off"). If the trapped surface-charge becomes de-trapped after some time, the NC is neutralized and becomes emissive again ("on"). The auger picture has been challenged in a range of reports and a further possible mechanism for fluorescence intermittency has been set up [100]. In an alternative scenario, either the electron or the hole of the photogenerated electron-hole pair is trapped in a defect state before radiative recombination can occur. Immediately afterwards, the trapped charge recombines non-radiatively with its counter charge [101]. In this picture, the existence or the accessibility of the respective trap state fluctuates in time. This means that if the trap is absent or not accessible for the carrier, the NC would be in the "on" state, otherwise it would remain non-emissive "off". In either case, the analysis of fluorescence intermittency and its temporal statistics can be used as a reporter to analyse the nature of the trap states involved in the respective material system [101].

In this chapter, intermittent fluorescence in single NCs of $CH_3NH_3PbI_{3-x}Cl_x$ is analysed. Their on/off statistics and the dependence of the blinking characteristics on NCs size and illumination intensity are demonstrated.

3.2. Perovskite nanocrystals (NCs) preparation

After cleaning, the substrates are transferred to a nitrogen-filled glovebox. For the preparation of the $CH_3NH_3PbI_{3-x}Cl_x$ perovskites, an alternative two-step deposition technique is employed (**Figure 3.2.1**). more detail about substrate cleaning process and perovskite NCs formation can be found in **Appendix A/Experimental data**.

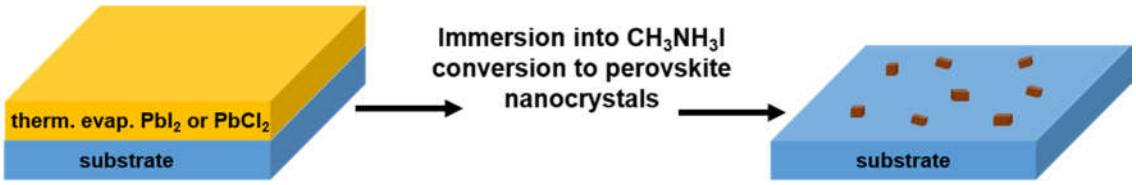

Figure 3.2.1. *Perovskite NCs synthesis in a two-step deposition process.*

I start with 30 nm evaporated lead chloride, and immerse it into a CH_3NH_3I solution. As can be seen from XRD patterns in **Figure 3.2.2**, $PbCl_2$ is just partially converted to $MAPbCl_3$ perovskite when it is dipped into the solution for 10 min, and there is no peak related to $MAPbI_3$ perovskite. Then, another $PbCl_2$ layer is dipped into the solution for 20 min, and as it is shown in **Figure 3.2.2**, the dominant signals in XRD appear at 14.08° and 28.36°, corresponding to the (110) and (220) planes of the tetragonal perovskite structure of $MAPbI_3$ [102], and there is no indication of $PbCl_2$ confirming the complete conversion of lead chloride into $MAPbI_3$ perovskite. Note, in a layer which is immersed into solution for 10 min, two peaks labeled with (◊) are identified, that cannot be associated with $PbCl_2$, MAI, $MAPbCl_3$, or $MAPbI_3$.

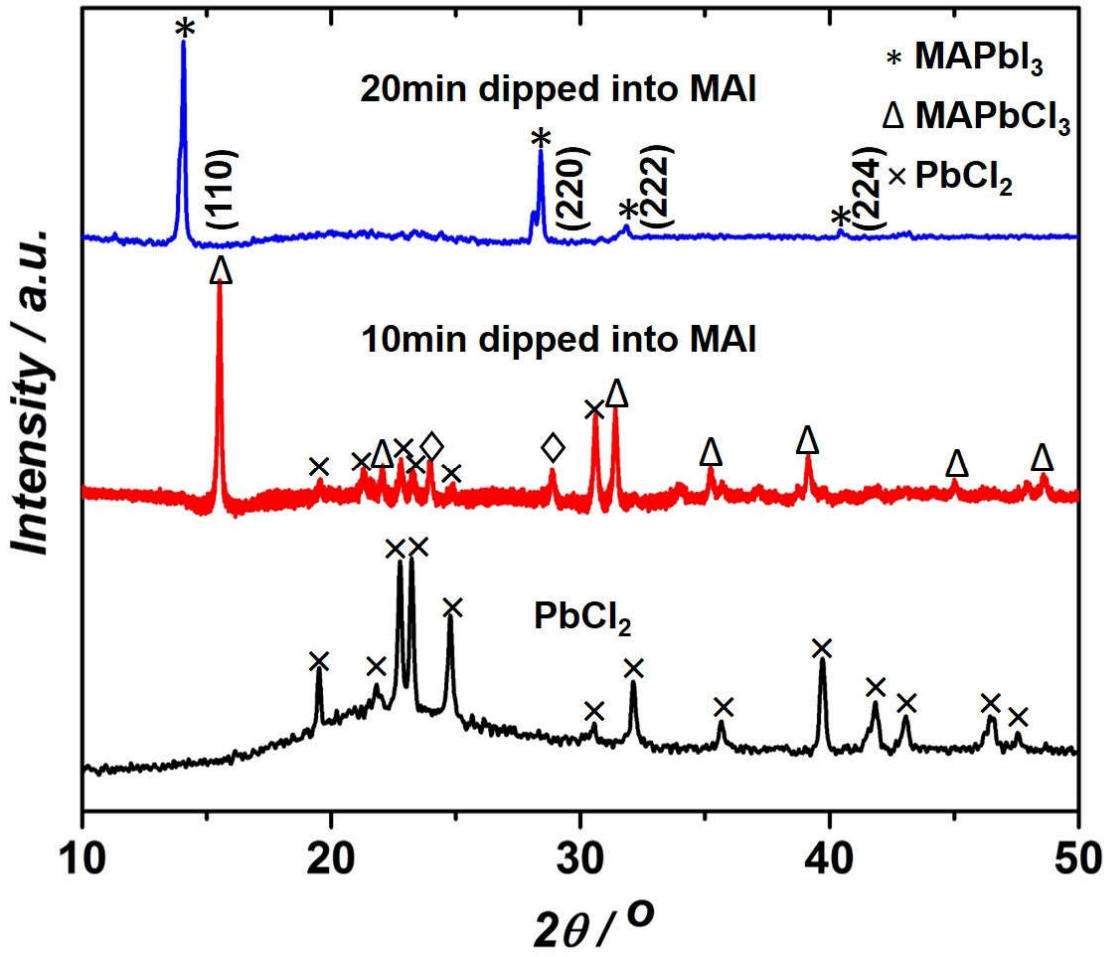

Figure 3.2.2. *X-ray diffractions of 30 nm evaporated $PbCl_2$, and resulting perovskite after dipping $PbCl_2$ into alcoholic CH_3NH_3I solution for 10 min, and 20 min.*

As expected and as evidenced in **Figure 3.2.3,** the material formed by using PbI_2 as starting layer shows the crystal structure of $MAPbI_3$ as well.

Respecting SEM images (**Figure 3.2.4**), the 30nm evaporated $PbCl_2$ layer after being immersed into MAI solution for 20 min and being converted to $MAPbI_3$ perovskite consists of dense perovskite NCs covered with quite a lot of rods, plates and cuboids which makes it difficult to study the isolated single perovskite NCs.

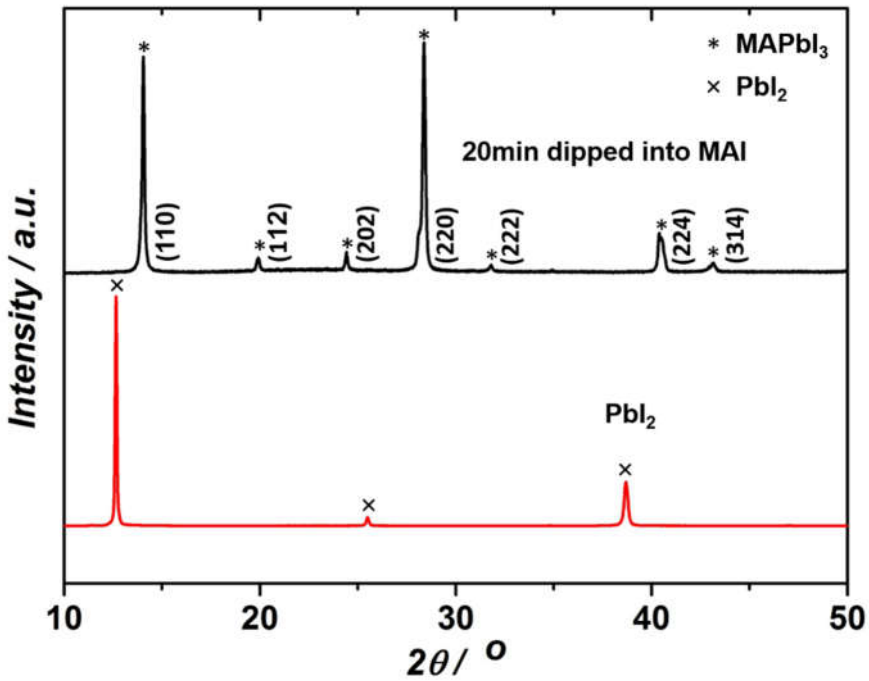

Figure 3.2.3. *X-ray diffractions of 30 nm evaporated PbI_2, and resulting perovskite after dipping PbI_2 into alcoholic CH_3NH_3I solution for 20 min.*

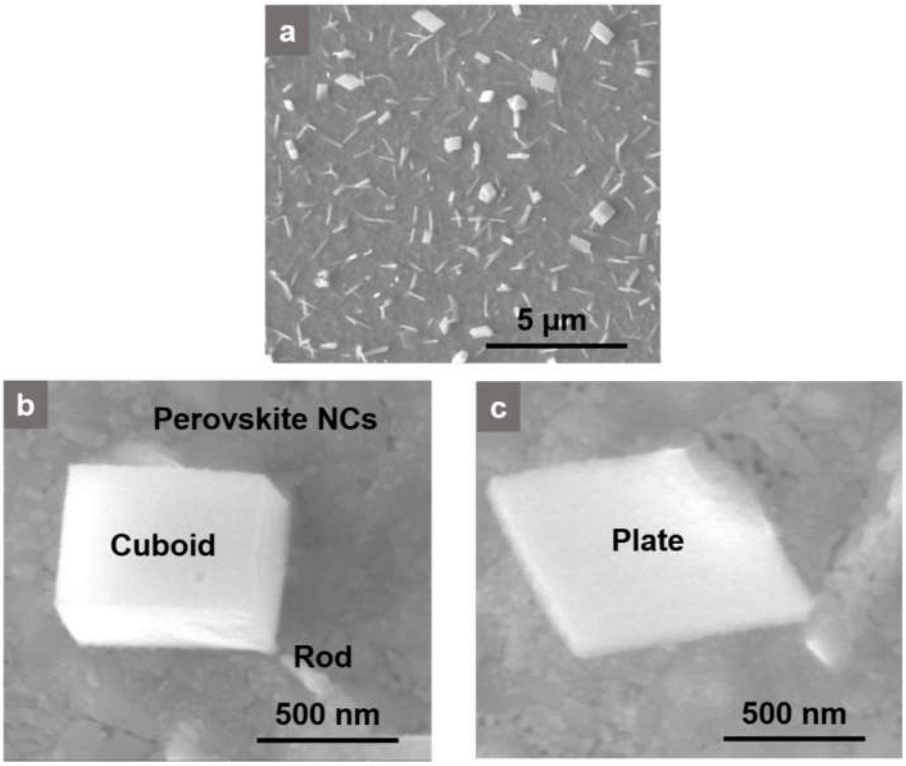

Figure 3.2.4. *a) SEM of the resulting Perovskite (30 nm evaporated $PbCl_2$ dipped into alcoholic CH_3NH_3I for 20 min). b,c) magnified SEM of cuboid, plate, and rod forming on surface.*

Therefore, the thickness of the $PbCl_2$ has been decreased step by step until the perovskite NCs are properly isolated, so that they can be separately investigated. In **Figure 3.2.5**, the SEM images of 2Å evaporated $PbCl_2$, which is subsequently converted to $MAPbI_3$ NCs by dipping into CH_3NH_3I, is shown. By this thickness, I can easily demonstrate isolated perovskite NCs. The size of individual cuboid shaped NCs is typically about 85-150 nm edge length.

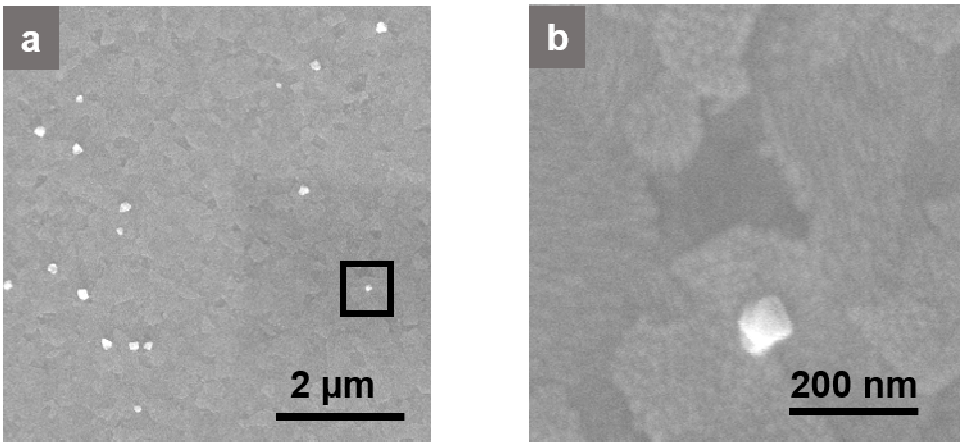

Figure 3.2.5. *a) SEM of the resulting perovskite NCs where only 2Å $PbCl_2$ is evaporated, and b) magnified view of a single representative perovskite NC. The NC in part (b) is marked with a black square in (a). The underlying nano-structure results from the ITO coated substrate.*

For comparison, the SEM images of samples with 5 Å, 1 nm, and 2 nm evaporated lead chloride films are also presented in **Figure 3.2.6**.

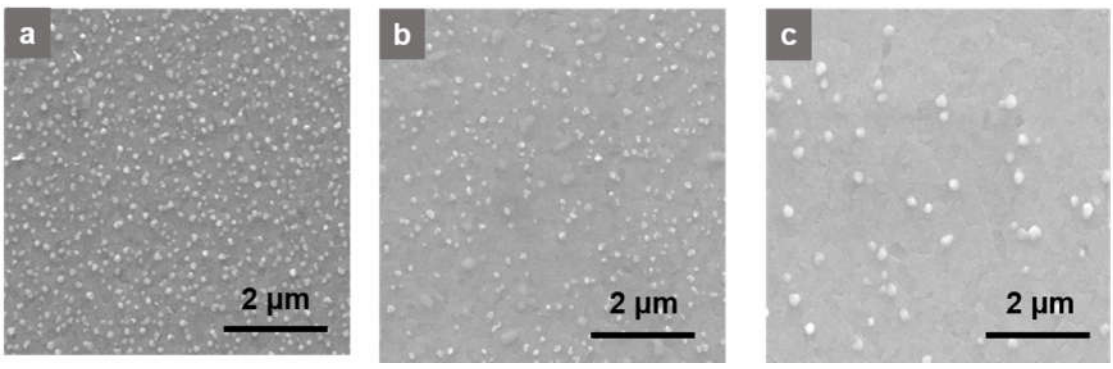

Figure 3.2.6. *SEM of the perovskite NCs resulting from immersing a) 2nm, b) 1nm, and c) 5Å lead chloride films into alcoholic CH_3NH_3I solution, respectively.*

By evaporating lead chloride films thicker than 2 Å, perovskites NCs get so close to each other, that it makes the optical investigation difficult. Therefore, the further investigation of perovskite films is carried out starting with just 2Å evaporated lead halide layer.

3.3. Optical analysis

To further prove the conversion of lead chloride into perovskite after immersion into CH_3NH_3I solution, the PL, which is averaged over an ensemble of resulting perovskite NCs, is investigated. As can be seen in **Figure 3.3.1**, the PL peak is located at 763 nm which is in agreement with previous reports on $CH_3NH_3PbI_{3-x}Cl_x$ [102], but it is a little blue shifted that can be attributed to the crystal size reduction according to D'Innocenzo et al [103].

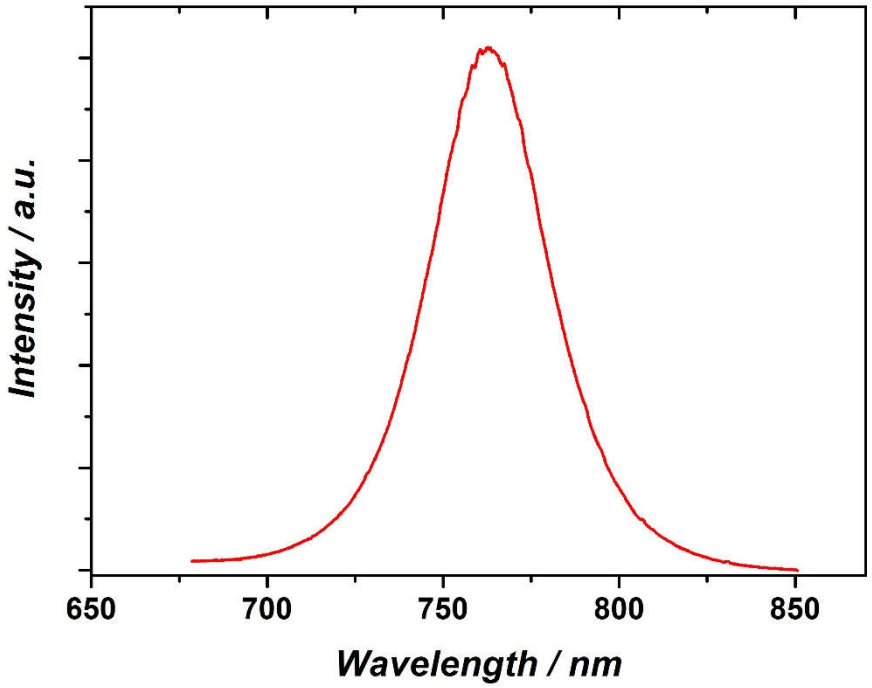

Figure 3.3.1. *Photoluminescence over an ensemble of $CH_3NH_3PbI_{3-x}Cl_x$ perovskite NCs (2Å evaporated lead chloride immersed into alcoholic CH_3NH_3I solution)*

To demonstrate fluorescence intermittency, the sample is placed under a conventional microscope and illuminated by a 532nm continuous wave laser from the back side

(**Figure 3.3.2.a**). The PL images and videos are obtained by blocking the transmitted laser light with a 610 nm long-pass optical filter. Videos are recorded with a camera, which is mounted on top of the optical microscope. An image analysis software (ImageJ) is used for further assessment.

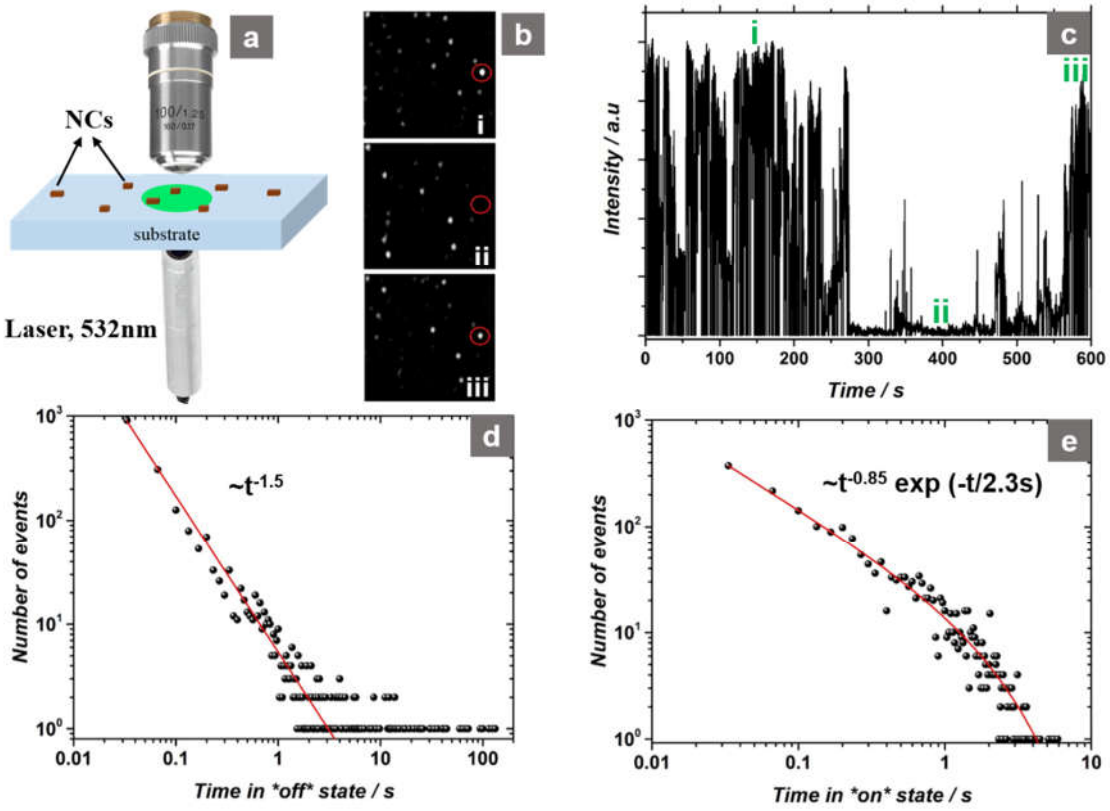

Figure 3.3.2. *a) Schematic of the emission microscopy using a conventional optical microscope with bottom illumination by a laser emitting at 532nm. b) Luminescence emission microscopy of an ensemble of NCs upon continuous wave excitation at different times (i at about 150 s, ii at 400 s and iii at 600 s). One NC is marked with a red circle, the luminescence intensity vs. time of this NC is displayed in (c). The temporal statistics for "off"-times and "on"-times for this representative NC are shown in (d) and (e), respectively. The observation time to record these data was 3600 s. The red lines show a fit to the data according to a (truncated) power law, yielding exponents of -1.5 (off-time), and -0.85 (on-time), respectively.*

Blinking of an individual NC (marked with a red circle) over the course of the experiment is explicitly visualized in **Figure 3.3.2b**. It has to be noted that many of the NCs **in Figure 3.3.3b** show luminescence intermittency. Introducing a threshold on the intensity vs. time trace in **Figure 3.3.2c**, I distinguish between an emitting "on" and a dark "off" state. Statistical analysis of the probability for the NC being in the "off" or in the "on" state for a certain time t_{off} or t_{on} is shown in log-log plots (**Figure 3.3.2d, e**).

Note, the minimum time scale of 33 ms is given by the minimum exposure time of my camera used for the fluorescence microscopy. The "off" characteristics (**Figure 3.3.2d**) apparently follow a power law $\sim t^{\alpha}$ with $\alpha \approx -1.5$ over three decades, only limited by the duration of observation (3600 s). In some events, t_{off} may become even larger than 100 s. Note, the strictly non-exponential, power-law behaviour is either indicative of a statistical ensemble of charge trap states involved or of a charge trap state whose existence or accessibility for charge carriers fluctuates over time [104].

For comparison, the "on" characteristics (**Figure 3.3.2e**) follows a truncated power law $\sim t^{\beta} \exp(-t/\tau)$ with $\beta \approx -0.85$ and $\tau = 2.3$ s as a result form a least square fit to the data. A truncated power law dependence has been introduced by Tang et al. to model diffusion controlled blinking phenomena in inorganic NCs, where τ is the characteristic truncation time [105]. A similar truncation in the t_{on} characteristics has been encountered in blinking CdSe NC, and has been attributed to a second, competing photo-induced process [106].

By analysing several of the NCs in a similar manner, It has been found that α typically varies between -1.4 and -1.5, while β ranges between -0.85 and -1.2. It should be noted that similar results of fluorescence intermittency are found, regardless of whether $PbCl_2$ or PbI_2 is used as precursor for the synthesis of the perovskite NCs.

An important note on my finding of intermittent fluorescence in perovskite NC is that they do blink in spite of their large dimensions of about 100 nm (**Figure 3.2.5b**) while in materials such as CdSe, blinking has been successfully suppressed by the concept of so called "giant" NCs based on 3-4 nm sized CdSe core and a thick ZnS or CdS shell to form particles with a diameter of up to 20 nm. It has been argued that this concept leads to an efficient separation of the core wave-functions from the surface states.

The absence of blinking in larger sized NCs of other material systems, may be related to the size of the Bohr radius a, which depends on the material properties, i.e. reduced effective mass m_r^* ($1/m_r^* = 1/m_e^* + 1/m_h^*$) and the relative dielectric constant ε_r as $a = \varepsilon_r\, m_0/m_r^*\, a_0$. With $a_0 = 0.529$ Å and m_0 is the mass of a free electron. For example, in CdSe the Bohr radius is 5.6 nm [107].

For $MAPbI_3$, effective masses for electrons and holes of 0.23 m_0 and 0.29 m_0 have been determined, respectively [108]. A high-frequency dielectric constant of 7.1 has been reported for $MAPbI_3$. This would result in a Bohr radius of 2.9 nm. On the other hand, some reports have indicated a static dielectric constant in the range of 70-1000 [109, 110]. Furthermore, it has been argued that due to the large exciton radius in organo lead halide perovskites, for the Wannier–Mott description of electron-hole interaction the static dielectric constant has to be taken into account [111, 112]. Along these lines, the Bohr radius in $MAPbI_3$ could be estimated to be on the order of 10-100 nm, subject to the large variations in reported numbers for the dielectric constant. Of course, these large Bohr radii would come along with an ultra-low binding energy, which actually would lead to the transition from excitons to free carriers, as discussed in several reports [113, 114].

3.4. Influence of perovskite NC size on fluorescence intermittency

In an attempt to explore the limits of particle size, up to which intermittent fluorescence is found, larger $CH_3NH_3PbI_{3-x}Cl_x$ NCs are grown by increasing the thickness of the evaporated lead halide layer. For this special experiment, and regarding SEM measurements (**Figure 3.2.4**), 30 nm $PbCl_2$ film is evaporated, and subsequently convert it to perovskite as explained earlier. This perovskite film consists of perovskite NCs with different sizes. Notably, while the smaller NCs on these samples show fluorescence intermittency as discussed before, for NC with a size > 200 nm continuous (non-intermittent) emission is found. A representative of these non-blinking larger NCs is shown in **Figure 3.4.1**.

The above considerations and experimental results would be in line with a model, which interprets fluorescence blinking in my $CH_3NH_3PbI_{3-x}Cl_x$ NCs on the basis of the well-

established concept of non-radiative recombination due to Auger recombination (see my discussion in **Introduction**).

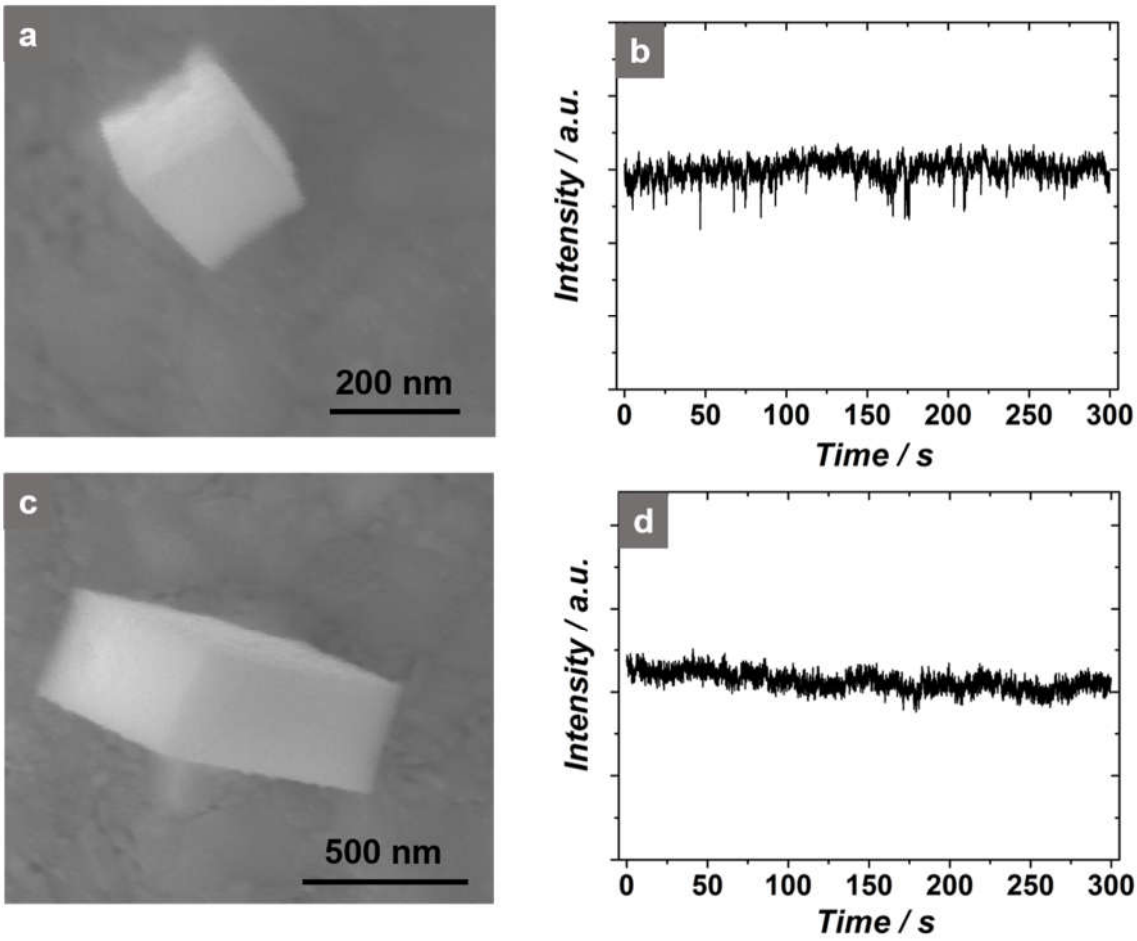

***Figure 3.4.1**. a, c) SEM image of $CH_3NH_3PbI_{3-x}Cl_x$ NCs showing continuous (non-intermittent) fluorescence. The fluorescence intensity vs. time is shown in (b, d).*

A similar interpretation of intermittent fluorescence has been provided for NCs of $CsPbI_3$ [88], which were significantly smaller (size ~ 10 nm) than mein and showed clear quantum confinement effects. In the same study, the authors have shown that the t_{on} statistics was significantly affected by the excitation intensity. With increasing excitation intensity, the probability of longer "on" times was significantly reduced. This is in agreement with the model of a non-emissive state that results from a trapped photo-induced charge.

3.5. Influence of illumination intensity and environment on fluorescence intermittency

It has been reported by several groups that perovskite photoluminescence depends strongly on optical pump properties and the surrounding atmosphere [115, 116]. For example, the PL increase of up to three orders of magnitude upon light illumination with an excitation power density of 0.01–1 W/cm^2 has been reported by Tian et al [115]. They also showed that the trapping sites which are considered to be responsible for non-radiative charge recombination can be de-activated by a photochemical reaction involving oxygen.

In light of the above discussion, the influence of illumination intensity and atmosphere on the fluorescence intermittency was studied. Perovskite NCs are prepared on glass substrates by evaporating just 2 Å $PbCl_2$, and converting it to perovskite by dipping into MAI, and then illuminating the perovskite NCs with a laser while increasing the illumination power density by an order of magnitude, changing between 1.8 and 18 W/cm^2. For the first experiment, I just illuminate the sample under ambient air, the same experiment which has been done for the results in **Figure 3.3.2.** As can be seen in **Figure 3.5.1**, by increasing the power density from 1.8 to 18 W/cm^2 for two selected perovskite NCs, blinking stops, and the NCs show a constant PL.

It is essential to mention that based on the size of the NCs, and therefore their defect density, by increasing the illumination power density, for some of NCs, blinking stops, for some, which have been totally off and showed no PL, blinking is triggered, and for some of them, the on time gets longer. Based on this observation, the stop of blinking by increasing the illumination power density can be correlated to defect/trap filling which has also been proposed to explain the increase of PLQY at elevated excitation power density [117, 118]. In fact, these defects and traps are responsible for non-radiative decay and are considered as PL quenchers.

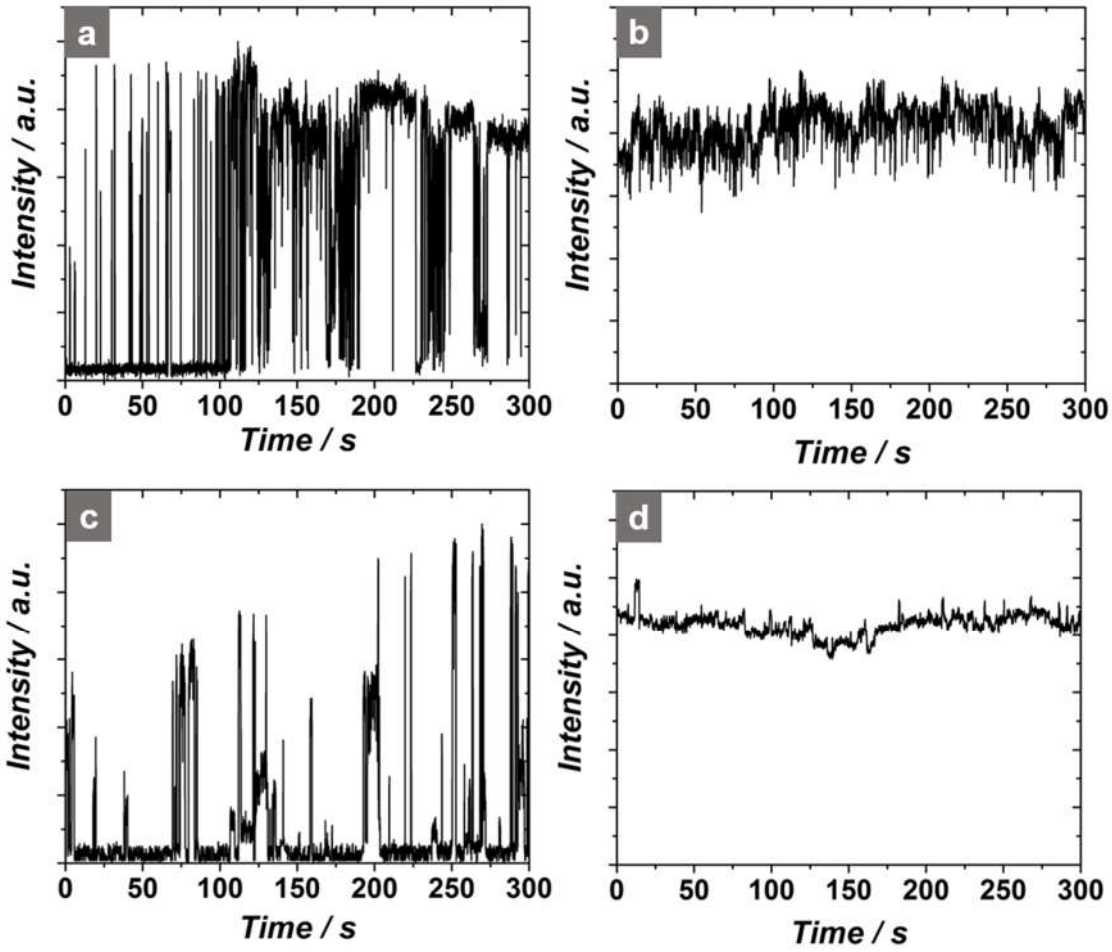

***Figure 3.5.1**. The fluorescence intensity vs. time when illuminated by a, c) power density of 1.8 W/cm², and b, d) 18 W/cm². (Note: (a, b) and (c, d) are measurement results from two different NCs illuminated with different power densities)*

Note, the fluorescence intermittency returns by just reducing the illumination power density to 1.8 W/cm^2, the NCs again start to blink, showing the reversibility of fluorescence intermittency. Therefore, it can be concluded that the increase of illumination intensity doesn't infer permanent passivation of the defects, but just temporarily fills the defects/traps.

To determine environmental effects on fluorescence intermittency, perovskite NCs are encapsulated by spin-coating 1 µm of polymethylmethacrylat (PMMA) and then depositing 100 nm aluminium oxide (Al_2O_3) by atomic layer deposition (ALD). the first aim is to understand if the blinking is caused by defects which have been formed during

preparation of the perovskite inside the nitrogen-filled glovebox or if they originate from the exposure to air during PL microscopy.

In **Figure 3.5.2**, the fluorescence behaviour of encapsulated perovskite NCs upon illumination with a power density of 1.8 W/cm^2 is shown. As can be seen clearly (**Figure 3.5.2a**), even after encapsulation, the perovskite NCs still switch off and on over illumination which dismisses this hypothesis that the fluorescence intermittency originated from exposing the sample to air and therefore forming defects through sample decomposition or degradation. Thereafter, the power density is increased to 18 W/cm^2 to further prove that stop of blinking is due to defects/traps filling and not because of photo induced reaction involving oxygen, and passivation of defects which have been already reported by some groups [115, 116]. As can be seen obviously in **Figure 3.5.2b**, by increasing the power density from 1.8 W/cm^2 to 18 W/cm^2, blinking stops showing that oxygen plays no role in elimination of blinking.

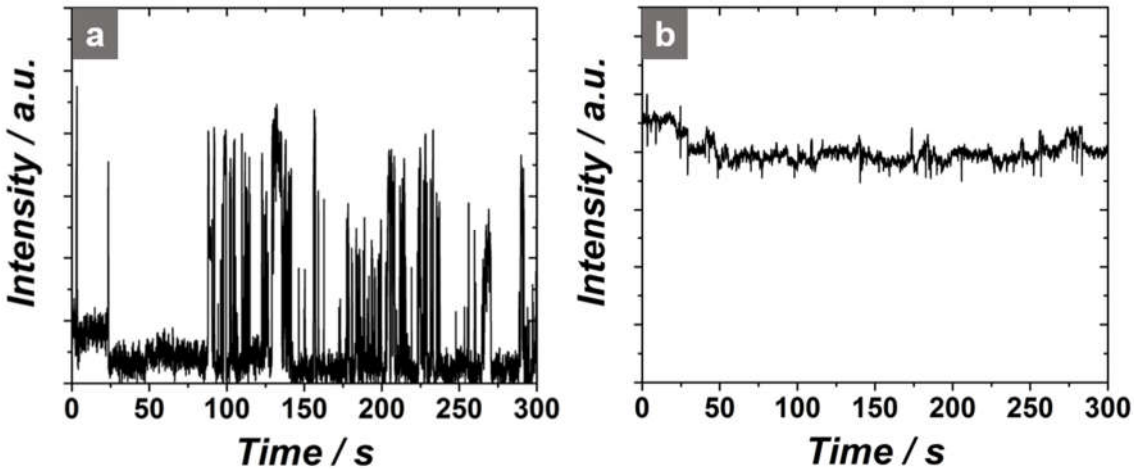

***Figure 3.5.2**. The fluorescence intensity vs. time of $CH_3NH_3PbI_{3-x}Cl_x$ NCs, encapsulated by 1 µm PMMA plus 100 nm Al_2O_3, when illuminated by laser having a) power density of 1.8 W/cm^2, and b) 18 W/cm^2.*

3.6. Summary

In this chapter, fluorescence intermittency of $CH_3NH_3PbI_{3-x}Cl_x$ perovskite NCs, prepared through a two-step deposition process, is demonstrated. Perovskite NCs fluorescence is analysed through a conventional microscope while illuminating the sample by a 532nm

continuous wave laser. Notably, I could observe intermittent fluorescence from perovskite NCs even with exceptionally large sizes of about 100 nm showing the presence of a high density of trap states on the surface of the perovskite NCs. It is shown that off and on times of fluorescence blinking follow a power law t^{α}, and a truncated power law t^{β} exp $(-t/\tau)$, respectively. The influence of NC size, illumination intensity, and environment on fluorescence intermittency is demonstrated. Interestingly, it is observed that when NCs get bigger than 200 nm, blinking stops which indicates the importance of perovskite grain sizes on perovskite-based devices performance. By increasing the illumination intensity, I am also able to stop blinking which is the indication of filling defect/trap sates presence on the surface of the perovskite NCs. By encapsulating perovskite NCs, it is demonstrated that elimination of blinking through increasing the illumination intensity is not affected by environment which dismisses the possibility of photo induced reaction with oxygen.

Chapter 4

Photonic Nanostructure Patterning into $MAPbI_3$ by Direct NIL

4.1. Introduction

With astonishing optoelectronic properties comparable to the most prosperous inorganic semiconductors like GaAs, organometal halide perovskites such as $CH_3NH_3PbI_3$ ($MAPbI_3$), apart from considerable progress in the field of solar cells, state an intriguing platform for light emitting diodes and lasers.

As observing amplified spontaneous emission (ASE) is a prerequisite for lasing, ASE in $MAPbI_3$ and other organometal halide perovskites has been substantially investigated and characterised [7, 8, 9, 10,76, 119].

For lasing, DFB resonators are considered as a promising resonator for obtaining low-threshold electrically operated laser diodes. One way to realize a DFB resonator would be the direct pattering of the perovskite with the highest control and precision. However, due to the relatively low intrinsic stability of hybrid perovskites and their susceptibility to a number of commonly used solvents, patterning via established wet-chemical lithography techniques is extremely limited. For example, well established

photolithographic techniques cannot be applied as the material readily decomposes in the presence of moisture [120]. On top of that, thermally activated decomposition of $MAPbI_3$ to CH_3NH_3I and PbI_2 has been evidenced even under inert conditions at temperatures of 85 °C [59, 121].

To overcome the above mentioned issues resulting from direct patterning, pre-patterned substrates with a resonator structures have been used, on top of which a rough, polycrystalline perovskite active medium has been formed [9]. In general, the scattering losses due to the rough perovskite layers infer elevated lasing thresholds and, in some cases, require cryogenic temperatures to achieve lasing. Therefore, for fabricating stable, and low threshold perovskite based DFB lasers, it is necessary to identify a patterning method that tackles the scattering issue, and at the same time prevents perovskite decomposition.

In this chapter, it is demonstrated for the first time, that photonic nanostructures can be prepared by nanoimprint lithography (NIL) directly into $MAPbI_3$ at temperatures as low as 100 °C (a temperature which is also used for fabricating perovskite solar cells) without any indication of decomposition resulting in significantly smoothened layers. Aside from smoothening, it is shown that the imprint process reduces the detrimental impact of surface defects, that form recombination sites in as–deposited layers, considerably.

As a case study, imprinted 2D photonic crystals (2DPC) are prepared and demonstrated to afford lasing with a very low threshold of 3.8 $\mu J/cm^2$ at room temperature, which is indicative of excellent material quality after imprint. The direct NIL patterning of photonic structures into perovskite layers is expected to inspire not only the field of lasers but also other perovskite-based devices, such as LEDs and solar cells.

Note, this chapter is based on my previously published journal article **"Photonic Nanostructures Patterned by Thermal Nanoimprint Directly into Organo-Metal Halide Perovskites", Adv. Mater., 2017, 29, 1605003.**

4.2. Thermal nanoimprint lithography (NIL) process

The stamp used for imprinting $MAPbI_3$ layers, as depicted in **Figure 4.2.1**, features a triangular array of pillars of 230 nm in diameter, 140 nm in height, with a pitch of 450 nm across the whole surface (the stamp is designed following the considerations in **Section 2.2.6**).

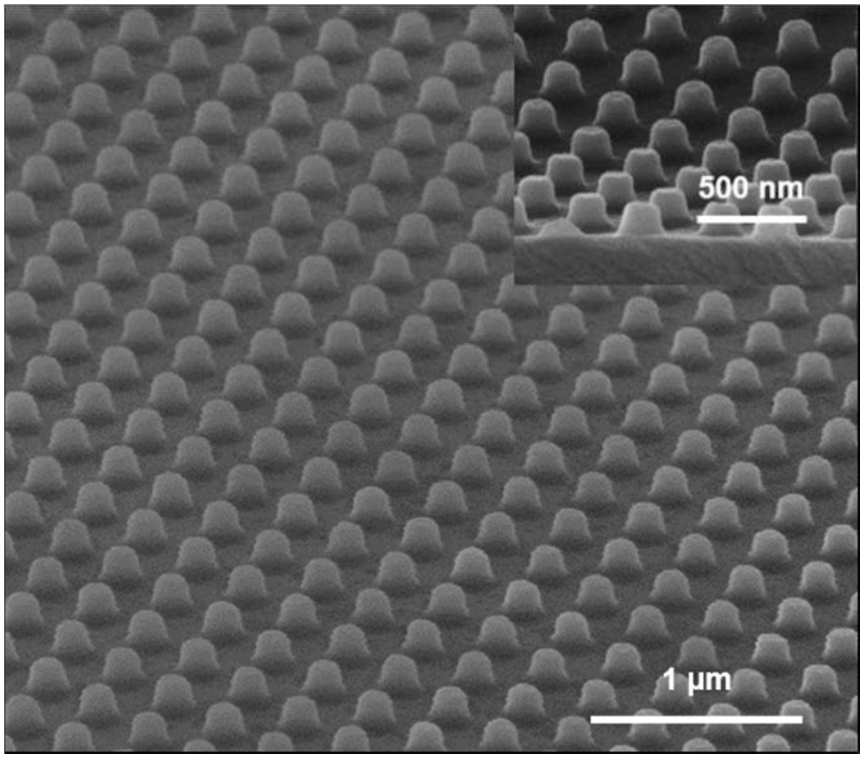

Figure 4.2.1. *SEM image of the stamp used for imprinting $MAPbI_3$ perovskite.*

The thermal imprint process follows the protocol shown in **Figure 4.2.2**. The imprint temperature is 100 °C, a temperature similar to that used in the solution processing of $MAPbI_3$-based solar cells [122]. The details of preparing the stamp and of the NIL process are given in **Appendix A/Experimental data**.

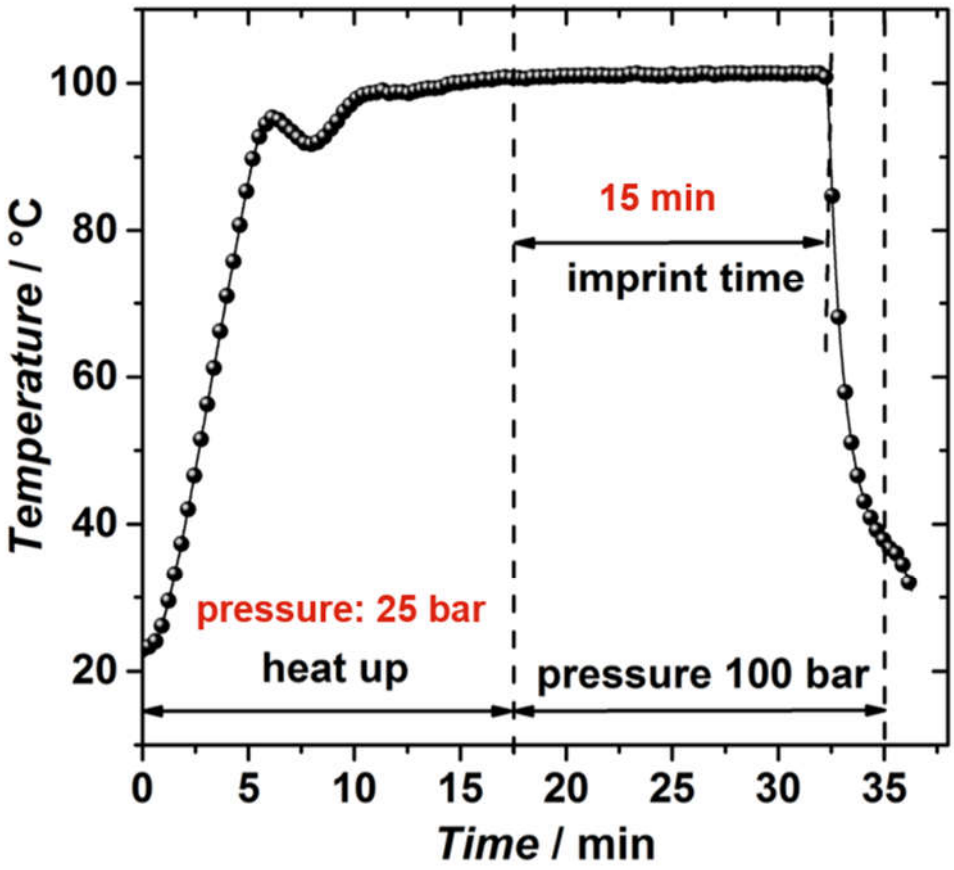

Figure 4.2.2. *Applied temperature and pressure over thermal nanoimprint procedure for imprinting $MAPbI_3$ perovskite layers.*

4.3. $MAPbI_3$ thin film deposition

The $MAPbI_3$ layers used in this study are prepared by spin coating from a lead acetate ($Pb(Ac)_2$) and anhydrous methylammonium iodide (CH_3NH_3I) solution in anhydrous dimethylformamide (DMF) following a deposition protocol that can be found in **Appendix A/Experimental data.** The thickness of the perovskite film is measured by looking at cross sections in SEM (**Figure 4.3.1a**); the typical thickness is between 150 to 200 nm as thickness changes moving from the centre of the sample to the edges, the typical behaviour of a spin-coating process. As shown in **Figure 4.3.1b**, the resulting layers exhibit a polycrystalline morphology.

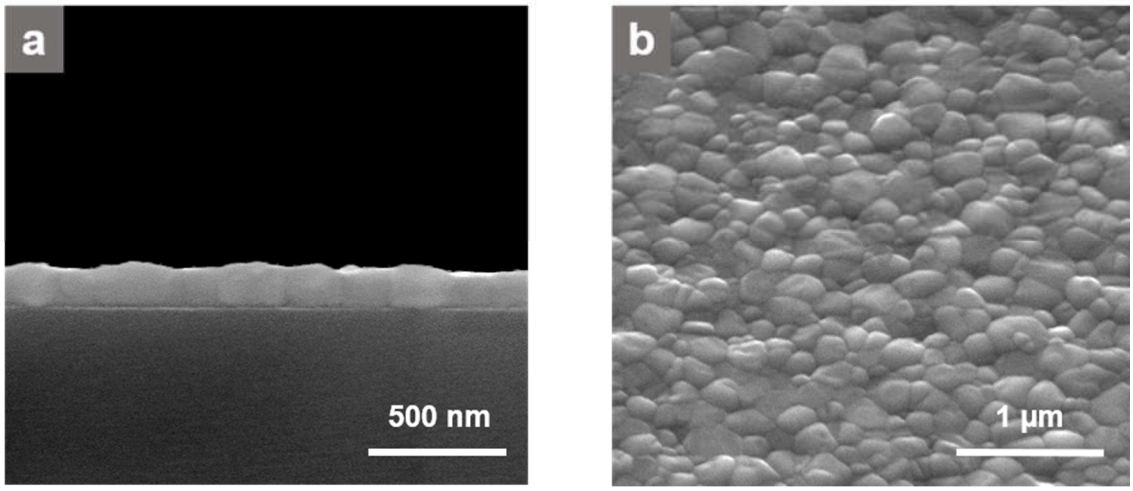

Figure 4.3.1. *SEM image of a) the cross section, and b) the top view of as-deposited $MAPbI_3$ perovskite layer.*

Note, the precursor solution concentration and the spin-coating/post-annealing parameters, in order to form the desired thickness, are subject to the design considerations of the $MAPbI_3$-based optical waveguide which was explained partially in **Section 2.2.6**, and will be characterised in more detail in **Section 4.7**.

4.4. The effect of NIL on perovskite morphology and crystallinity

To determine the quality of imprinting and transferring of patterns into the $MAPbI_3$ perovskite film, SEM is performed. The SEM images of imprinted perovskite layer are shown in **Figure 4.4.1**.

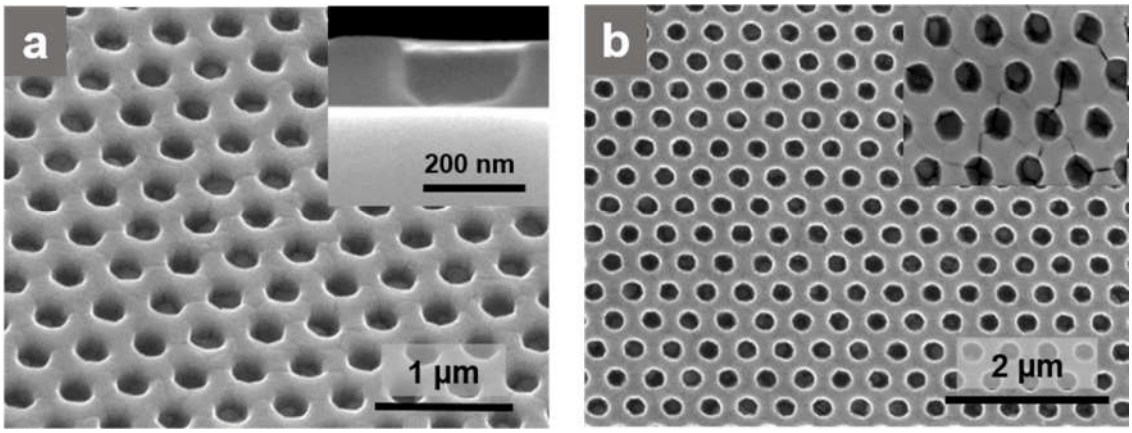

Figure 4.4.1. *a) SEM image of the imprinted perovskite layer viewed under an angle of 45° (inset: cross section). b) Plan view SEM of the imprinted layer (inset: magnified view).*

As can be seen clearly, the pattern of the stamp is perfectly replicated into the perovskite layer even on a large area which is because $MAPbI_3$ perovskite is regarded as a soft material. Crystal binding in these materials has been found to extend beyond purely covalent/ionic bonds, but rather also includes significant contributions of van der Waals interactions among the halide atoms as well as Hydrogen bonding [123]. Closer inspection shows some residual grain boundaries in the imprinted perovskite layer (inset in **Figure 4.4.1b**).

To investigate how thermal NIL influences the surface morphology of the perovskite layer, I look at perovskite samples before and after imprinting through AFM (**Figure 4.4.2**).

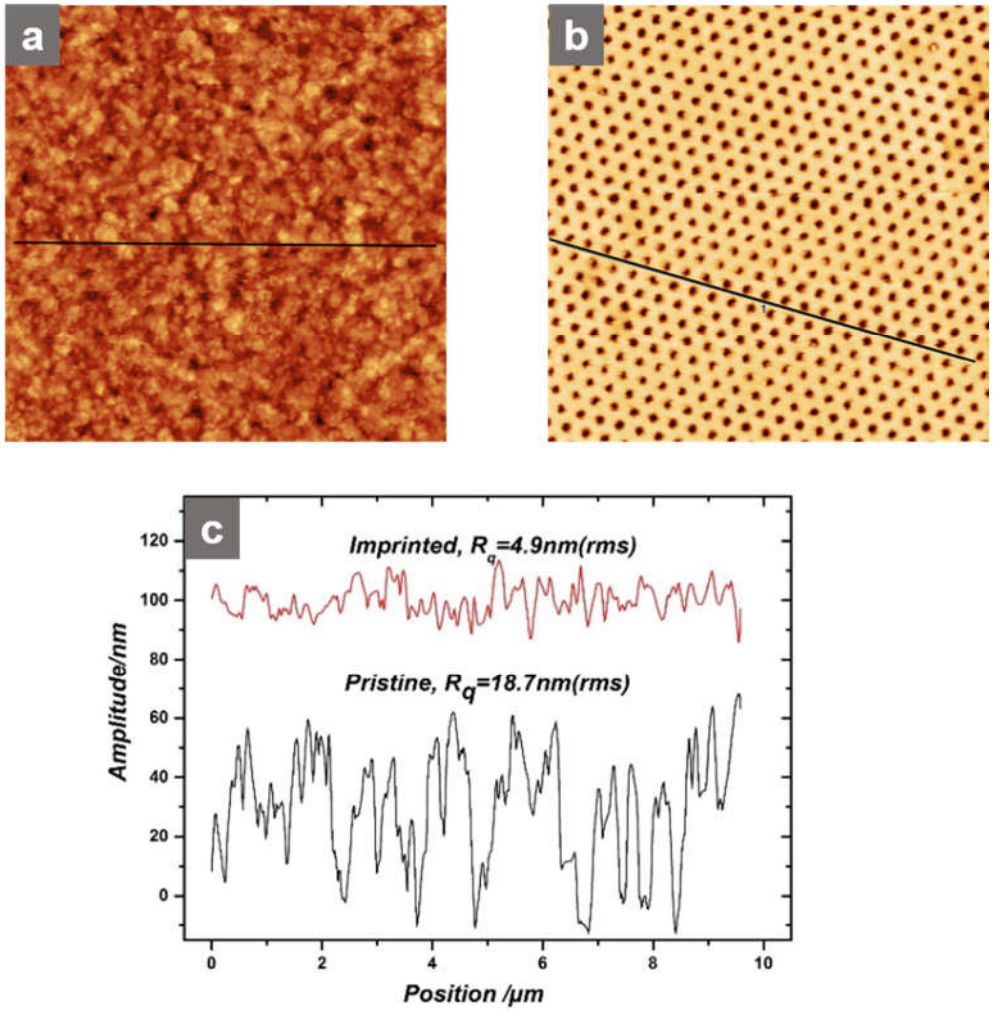

Figure 4.4.2. *a, b) AFM images of the $MAPbI_3$ perovskite layers before and after imprint, respectively. The lines in the viewgraphs indicate the location of the traces shown in (c). The traces shown in (c) have been vertically offset for clarity.*

While as-prepared $MAPbI_3$ layers are rough, which is commom for spin-coated perovskite films, with a rms roughness of 18.7 nm, they get considerably smoothened after nanoimprinting and their rms roughness decreases to 4.9 nm. The smoothening of the perovskite film is regarded as one of the advantages of thermal NIL as it reduces the scattering and therefore can decrease the losses of an optical mode propagating in the provskite-based waveguide.

This striking smoothening of $MAPbI_3$ thin films after imprinting is further evidenced by cross sectional SEM images which are illustrated in **Figure 4.4.3a, b**. To better illustrate the flattening of the perovskite after imprinting, I also look at samples in SEM when they are tilted by 10° (**Figure 4.4.3c, d**). Regarding these SEM images, it is obvious that rough pristine layers get remarkably flattened by the imprinting process.

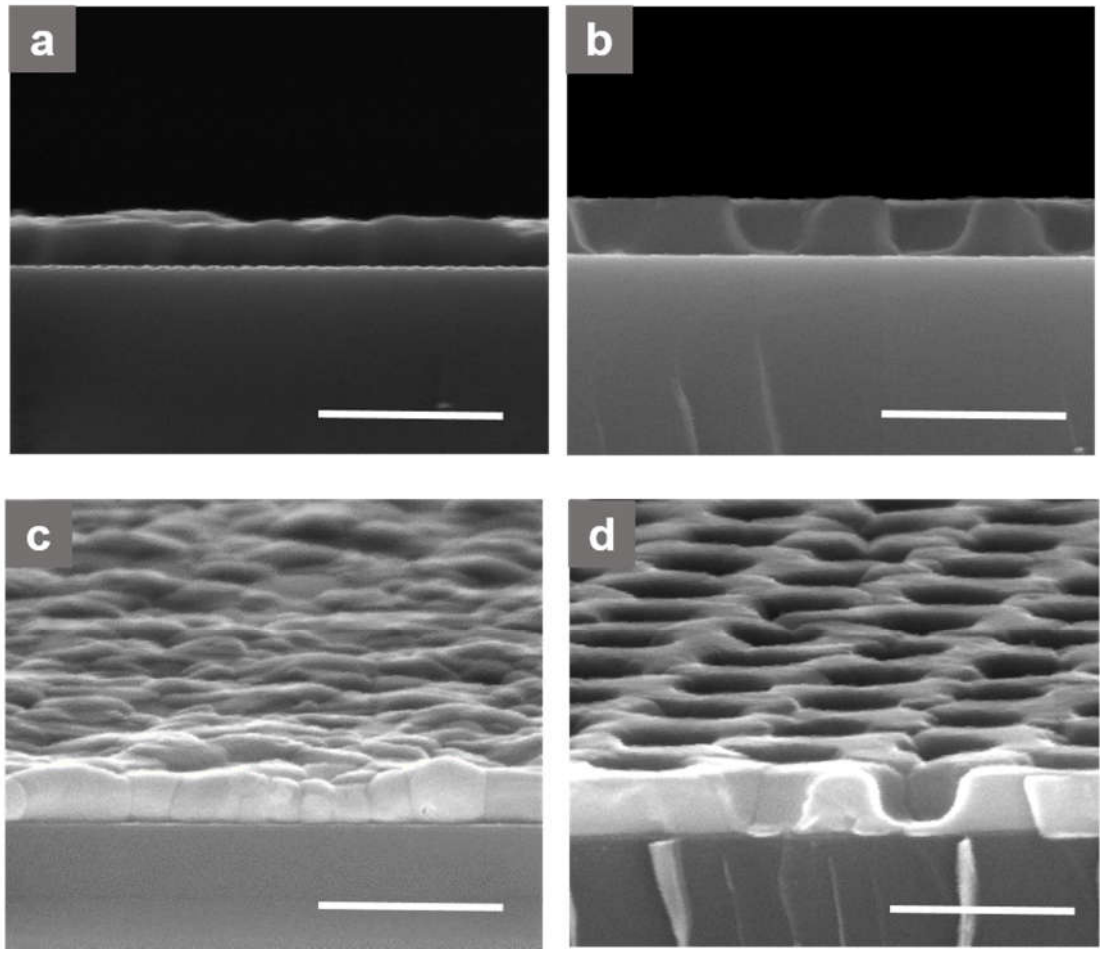

Figure 4.4.3. *Cross sectional SEM image of a, c) pristine and b, d) imprinted $MAPbI_3$ perovskite layers. In parts (c, d), the samples have been tilted by 10°. The bar in the micrographs is 500 nm.*

Furthermore, I measure the optical transmittance of as-prepared, and imprinted $MAPbI_3$ thin films. As can be seen clearly in **Figure 4.4.4,** the transmittance of the pristine layer in the sub-bandgap region ($\lambda > 790$ nm) is significantly lower than that of the imprinted layer. Typically, scattering due to layer roughness limits transmittance in this wavelength range. The higher transmittance of the imprinted layer in the sub-bandgap region, therefore, indicates substantially reduced scattering and roughness, in agreement with AFM and SEM data.

Also, the modification of the DOS in the imprinted layers can be obviously seen in the transmittance curve in comparison to that of the pristine non-imprinted layer in **Figure 4.4.4**. Notably, there are clear features of enhanced absorption at 780 nm, 796 nm and 811 nm in the spectrum of the imprinted layer as a result of the 2D-PC pattern.

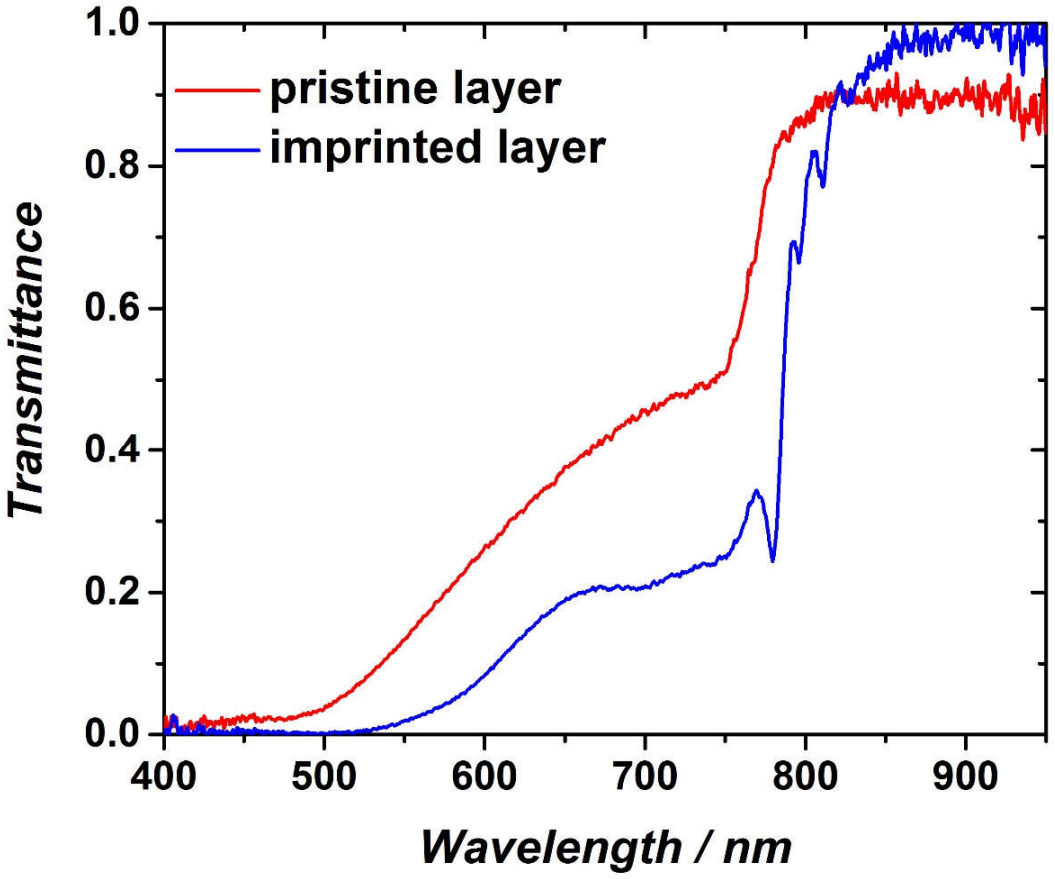

Figure 4.4.4. *Transmittance (T) spectra of a pristine and an imprinted $MAPbI_3$ layers.*

The grain size distribution, which is shown in **Figure 4.4.5**, is evaluated to characterise how temperature and pressure over imprinting influence the pristine $MAPbI_3$ grains. To measure the grain sizes, SEM images of both pristine and imprinted films are used , and the average grain size over a defined area is calculated. Based on SEM images, perovskite grain size for this process increases from 180 nm for pristine to 290 nm after imprinting. By increasing the grain sizes, the number of grain boundaries decreases which can be expected to infer a reduced contribution of surface recombination.

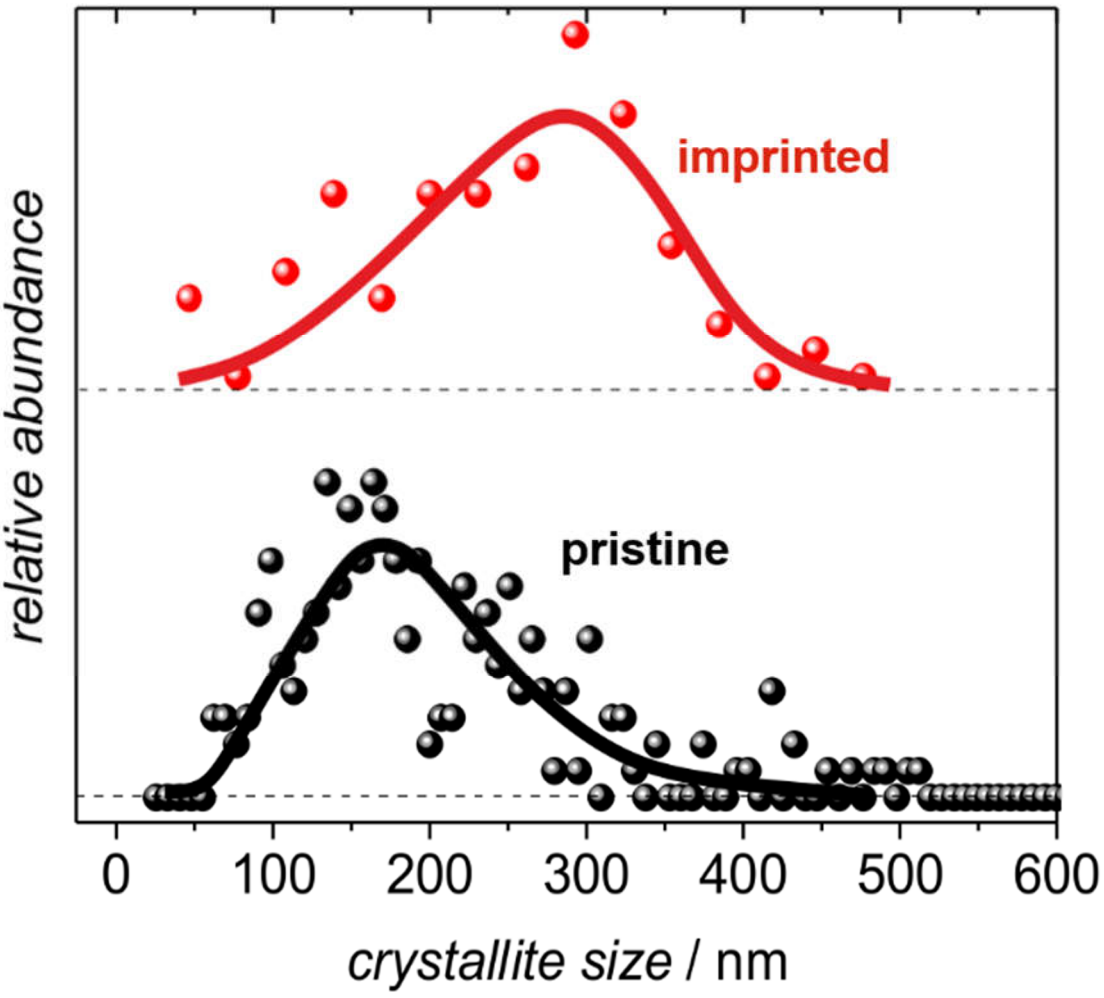

Figure 4.4.5. *Relative abundance of grains vs. size for the pristine (non-imprinted) and the imprinted samples. The two distributions have been vertically offset for clarity. The bold lines are guides to the eye.*

To undestand how the applied temperature and pressure during the imprinting process affect the crystal structure of the perovskite, the X-ray diffraction of the as-cast and imprinted layers is studied. The result of the XRD analysis is shown in **Figure 4.4.6**. As can be seen, prevailing X- ray signals in both pristine and imprinted layers are located at 14.08° and 28.36°, corresponding to the (110) and (220) planes of the tetragonal perovskite structure of $MAPbI_3$. A high degree of crystalline orientation is shown by the absence of the (002) and (004) reflections, that sometimes occur in less ordered $MAPbI_3$ layers [124]. There is also a small peak at 12.63° (with the same intensity for both pristine and flattened samples) resulting from the presence of PbI_2 within the layers which may form over XRD measurement as the samples are exposed to ambient air while being measured. This results evidence that no decomposition occurs over the NIL process.

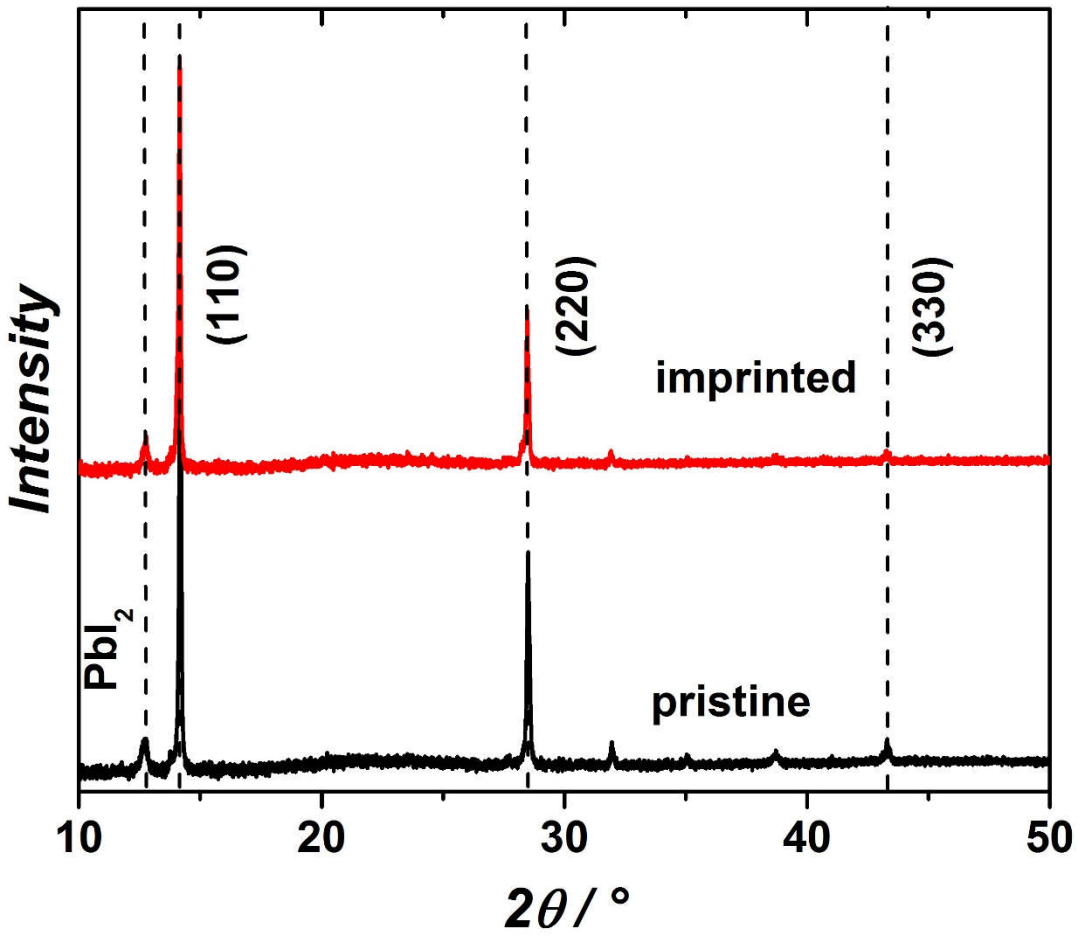

Figure 4.4.6. *X-ray diffraction of $MAPBI_3$ perovskite before and after thermal imprint.*

4.5. Stability of patterns imprinted into perovskite thin films

To investigate the stability of replicated patterns, an imprinted sample has been kept over four months under nitrogen atmosphere. Noticeably, the patterns which are imprinted into peroskite thin films remain unaltered even after four months of storage (**Figure 4.5.1**). The cracks which can be seen clearly along grain boundaries are due to the perovskite instability at grain boundaries when exposed to the electron beam under SEM measurement. Note, for practical reasons, the images have been taken at different positions on the sample.

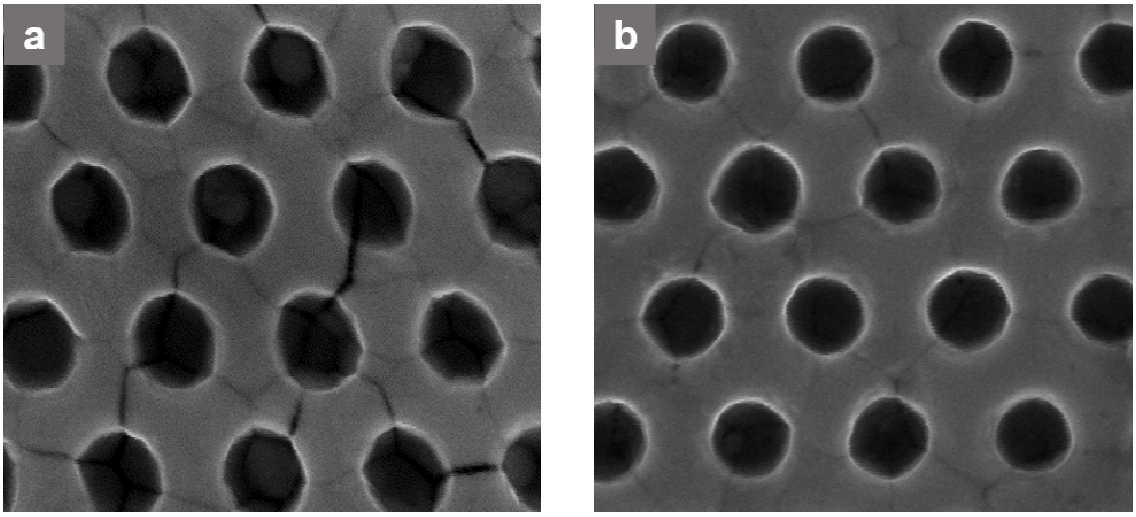

Figure 4.5.1. *SEM images of an imprinted sample a) fresh, and b) after four months of storage in nitrogen atmosphere.*

4.6. The role of imprinting on the passivation of surface defects

Apart from smoothing of the perovskite surface, it is evidenced that thermal nanoimprint has also a noticeable effect on the surface defects of the perovskite layer, which are known to function as recombination centers [125]. It has been reported by several groups that some Lewis bases and acids can be utilized to passivate these defects [126-129] among which, tri-n-octylphosphine oxide (TOPO) has been shown to be a good candidate for passivation of surface defects in as-cast polycrystalline $MAPbI_3$ [129]. It was shown that after TOPO

passivation, which could deactivate non-radiative decay pathways to some extent, there was an increase of an order of magnitude in photoluminescence (PL) intensity. It is demonstrated that passivation with TOPO has a similar effect in the as-deposited non-imprinted $MAPbI_3$ layers.

To passivate the pristine and imprinted perovskite thin films, after depositing and imprinting the perovskite layers, 70 µL of the TOPO solution is spin coated onto the perovskite layers; More details about TOPO deposition can be found in the **Appendix A/Experimental data**. After passivation, a PL measurement is done on both as-prepared and imprinted samples before and after passivation. A factor of 20 higher integrated PL intensity after TOPO passivation is confirmed for non-imprinted layers (**Figure 4.6.1a**). On the other hand, the integrated PL of the nanoimprinted sample is already about a factor of three higher than that of the passivated non-imprinted layer (**Figure 4.6.1b**). Note, the structured PL spectrum is a direct consequence of the 2D-photonic crystal pattern imprinted into the perovskite. Most strikingly, in the imprinted samples, the TOPO treatment does not have any notable further effect, and the integrated PL intensities are the same without and with TOPO passivation.

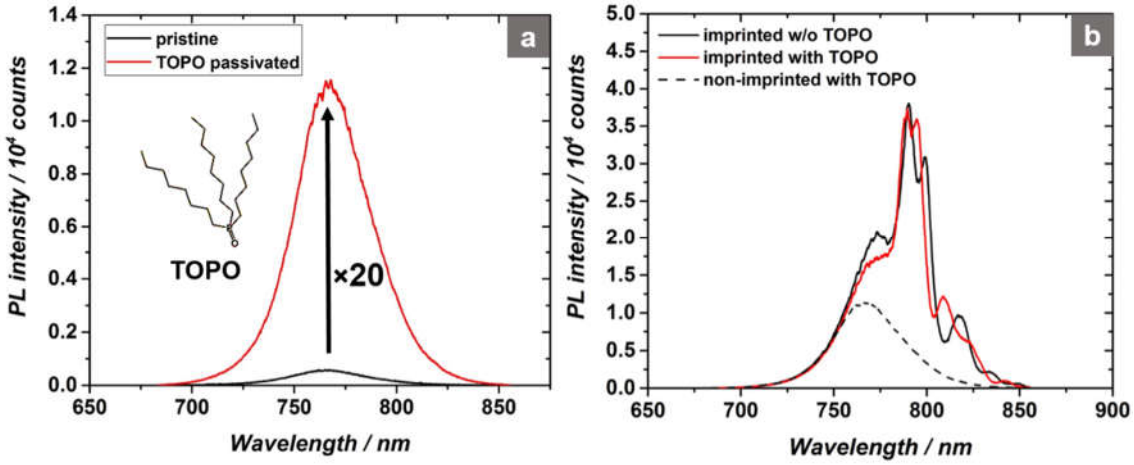

Figure 4.6.1. *a) PL spectra of non-imprinted $MAPbI_3$ layers with and without passivation with tri-n-octylphosphine oxide (TOPO). b) PL spectra of nanoimprinted $MAPbI_3$ with and without TOPO passivation. The PL spectrum of the TOPO passivated, non-imprinted sample is shown for comparison. Please note the different scale in the vertical axes (PL intensity) of part (a) and (b).*

This leads me to the conclusion that recrystallization during the NIL process signifcantly reduces the density of surface defects or reduces their detrimental impact on the recombination of charges. The somewhat different spectral shape of the PL for the sample before and after TOPO treatment is not an effect of the passivation but it can be ascribed to the fact that I am not able to measure the PL before and after passivation at the exactly same position on the sample. Slight spatial variations in layer thickness (typical for spin-coated perovskite films) lead to variations in the effective refractive index and in the photonic band-structure, which causes changes in the spectral positions of the increased optical density of states.

To further prove the passivation of defects by thermal NIL, time-resolved PL measurements are peformed. Time resolved PL transients of pristine and passivated non-imprinted layers in comparison to that of an imprinted $MAPbI_3$ layer are shown in **Figure 4.6.2**. The pristine $MAPbI_3$ shows a PL-lifetime τ_{PL} = 12.3 ns, which is more than doubled compared to τ_{PL} = 25.3 ns upon TOPO passivation of defects. Interestingly, a τ_{PL} = 21.4 ns is found for the imprinted $MAPbI_3$ which is signifcantly higher than that of the non-imprinted layer and on a similar level as the TOPO treated $MAPbI_3$ layer, corroborating the diminished importance of defects in imprinted layers.

4.7. The working principle of a 2D-PC as resonator

Figure 4.7.1 shows the imprinted triangular patterns form a 2D-PC functioning as a resonator. A schematic of the first Brillouin zone (BZ) of the photonic grating with some important points of high symmetry in k-space are marked as M, K, and Γ; M is the the center of an edge, K is the middle of an edge joining two hexagonal faces, and Γ is the center of the Brillouin zone (inset of **Figure 4.7.1**). It is known, that the working principle of a 2D-PC as a resonator is in analogy to 1D DFB resonators, where the feedback condition for the Bragg wavelength in second order is given by $\lambda_{Bragg} = n_{eff} \times \Lambda$; λ_{Bragg} is the free-space wavelength, Λ is the period of grating, and n_{eff} represents the effective refractive index of the respective optical mode propagating in the waveguide.

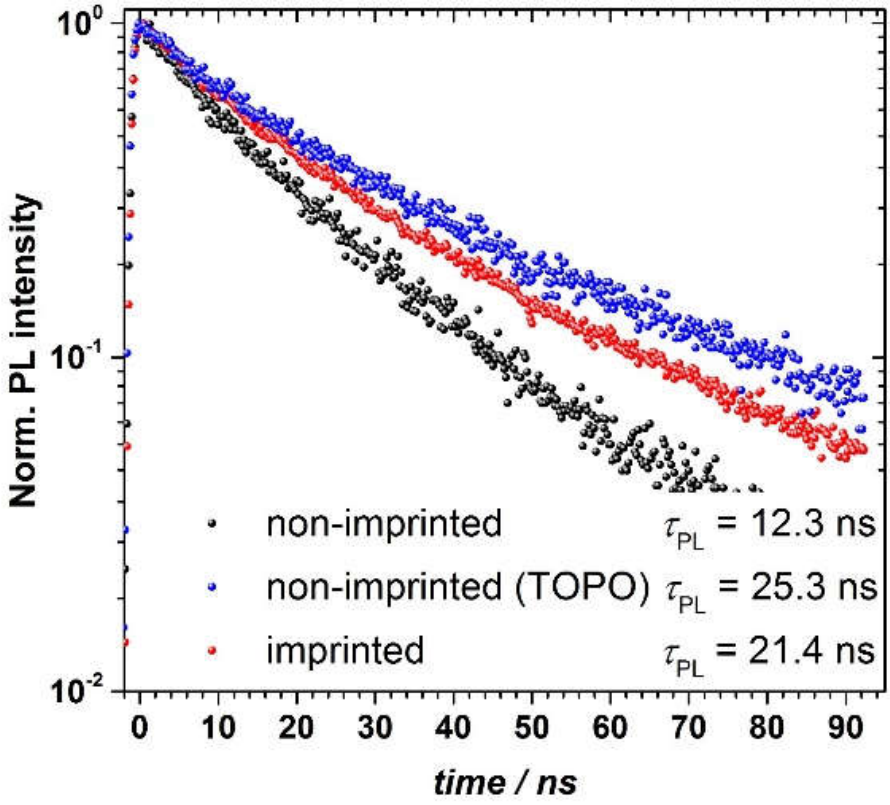

Figure 4.6.2. *Time-resolved PL of pristine and TOPO passivated non-imprinted $MAPbI_3$ layers as well as of an imprinted $MAPbI_3$ layer.*

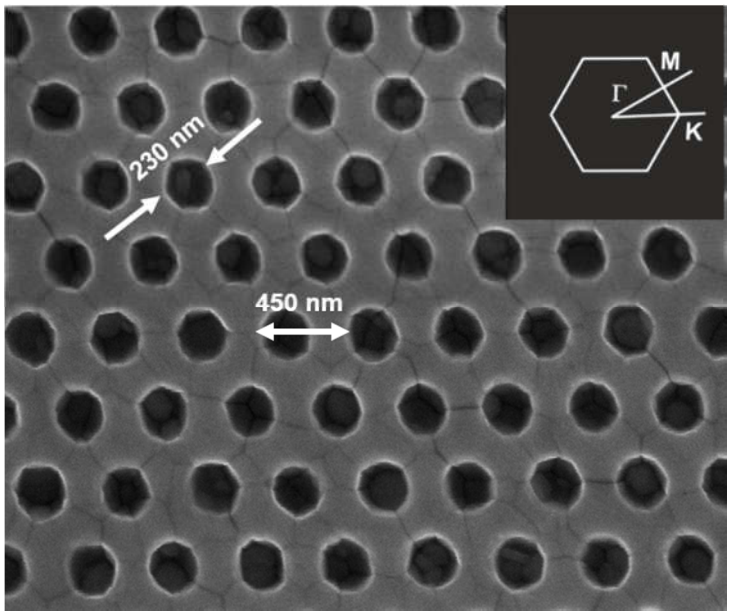

Figure 4.7.1. *SEM image of the 2D-PC with dimensions of the triangular grating. Inset: First Brillouin zone of the 2D-PC with labelled points of high symmetry.*

The laser light due to first order diffraction is coupled out in the direction normal to the surface. In a 2D-PC, depending on the difference of the refractive index Δn between the gain medium (here perovskite) and the medium in the holes (here air), a photonic bandgap opens up in the points of high symmetry of the grating (e.g., Γ). For a detailed mathematical treatment of 2D-PCs, the reader is referred to the work of Meier et al. [130]. As it has been shown, both the size of the optical gap and the concomitant enhancement of the optical DOS at the photonic band edges is increasing with increasing Δn [131]. In this regard, the relatively high refractive index of $MAPbI_3$ ($n \approx 2.7$) [9] is very beneficial. In the absence of dedicated defects in the 2D-PC, lasing will be favoured in the spectral positions of enhanced optical DOS (Referring to **Figure 4.4.4**, in the present case, the enhanced DOS can bee clearly observed at 780 nm, 796 nm and 811 nm), if these positions are matched to that of the optical gain spectrum of the active medium.

4.8. Lasing characteristics

Before demonstrating the lasing properties of my imprinted perovskite layers, I want to note, that the claim of lasing needs sound verification by a number of clearly defined indicators, as detailed by Samuel et al [132]. In the following, a range of these indicators will be addressed to provide clear evidence of lasing in the imprinted 2D-PC samples.

Figure 4.8.1 shows exemplary emission spectra of my 2D-PC perovskite upon optical pumping and the related output characteristics, i.e., light output versus pump energy density. The imprinted sample is illuminated by a 532 nm pump laser with a pulse duration of 300 ps, and a repetition rate of 1 kHz. The diameter of the pump laser spot on the sample is measured to be 0.62 mm. A clear threshold at an energy density of E_{thr} = 3.8 μJ/cm^2 is identified, which is characterised by the emergence of a spectrally narrow emission at 787.6 nm (**Figure 4.8.1a**) and a change in the slope of the output characteristics (**Figure 4.8.1b**).

The photoluminescence spectrum of a non-imprinted $MAPbI_3$ film, which is peaked at 769 nm, is added in **Figure 4.8.1a** for comparison. Even below threshold a notable

difference of the emission spectra of the imprinted sample can be found. Specifically, a pronounced Bragg-dip at λ = 778 nm indicates the modification of the optical DOS due to the 2D-PC.

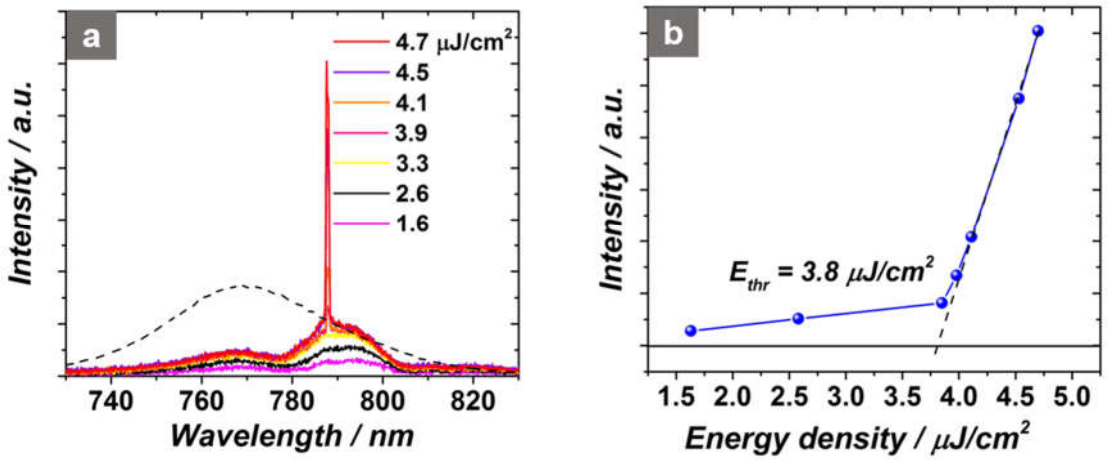

Figure 4.8.1. *a) Emission spectra upon optical pumping with increasing energy density 1.6–4.7 μJ cm^{-2}. A scaled PL spectrum of a pristine $MAPbI_3$ layer upon cw excitation is shown for comparison (dashed). b) Laser output characteristics.*

A very narrow linewidth of the laser emission is verified by high-resolution optical spectroscopy to be Δλ = 0.13 nm, limited by the resolution of the spectrometer (**Figure 4.8.2**).

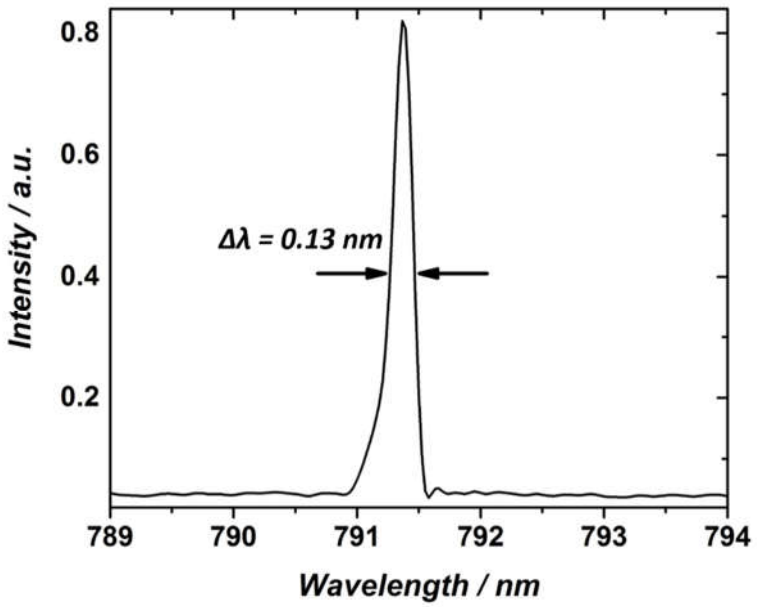

Figure 4.8.2. *Example of a laser line measured at high spectral resolution.*

It is essential to note, that the laser emission is substantially different from the ASE (**Figure 4.8.3**), which is evidenced in the non-imprinted perovskite layers. There, above a threshold of $E_{thr\ ASE}$ = 4.5 µJ cm^{-2}, I clearly detect ASE, characterised by the spectrally narrowed emission peaked at 790 nm with a full width at half maximum of 6.8 nm.

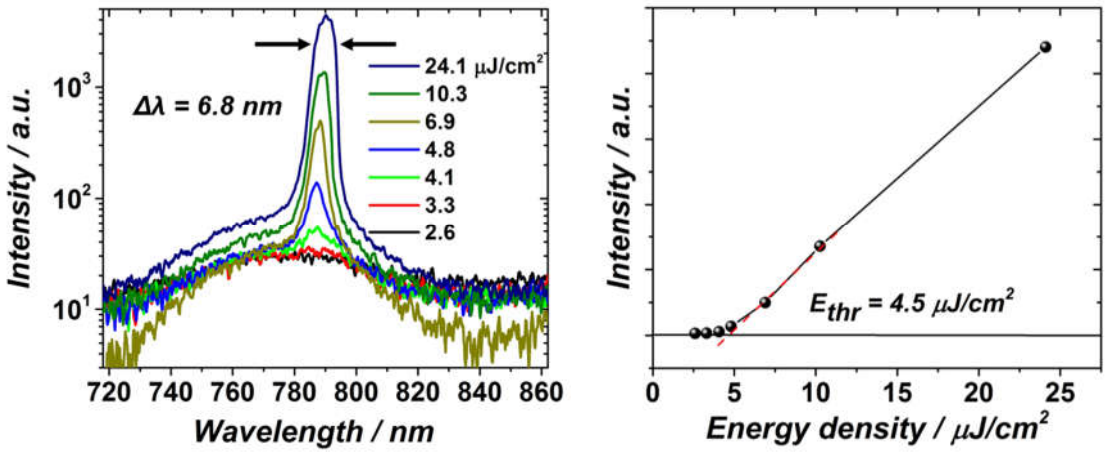

Figure 4.8.3. *ASE on a non-imprinted $MAPbI_3$ sample. a) Emission spectra and b) output characteristics.*

Note, as a feature of the 2D-PC resonator, the laser emission wavelength can be tuned between 778.8 and 800.8 nm (**Figure 4.8.4**), upon variation of the effective refractive index n_{eff}, resulting from a spatial variation of the perovskite layer thickness. **Figure 4.8.5** illustrates how the effective refractive index can undergo variations by the change of the perovskite layer thickness. The lateral dimensions of the 2D-PC are depicted in **Figure 4.8.5a**. Variations of the non-imprinted perovskite layer thickness result from a spatial inhomogeneity due to the spin-coating process (which is typical for spin-coated layers). The imprinted holes show a depth d = 140 nm regardless of the thickness (t) of the imprinted layer (**Figures 4.8.5b, c**). In a very simple estimate one can then derive the refractive index (n_{med}^{eff}) of the effective medium (perovskite, air) by a geometric weighting of the refractive index of the $MAPbI_3$ perovskite (n_p) and that of air (n_{air}):

$$n_{med}^{eff} = n_p - (n_p - n_{air})\frac{4\pi r^2 d}{3\sqrt{3}\Lambda^2 t}$$

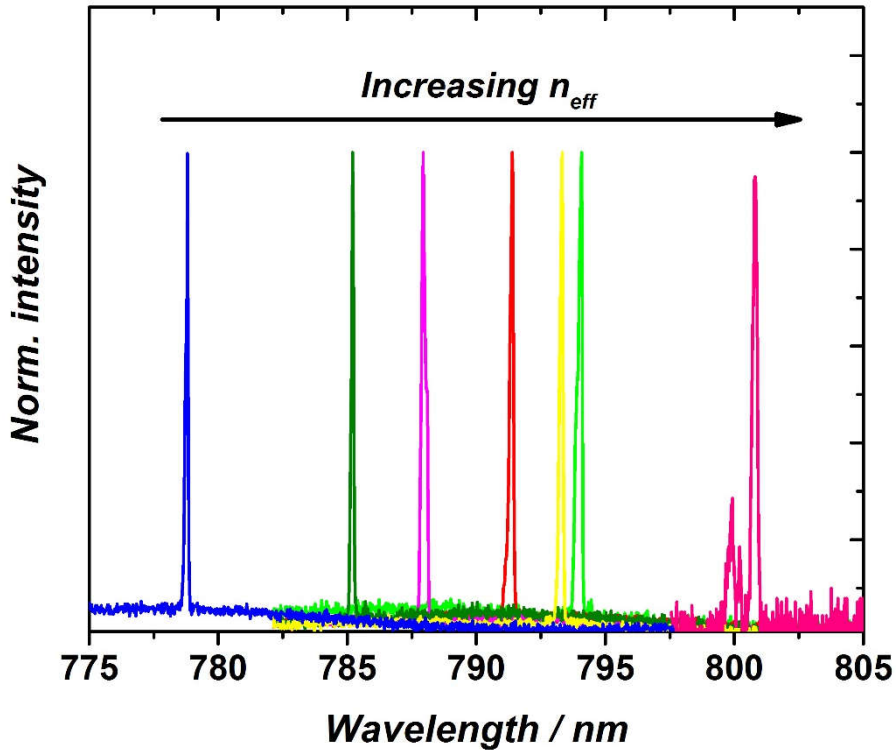

Figure 4.8.4. *Tunability of the laser emission upon variation of the position of the excitation spot on the sample. Variation in the layer thickness causes a spatial variation of the effective refractive index n_{eff}.*

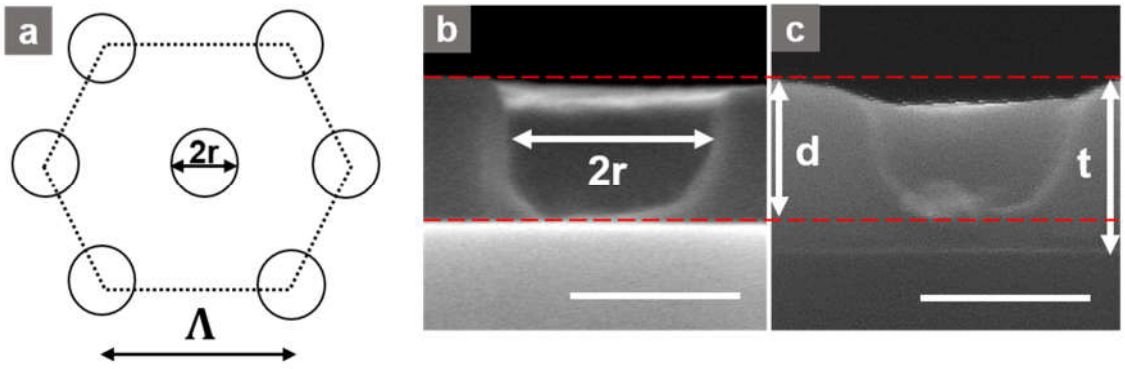

Figure 4.8.5. *a) Two dimensional schematic of the photonic crystal structure along with the characteristic dimensions. b,c) SEM cross section images of a single imprinted hole for a perovskite layer with different thickness t. Note, in (b) t ≈ d. The scale bar is 200 nm in the SEM images.*

Clearly, n_{med}^{eff} increases with increasing layer thickness (t). As the effective refractive index n_{eff} of the optical laser mode is related to n_{med}^{eff}, the tunability of the laser wavelength can be understood on this basis. The calculation of n_{eff} would require a full optical simulation of the mode structure of the photonic crystal which is beyond the scope, here.

The far field pattern of the laser below threshold is characterised by the faint, diffuse spontaneous emission, while slightly above threshold a strongly directed laser spot appears on a screen, which is positioned about 2 cm away from the laser surface (**Figure 4.8.6**).

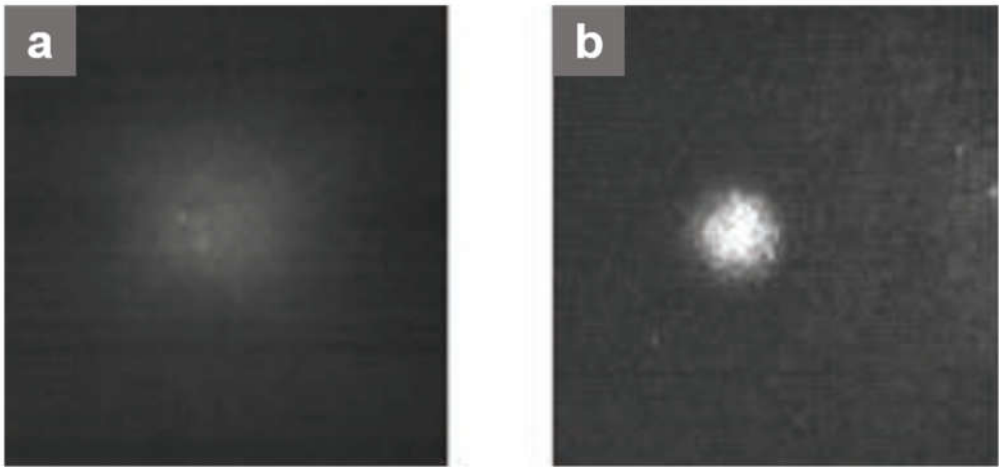

Figure 4.8.6. *The far field patterns slightly a) below and b) above threshold.*

To study the far field pattern of the laser in more detail, I further increase the pumping intensity (**Figure 4.8.7**). Aside from the central laser spot, in this photograph, the sixfold symmetry of the 2D-PC is clearly observed in the far-field. The star-shaped line features are the optical analogy to the Kikuchi lines originally reported for diffraction in electron microscopy. Here, these lines result from scattering of stimulated photons in the waveguide before they are diffracted [133].

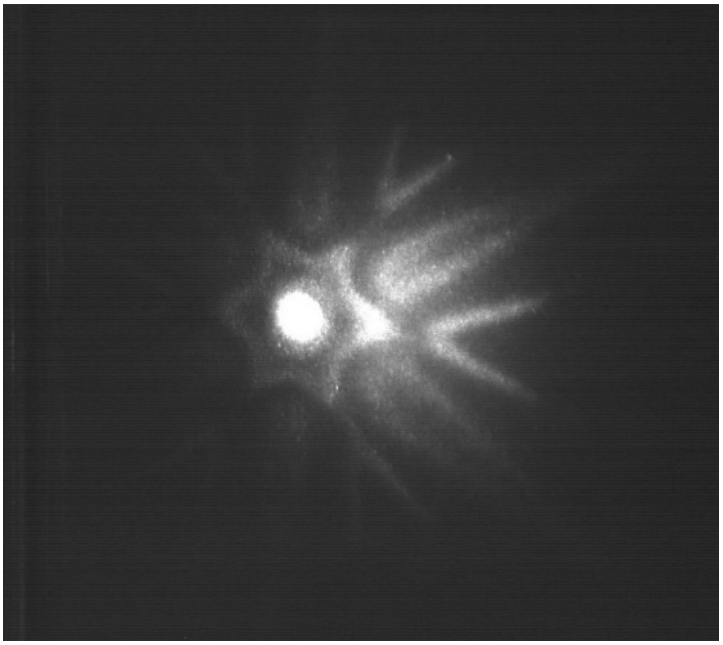

Figure 4.8.7*. Magnified view of the far-field pattern with the appearance of Kikuchi lines.*

4.9. PL and Lasing stability

The stability of the PL of the imprinted and pristine layers is studied under excitation in ambient air with a blue laser diode that provides a pulse power of about 600 mW (resulting in a power density of 80 W/cm^2). The PL of a non-imprinted and imprinted sample is measured in ambient air for 20 minutes (**Figure 4.9.1a**). As can be seen, no striking difference can be found between imprinted and pristine samples. The PL of the imprinted sample shows some increase by about 10% in the first five minutes. Similar "light-soaking" effects have been observed earlier [118]. To provide further information about the stability of the imprinted lasers under operation, I study the lasing of the imprinted sample over a time scale of more than 8 hours (>5×10^5 pulses) at about 15% above threshold without notable degradation (**Figure 4.9.1b**). The results of these orienting experiments are very encouraging and point to a significantly higher stability of perovskite lasers compared to those based on typical organic gain media [134]. This result is also in agreement with reports of highly stable perovskite lasers [135].

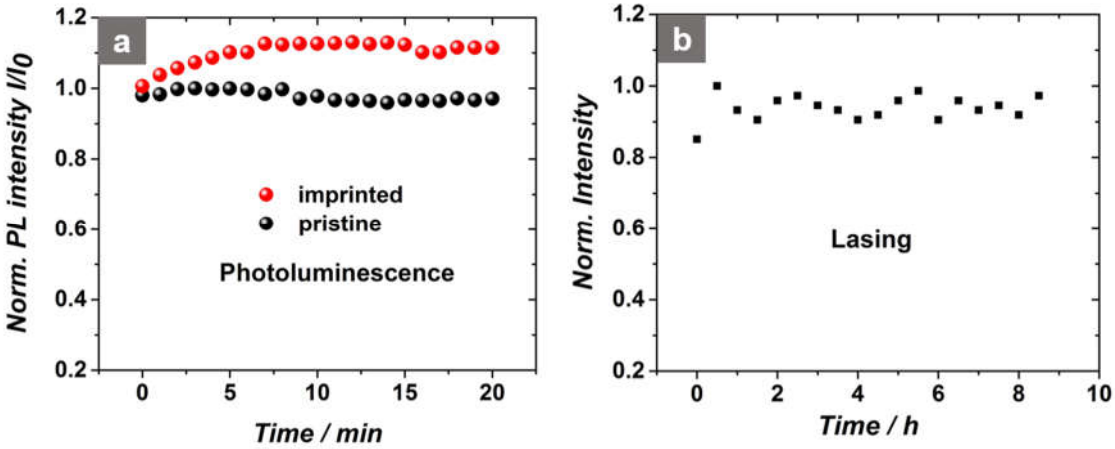

Figure 4.9.1. *a) Integrated PL intensity of the pristine and imprinted samples under excitation in ambient air with a blue laser diode (λ = 450 nm) that under pulsed operation provides a pulse power of about 600 mW and a power density of 80 W/cm^2. The integrated intensity has been normalized to that at the beginning of the experiment (I_0). b) Long term stability study of the sample under lasing conditions (1.15 × threshold) in nitrogen atmosphere.*

4.10. Summary

In this chapter, 2D photonic-crystal lasers, prepared by direct thermal nanoimprint lithography into a spin-coated layer of a methylammonium lead iodide perovskite, are demonstrated. Thermal imprint, at a temperature as low as 100 °C (used commonly for fabricating solar cells), is shown to transfer perfectly and homogeneously the nanopattern of the stamp via recrystallization of the perovskite over the area of the imprint region of 15 × 15 mm^2. Moreover, the resulting layers are significantly smoothened with respect to the pristine polycrystalline perovskite layer, which is beneficial for low propagation losses of wave-guided optical modes in the perovskite layer. In addition, surface defects which cause substantial recombination and luminescence quenching are eliminated by the recrystallization upon thermal imprint.

Taken together, the resulting 2D-PC lasers show low lasing thresholds of 3.8 μJ cm^{-2}. Apparently, organo-lead halide perovskites combine optoelectronic properties known

from the best crystalline inorganic semiconductors with the ease of patterning known from soft-matter like polymers. I believe this insight will provide an avenue to pattern these perovskites for photonic applications beyond lasers.

Chapter 5

$MAPbBr_3$-based DFB Laser

5.1. Introduction

Beyond $MAPbI_3$ which was demonstrated in **Chapter 4**, perovskite gain media like $MAPbBr_3$ with a larger bandgap and an emission in the visible spectral range would be very attractive for lasing applications. This class of perovskite bears the potential to cover the spectral region known as the "green-gap" [22], which is difficult to address at room temperature with established inorganic semiconductor gain media, such as InGaN or AlGaInP.

In this chapter, the first DFB laser based on $MAPbBr_3$ thin films, with a linear photonic grating imprinted into the $MAPbBr_3$ active layers is presented. Bragg resonator gratings with a periodicity of 300 nm are directly patterned by thermal nanoimprinting into thin films of $MAPbBr_3$ at a temperature as low as 100 °C to form a second-order DFB resonator. In the fabricated optically pumped DFB laser structures, very low lasing thresholds of 3.4 μJ/ cm^2 are achieved which is indicative of the outstanding material quality of the imprinted $MAPbBr_3$ layer.

Note, this chapter is based on my previously published journal article **"Distributed Feedback Lasers Based on $MAPbBr_3$", Adv. Mater. Technol., 2018, 3, 1700253.**

5.2. Pristine $MAPbBr_3$ layer preparation

$MAPbBr_3$ thin films used in my study are prepared from a solution of $Pb(Ac)_2$ and anhydrous CH_3NH_3Br in anhydrous DMF which is explained in more details in **Appendix A/Experimental data**. As displayed in Figure 5.2.1, the spin-coating process results in a very rough polycrystalline perovskite $MAPbBr_3$ layers, similar to the results shown for $MAPbI_3$ layer shown above. These layers are the starting layers on which an imprint process will be done

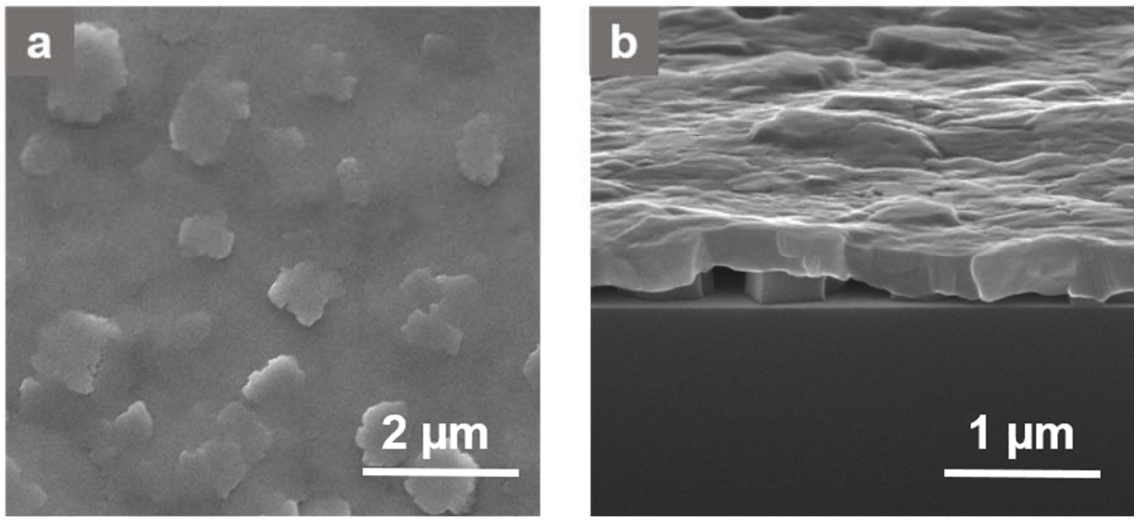

.

Figure 5.2.1. *a) Plan view, and b) cross sectional SEM images of an spin-coated $MAPbBr_3$ layer.*

5.3. Thermal nanoimprint lithography (NIL) process

The stamp, which is used for nanoimprint features 150 nm lines and spaces (**Figure 5.3.1**). The height of the ridges is 100 nm.

The thermal imprint process follows a temperature/pressure sequence as depicted in **Figure 5.3.2**. Further details of the NIL process and stamp preparation can be found in **Appendix A/Experimental data**. Essentially, I apply a prepressure of 25 bar before starting the heat-up procedure to the desired imprint temperature of 100 °C. The duration of the imprint is 3 min. Finally, the pressure is slowly released after cooling the sample to 30 °C.

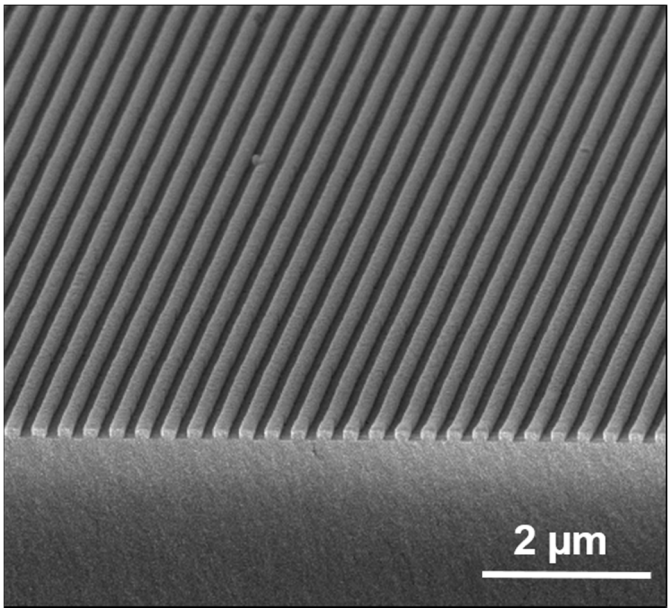

Figure 5.3.1. *NIL stamp with a linear grating with a pitch of Λ = 300 nm.*

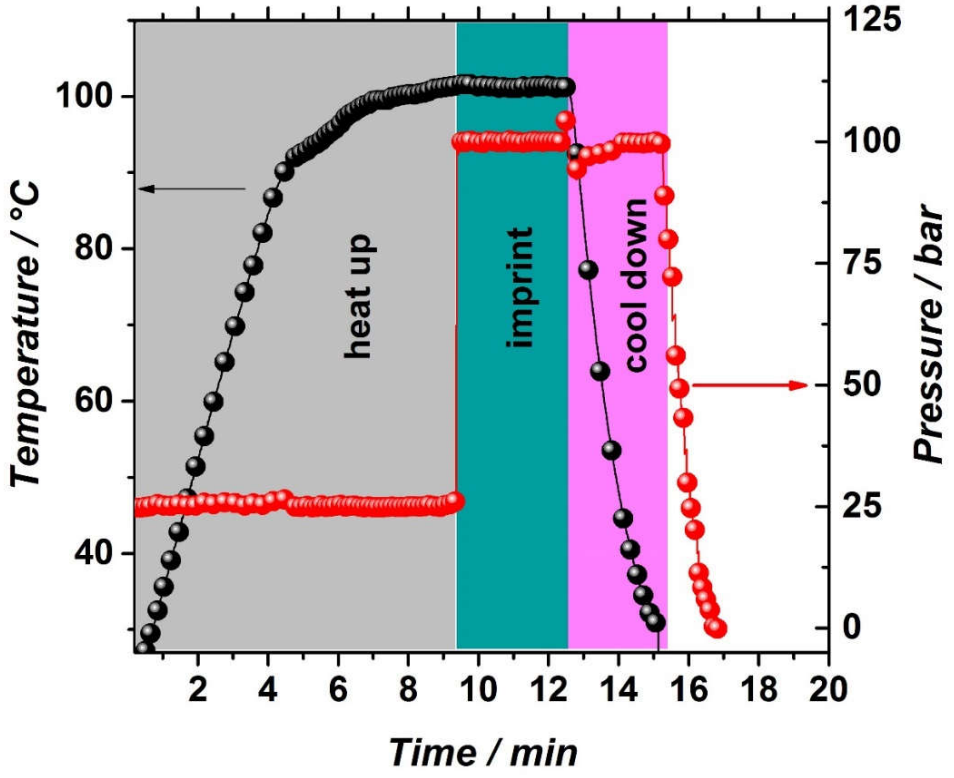

Figure 5.3.2. *Protocol of the imprinting process showing the temperature and pressure versus time.*

To demonstrate the quality of nanoimprinting, I perform SEM on imprinted perovskite layers. As can be seen from the SEM plan view in **Figure 5.3.3a**, the grating pattern of the stamp is perfectly replicated into the $MAPbBr_3$ film even on a large area. According to the cross sectional SEM image illustrated in **Figure 5.3.3b**, the imprint depth is measured to be 100 nm, as expected regarding the height of the ridges, shown in **Figure 5.3.1**.

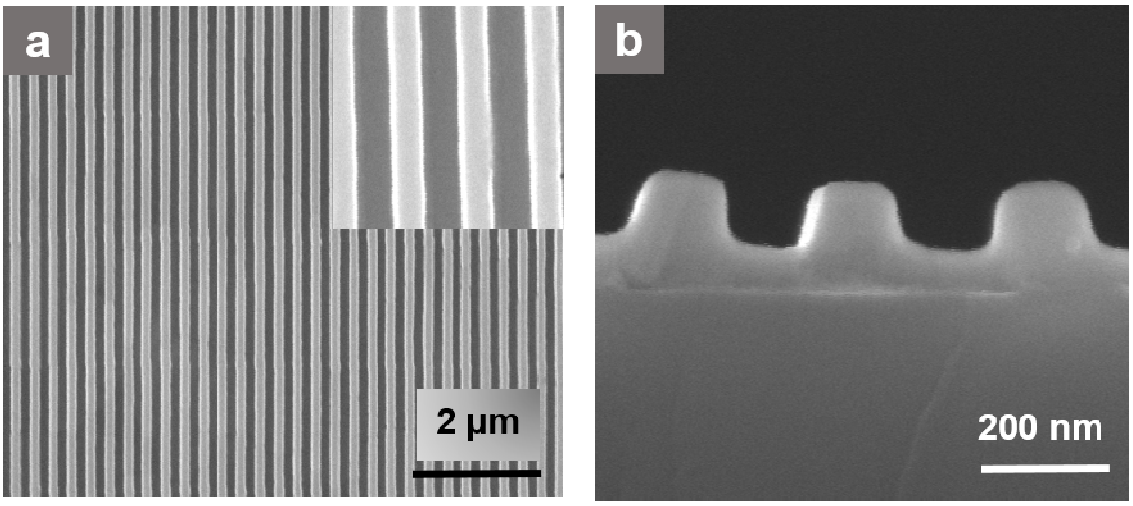

Figure 5.3.3. *a) Plan view SEM of the $MAPbBr_3$ imprinted layer (inset: magnified view). b) Cross sectional SEM image of the $MAPbBr_3$ imprinted layer.*

5.4. Perovskite thickness adjustment

The desired thickness of the perovskite layer is subject to the design considerations of planar optical waveguides based on $MAPbBr_3$ (**Figure 5.4.1**). A transfer-matrix calculation is used to simulate the light propagation in the optical waveguide. The calculation is done by taking the imprinted layer as an effective medium of $MAPbBr_3$/air as shown in the inset of **Figure 5.4.1**. Considering the imprinting depth of 100 nm and the refractive index of $MAPbBr_3$ of $n = 2.26$ at $\lambda = 550$ nm [136], a single TE0 mode would be supported for perovskite layers with an initial thickness of 60–200 nm, which after imprinting of the grating results in a height of the hills of 110–250 nm. For thicker layers, the onset of a second mode (TE1) is found.

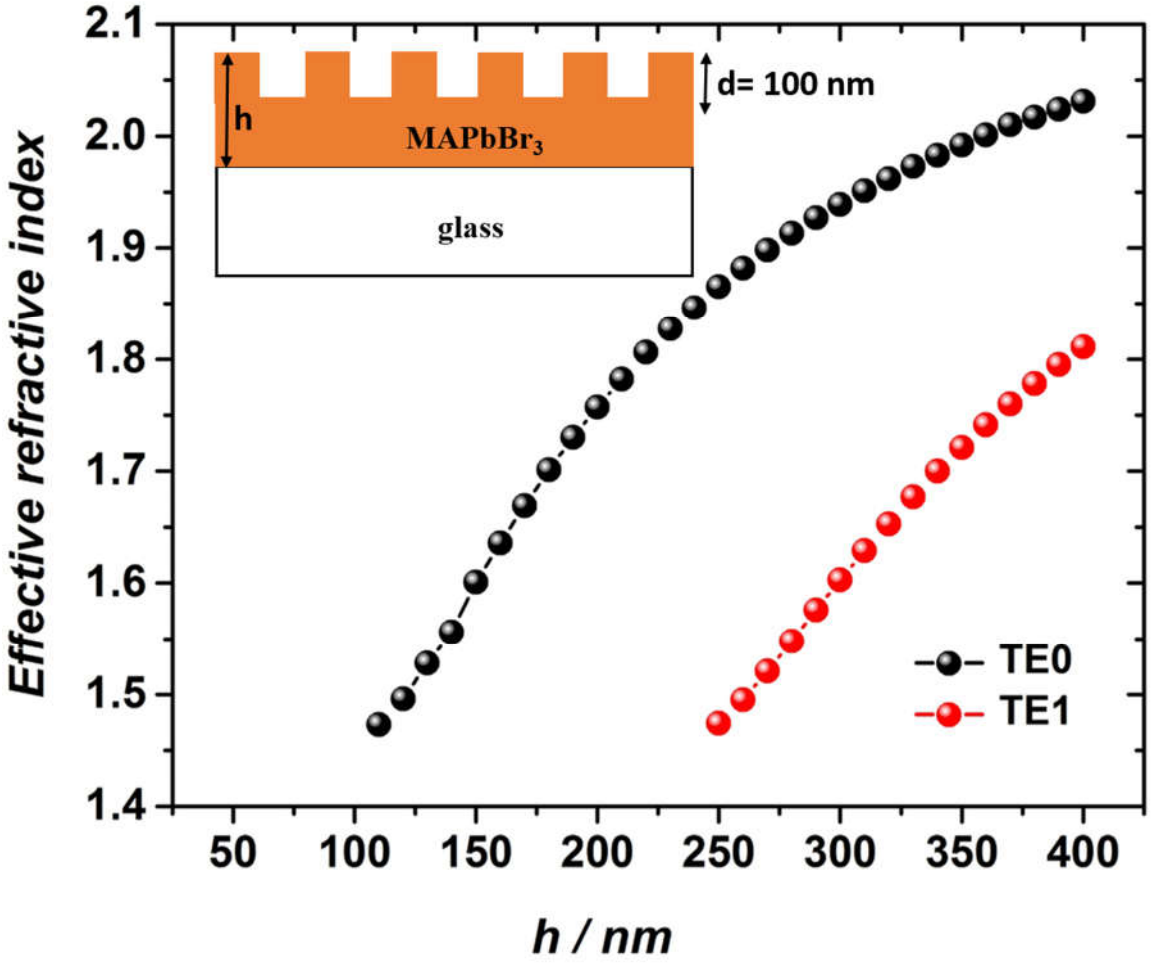

Figure 5.4.1. *Effective refractive index (n_{eff}) of TE modes guided in the imprinted $MAPbBr_3$ layer. The inset shows the schematic of the $MAPbBr_3$ imprinted layer.*

5.5. The effect of NIL on perovskite morphology and crystallinity

5.5.1. Grain size

A statistical assessment of the grain size distribution is presented in **Figure 5.5.1.1** to demonstrate how temperature and pressure, which are applied over imprinting, affect the spin-coated $MAPbBr_3$ morphology. The resulting histograms are shown in **Figure 5.5.1.1e, f**. From the SEM images, the average grain area is calculated to be 0.7 μm^2 and 6.5 μm^2 for the pristine and the imprinted layers, respectively.

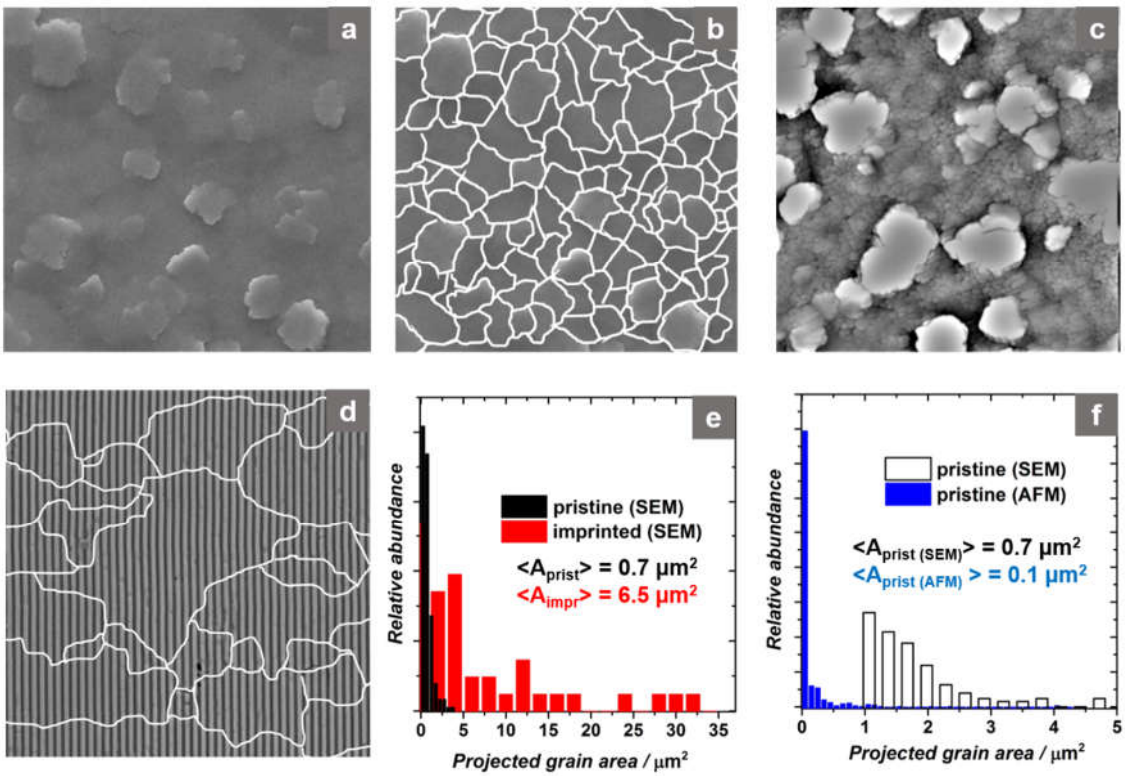

Figure 5.5.1.1. *a,b) SEM image of a pristine $MAPbBr_3$ layer with and without manually highlighted grain boundaries. c) AFM image of a pristine $MAPbBr_3$ layer with contrast and brightness levels tuned to best visualize the individual grains (different position on the sample as in a, b). d) SEM image of the DFB grating imprinted into the $MAPbBr_3$ with manually highlighted grain boundaries. e, f) Relative abundance of grains vs. projected gain area as determined from the images (a-d) using image processing software.*

I have to note that the meaningful determination of grain size statistics from the SEM images is limited by the resolution of the SEM if I intend to detect large and small grains in one image. This issue becomes obvious, if the SEM and AFM images are compared (**Figure 5.5.1.1b, c**). The AFM image reveals that the pristine layers consist of few larger grains but a vast majority of smaller grains that are not well resolved in the SEM images. As a result, the average grain area in the pristine layers according to the AFM data is 0.1 μm^2, much smaller than the 0.7 μm^2 determined from the SEM data of the same layer. It is very instructive to determine the area which is larger than that of 80% of the grains (80% level) in the respective layers. For the pristine layer, 80% of all grains have an area

of 0.8 μm^2 or less when derived from the SEM image, and 0.05 μm^2 or less when derived from the AFM image. No grains larger than 5 μm^2 could be detected for the pristine layers. For the imprinted layer, the 80% level is 12 μm^2. Therefore, it can be concluded that the imprinting process turns the pristine layers consisting of small grains to layers consisting of large crystals on the order of tens of microns.

5.5.2. Crystallinity

To determine how the imprinting process influences the crystal structure of $MAPbBr_3$ perovskite thin films, the X-ray diffraction of pristine and imprinted layers is analysed (**Figure 5.5.2.1**).

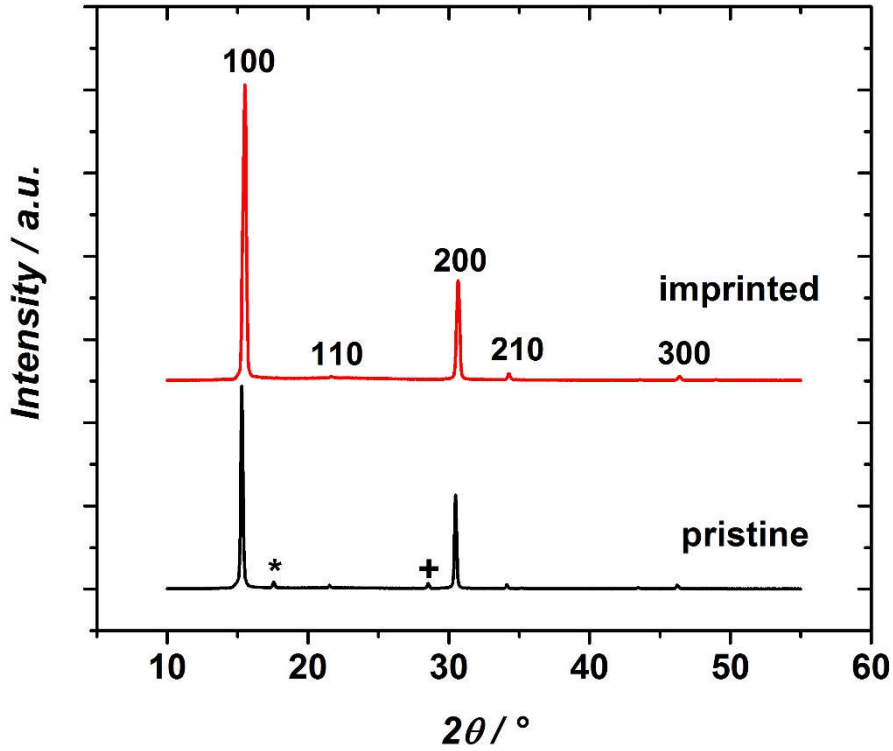

Figure 5.5.2.1. *XRD diffractograms of the pristine and imprinted $MAPbBr_3$ perovskite layers with assignment of the most relevant peaks.*

The corresponding diffractograms show dominating signals due to the 100 and 200 planes of the cubic $MAPbBr_3$ structure in agreement with the literature [137]. These prevailing

reflections indicate the preferred a-axis orientation of the crystals in the layers. The 100 and 200 peaks are substantially more intense in the recrystallized imprinted samples compared to the pristine ones. This result can be understood if I compare the cross sectional SEM micrographs of the pristine and imprinted layers (**Figures 5.2.1b** and **5.3.3b**, respectively). While the pristine layers show some notable inhomogeneity also in vertical direction (i.e., normal to the sample surface), the crystals extend over the entire layer thickness in the imprinted sample.

As such, I interpret the more intense X-ray diffraction (XRD) reflection peaks as a result of the improved crystallinity in the imprinted layers. Note, in the pristine layers, I identify two peaks labeled with (*) and (+), that cannot be associated with the $MAPbBr_3$ perovskite or $PbBr_2$ [138, 139]. These peaks are absent in the imprinted layers. The positions of these peaks agree with reports on diffraction peaks of lead acetate and may thus indicate the presence of some precursor traces in the pristine layers [140].

5.6. Planar hot pressing (PHP)

5.6.1. PHP process

Before characterising the lasing properties, in order to better understand the impact of the imprinting process in more depth, a flat stamp without any pattern is used to identify the structural changes inferred by what we call a planar hot pressing (PHP) process, schematically shown in **Figure 5.6.1.1**. The PHP procedure follows the protocol outlined in **Figure 5.3.2** except the temperature was set to 150 °C for this special presented example. Note, no noticeable variation of the optical properties is observed for temperatures in the range of 100 to 150 °C.

5.6.2. The effect of PHP on perovskite morphology

To demonstrate the surface morphology, atomic force microscopy is performed on both pristine and hot pressed $MAPbBr_3$ layers, illustrated in **Figure 5.6.2.1**. As can be seen,

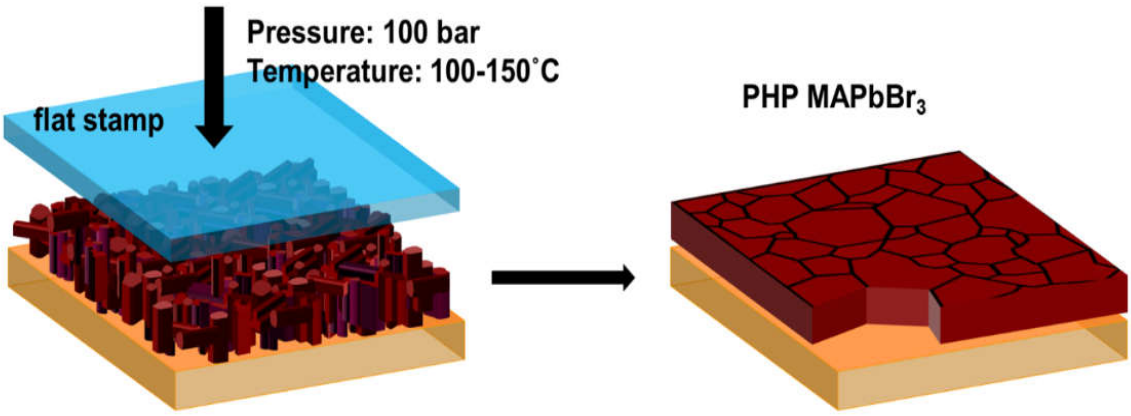

Figure 5.6.1.1. *Principle of the planar hot pressing (PHP) process using a flat stamp for the imprint procedure.*

the pristine $MAPbBr_3$ layers are very rough (rms roughness: 46 nm), which is a common finding for spin-coated $MAPbBr_3$ [20, 141]. Most strikingly, these initially very rough layers are dramatically flattened by the PHP process.

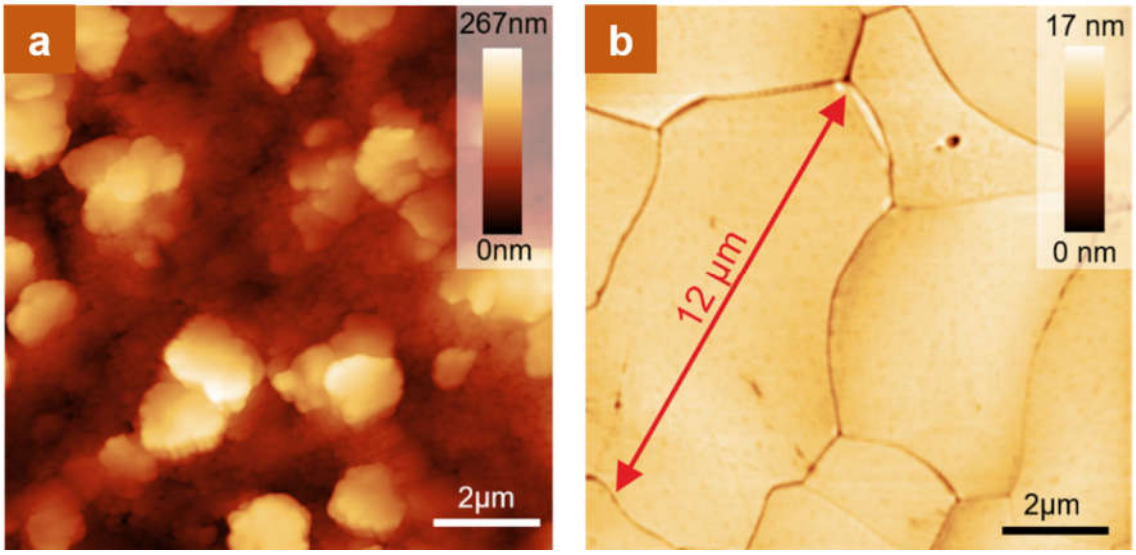

Figure 5.6.2.1. *AFM image of a) pristine and b) PHP $MAPbBr_3$ layers.*

The initial assembly of relatively small crystallites is transformed to a dense tiling of large crystals with lateral dimensions on the order of 10 µm, and the surface roughness of the large crystal grains is as low as 0.6 nm (rms). This residual roughness is identical to that found for the flat silicon stamp which was provided with an antisticking layer. (**Figure 5.6.2.2**).

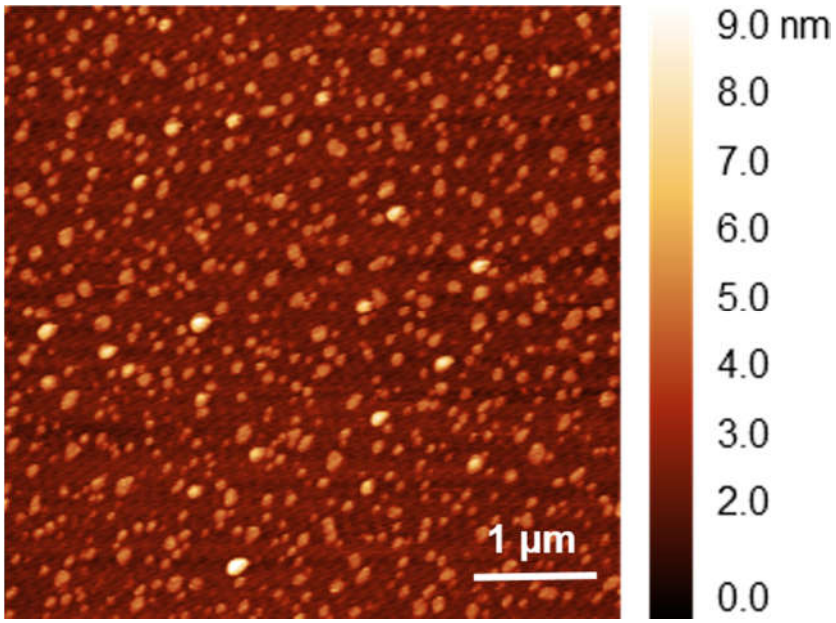

Figure 5.6.2.2. *AFM image of silicon stamp used for PHP process.*

In addition, a SEM image of the cross section reveals that the individual crystals indeed extend down to the substrate (**Figure 5.6.2.3**), While the pristine layers show noticeable inhomogeneity in vertical direction (**Figures 5.2.1b**).

5.6.3. Crystallinity and stability

A notable difference between pristine and PHP layers is the substantially more intense XRD peaks of the PHP perovskite (showing the improved crystallinity after PHP process which can be figured out from SEM images of the pristine and the PHP layers in **Figures 5.2.1b** and **5.6.2.3**, respectively) and a significantly increased environmental stability of

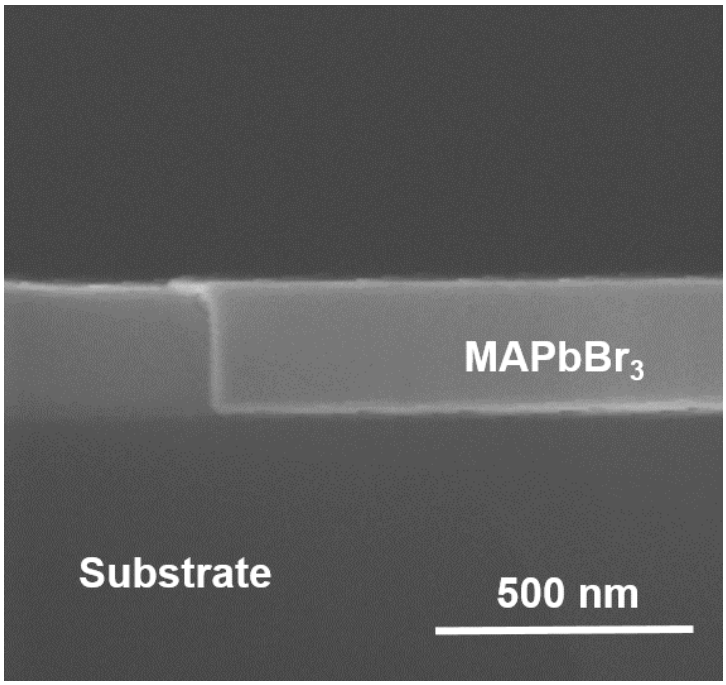

Figure 5.6.2.3. *SEM cross sectional image of a PHP $MAPbBr_3$ layer on a Silicon substrate.*

the PHP layers, which can be seen clearly through XRD diffractograms of pristine and flattened $MAPbBr_3$ layers in **Figure 5.6.3.1**. The fresh pristine layer shows the main reflections attributed to the $MAPbBr_3$ perovskite. After two days storage in air, the $MAPbBr_3$ reflections decay by almost an order of magnitude. Opposed to that, the fresh PHP $MAPbBr_3$ layers show reflections which are an order of magnitude more intense than those of the fresh pristine layers. Moreover, even after 7 days of storage in air no substantial decay of the intensity of these reflections is observable for the PHP $MAPbBr_3$ sample. Earlier reports have evidenced that $MAPbI_3$ layers with larger crystal grains were more stable upon exposure to ambient air [142].

5.6.4. Optical attributes

The flattening of $MAPbBr_3$ thin films after the planar hot pressing process and thus the reduced scattering is evidenced in the optical reflectance spectra of the pristine and the PHP layers (**Figure 5.6.4.1**). In the sub-bandgap region (λ > 630 nm), where the

absorption due to the perovskite is absent, the ratio of diffuse reflectance (R_{diff}) and total reflectance (R_{total}) for the pristine and the flattened sample is 65% and 26%, respectively.

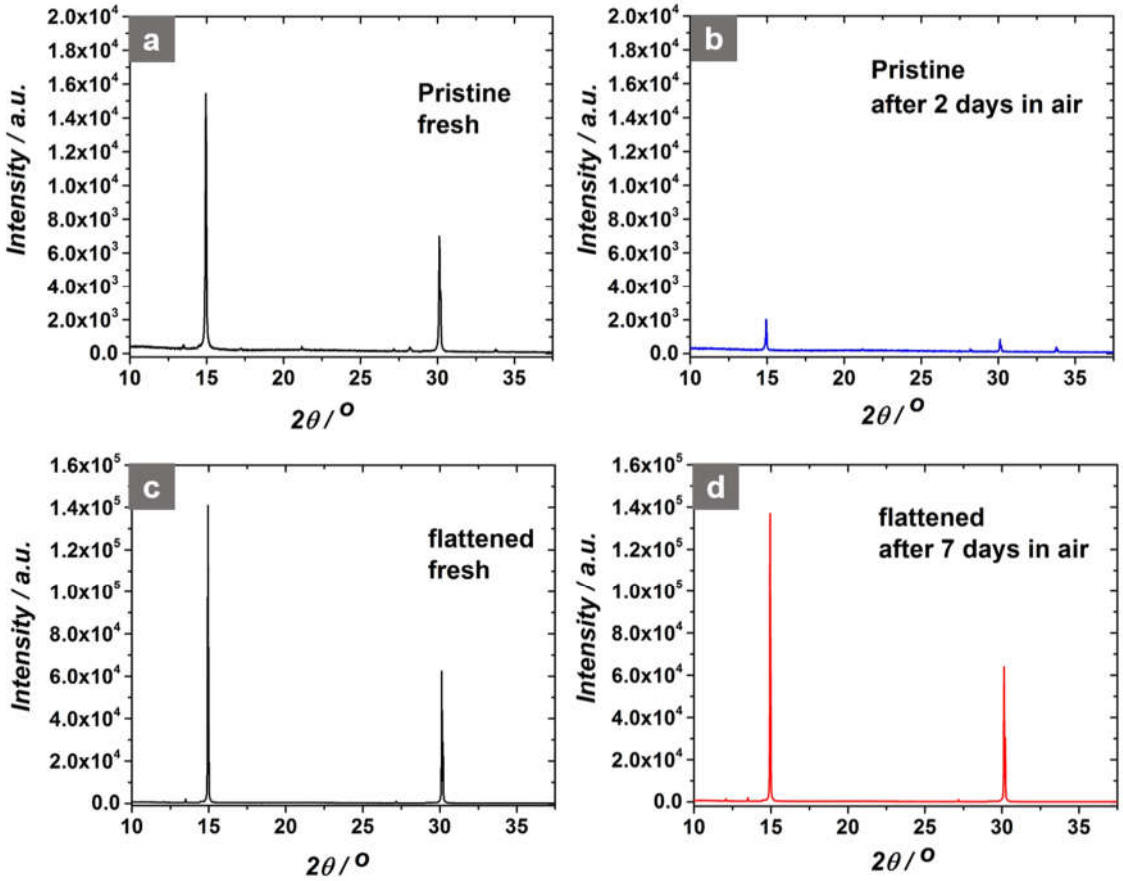

Figure 5.6.3.1. *XRD diffractogram of a pristine MAPbBr$_3$ layer, a) fresh, and b) after storage in air for 2 days. XRD diffractogram of a PHP MAPbBr$_3$ layer, c) fresh, and d) after storage in air for 7 days.*

The PLQY for both pristine and planar hot pressed $MAPbBr_3$ thin films is also measured. For both pristine and flattened layers, the PLQY is about 5% at an excitation density of 286 mW/cm^2 at 450nm.

To further investigate the impact of planar hot pressing on the optical properties, the ASE which is an important prerequisite for lasing is studied. The ASE for both pristine and PHP $MAPbBr_3$ layers is measured upon optical excitation with a 532 nm pulsed laser

with a pulse duration of 0.3 ns, and a repetition rate of 1 kHz (**Figure 5.6.4.2**). In a striking difference, the threshold for the onset of ASE in the flattened PHP MAPbBr$_3$ layers is 11 µJ/cm^2, significantly lower than that found in the pristine layers (61 µJ/cm^2). As the PLQY for both pristine and PHP MAPbBr$_3$ layers are the same, this substantially reduced ASE threshold in the flattened PHP MAPbBr$_3$ layers can be related to the significantly reduced losses due to scattering.

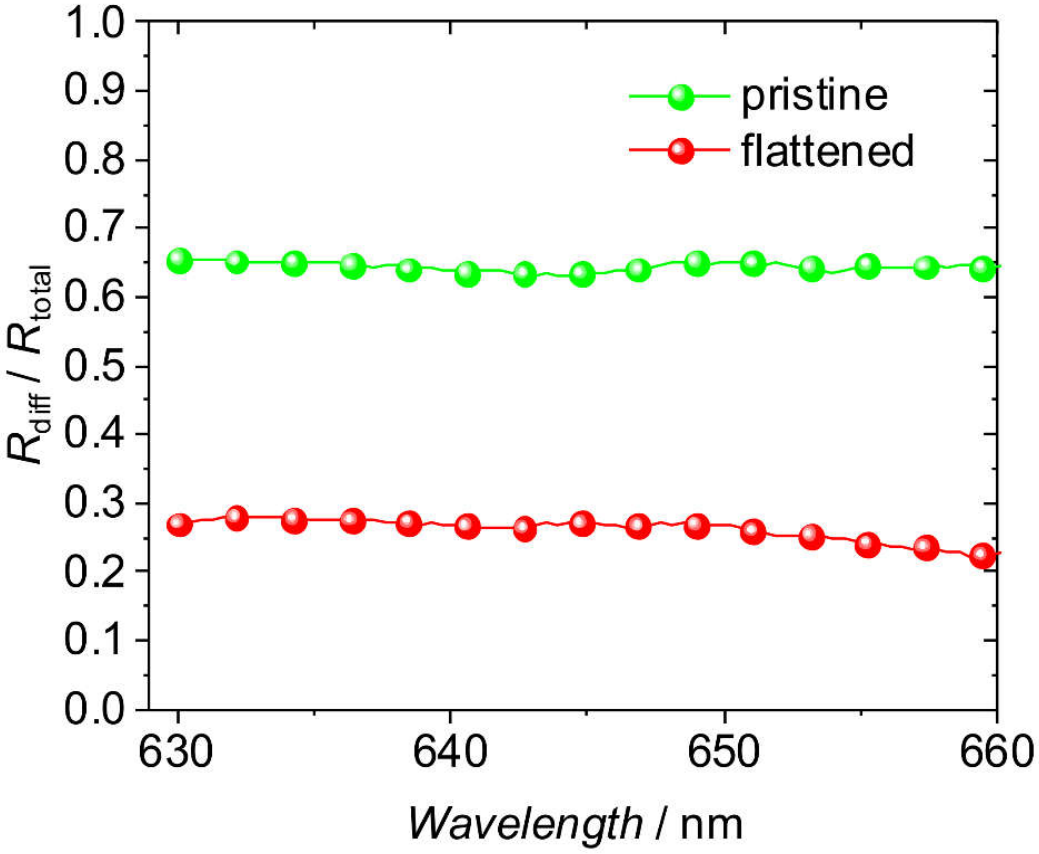

***Figure 5.6.4.1**. Diffuse reflectance (R_{diff}) vs. total reflectance (R_{total}) of pristine spin-coated MAPbBr$_3$ layers and MAPbBr$_3$ layers that have been flattened by PHP process. The spectral range of the measurement is below the band-gap of MAPbBr$_3$, where the material absorption is absent.*

The corresponding emission spectra below (PL) and above the ASE threshold are exemplary shown in **Figure 5.6.4.3**. The determined width of ASE is $\Delta\lambda = 2.5$ nm which is clearly much narrower than that of the PL.

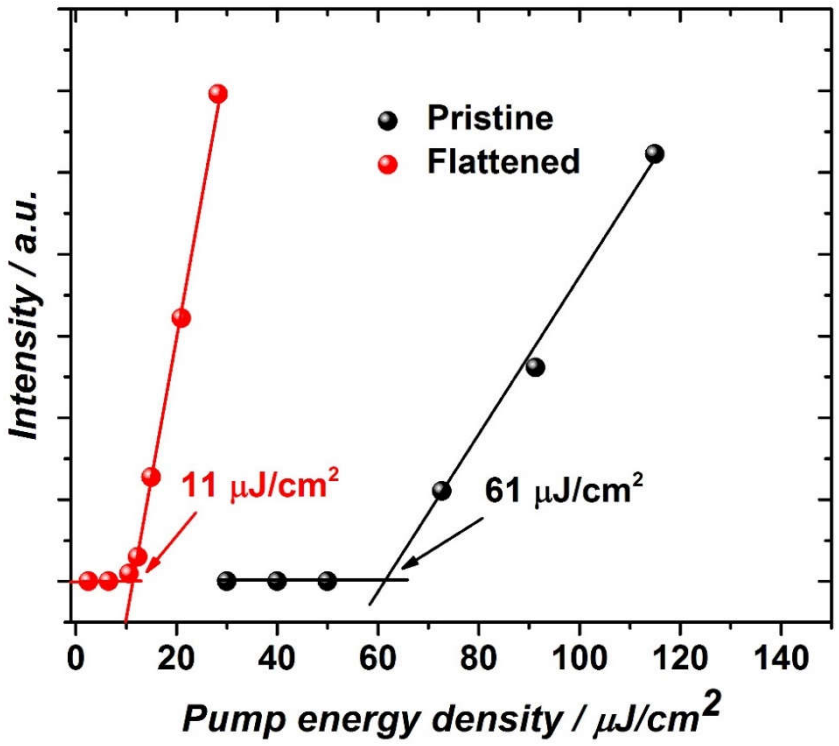

Figure 5.6.4.2. *Comparison of the output characteristics of pristine and PHP $MAPbBr_3$ layers upon optical pumping with increasing the energy density. The threshold for the onset of ASE is marked.*

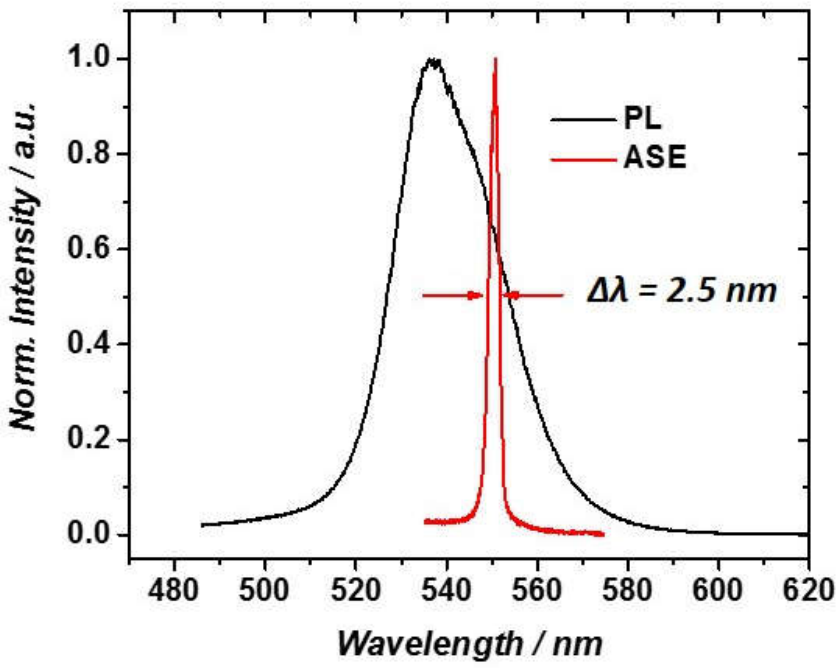

Figure 5.6.4.3. *Emission spectra of a flattened $MAPbBr_3$ layer below (PL) and above the ASE threshold.*

5.7. Lasing characteristics

In the following, the indicators introduced by Samuel et al. [132] will be investigated to prove the claim of lasing in my imprinted $MAPbBr_3$ thin films. Representative spectral emission characteristics of the $MAPbBr_3$ DFB laser upon increasing the optical excitation density from 0.5 to 5 μJ/cm^2 are shown in **Figure 5.7.1a**. At an excitation density in excess of 3.4 μJ/cm^2, a sharp emission line at $\lambda = 555.3$ nm appears, and the determined width of this emission line is $\Delta\lambda = 0.14$ nm, limited by the resolution of my spectrometer (**Figure 5.7.1b**). The narrow spectrum of the laser emission is clearly different from the ASE spectrum, which is peaked at 550.7 nm and is significantly broader (spectral width: 2.5 nm) (**Figure 5.6.4.3**).

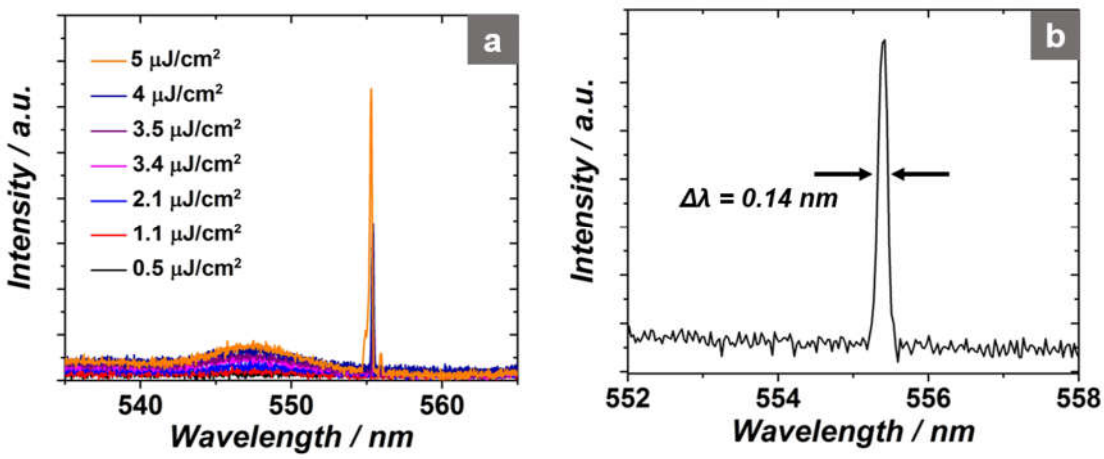

Figure 5.7.1. *a) Emission spectra upon optical pumping with increasing energy density: 0.5–5 μJ cm^{-2}. b) Emission spectrum of the laser measured with high spectral resolution.*

In agreement with the collapse of the width of the emission spectrum, the output power shows an abrupt increase for excitation levels above the threshold which is the characteristic behaviour for the transition from spontaneous emission to lasing (**Figure 5.7.2**).

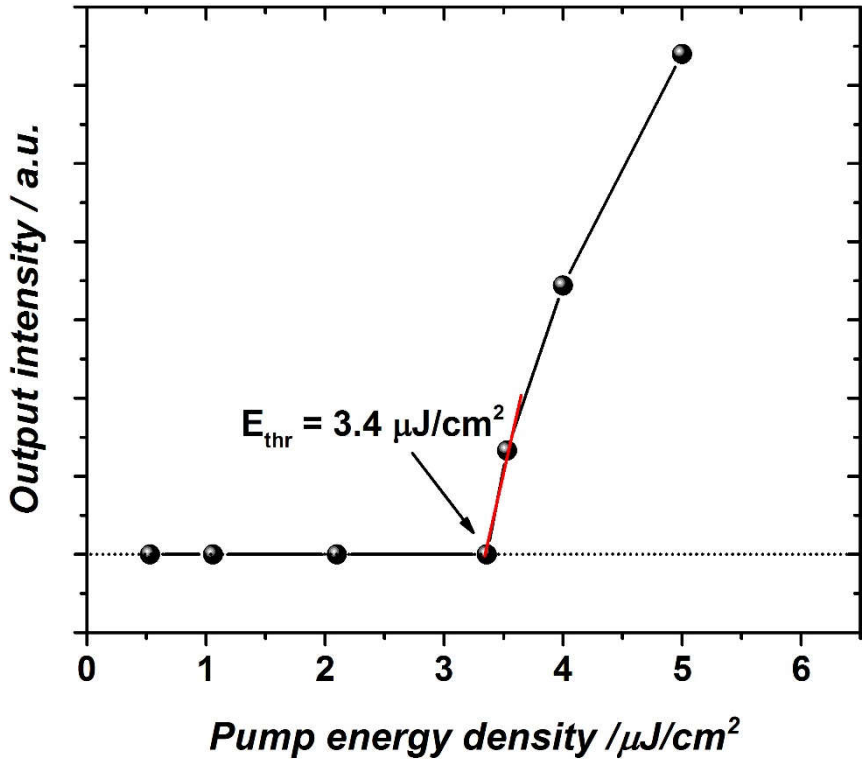

Figure 5.7.2. *Output power versus excitation energy density demonstrating a clear threshold. behaviour.*

As shown in **Figure 5.7.3**, the wavelength of laser emission can be tuned between 543.3 and 557.4 nm due to variation of the effective refractive index which is resulting from thickness inhomogeneity of the spin-coating process used for deposition of the pristine $MAPbBr_3$ thin film. The change of n_{eff} with varying the layer thickness has been already discussed (**Figure 5.4.1**). An increase of n_{eff} with increasing the thickness of the $MAPbBr_3$ waveguide layer directly infers a redshift of the lasing wavelength.

The corresponding far-field characteristics above threshold are also shown in **Figure 5.7.4a**, featuring a highly astigmatic dual-lobed pattern, which is typical for the emission of complex coupled DFB lasers based on linear grating resonators with strong diffractive out-coupling [143]. The corresponding schematic of the DFB laser is shown in **Figure 5.7.4b**. Note, the two lobes in the far-field arise as a Fourier transform of the near-field characteristics of the dominating antisymmetric resonator mode, as discussed in detail by

Noll et al [144]. If desired, a single-lobed emission could be achieved by introducing a phase shift of π.

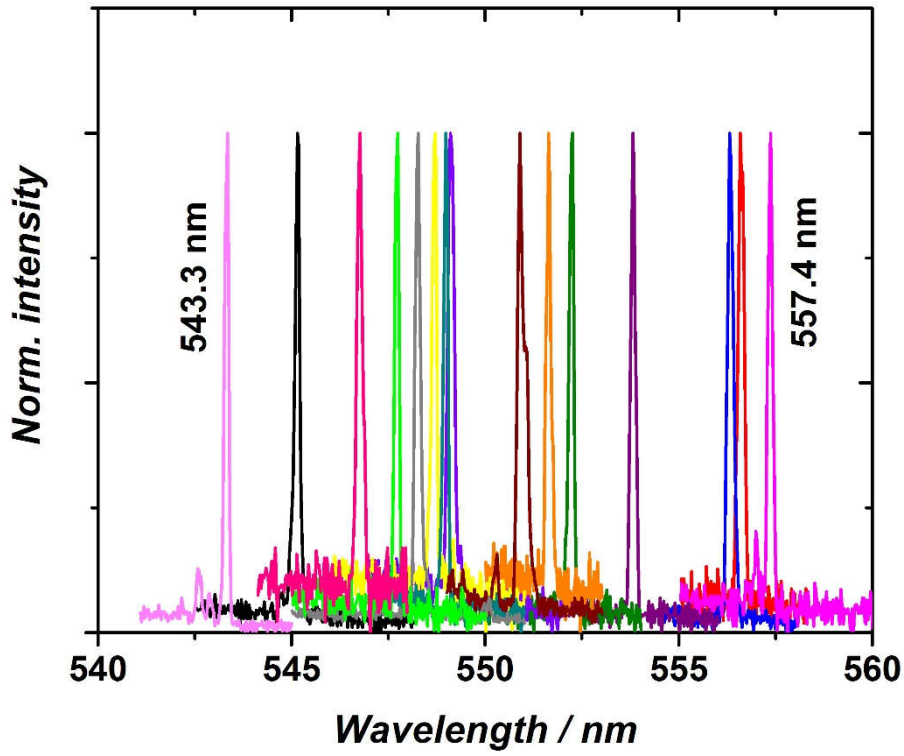

Figure 5.7.3. *Tunability of the DFB laser wavelength as I vary the position of the excitation spot on the sample. Here, local variations of the layer thickness infer a variation of the effective refractive index n_{eff} (cf. Figure 5.4.1).*

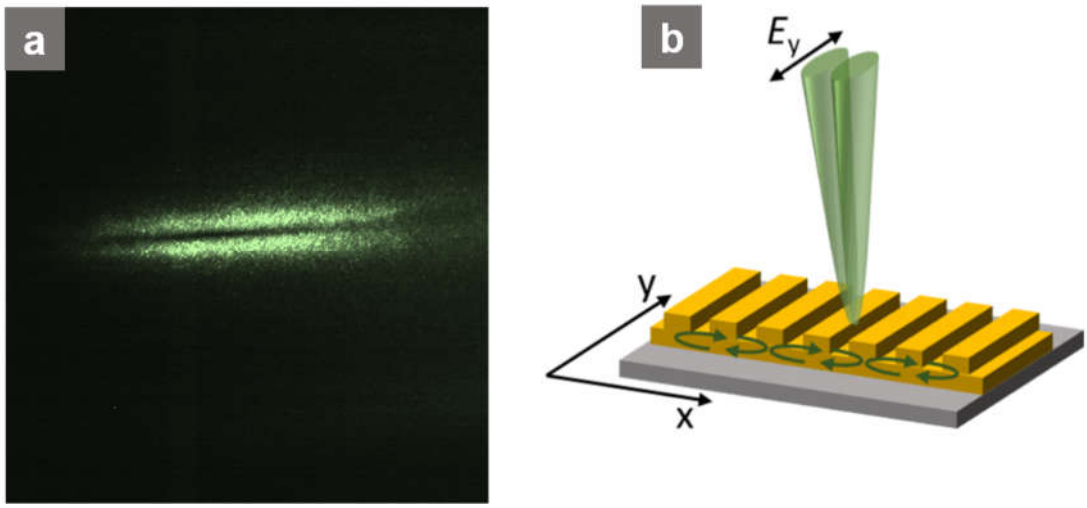

Figure 5.7.4. *a) The dual-lobed far field emission pattern above threshold. b) Schematic of the DFB laser with assignment of directions and a sketch of the laser emission as a result of first order diffraction normal to the sample surface.*

Aside from the characteristic far-field pattern, the laser emission shows a pronounced linear polarization (**Figure 5.7.5**), with the electrical field-vector parallel to the DFB grating (y-direction), indicated in **Figure 5.7.4b**.

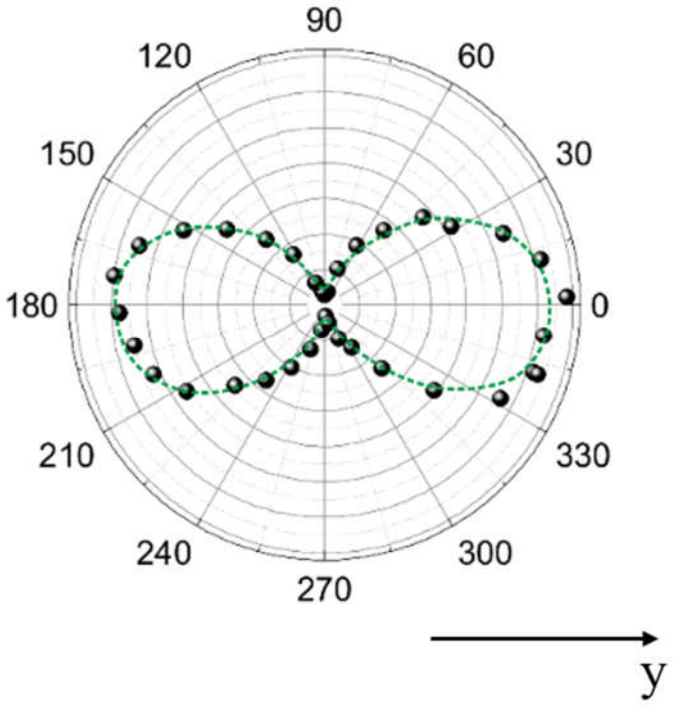

Figure 5.7.5. *Polarization characteristics of the laser emission.*

5.8. Summary

In this chapter, the first $MAPbBr_3$ thin-film DFB lasers with thermally imprinted linear gratings were realized. The imprinted resonator structures provided high quality resonators. As notable effect of the imprinting process, aside from the pattering, I achieve a substantial flattening of an initially very rough polycrystalline layer to a layer with large crystals on the order of tens of microns with a surface roughness of 0.6 nm. Therefore, a significantly lowered threshold for the onset of amplified spontaneous emission results from the reduced scattering. Regarding smoothening of the perovskite surface and a remarkable increase of grain size, in fabricated optically pumped DFB laser structures,

very low lasing thresholds of 3.4 $\mu J/cm^2$ are achieved. These low lasing threshold levels are essential on the way to the first electrically operated perovskite laser diode.

Chapter 6

Caesium-based Perovskite DFB and Vertical Cavity Surface Emitting Lasers

6.1. Introduction

ASE and optically pumped lasing has been reported for organometal halide perovskite such as $MAPbI_3$, and other hybrid organic-inorganic lead halide perovskites [4-8, 76, 9, 10, 119]. As discussed in **Chapters 4** and **5**, due to the soft nature of this class of materials, photonic resonator structures can be directly patterned into $MAPbX_3$ (X=Br, I) by thermal NIL to achieve low-threshold optically pumped perovskite lasers [145, 146]. However, as MA is volatile, MA-based organic-inorganic halide perovskites lack intrinsic stability, which substantially compromises their serious application [52, 56-60, 120, 121]. To improve thermodynamic stability, the volatile organic moiety can be replaced with inorganic cations, such as Cs [63-66]. The corresponding all-inorganic family of perovskite semiconductors, i.e. caesium lead halide, has been identified as particularly promising for light emitting applications [147].

However, early attempts to use thin-films of $CsPbX_3$ for light emission only led to disappointing results with a very low photoluminescence quantum yields (PLQY) of about 16 % [37]. More detrimentally, ASE in $CsPbX_3$ thin-films has only been achieved at

cryogenic temperatures below 150 K [148]. The poor performance at higher temperatures has been attributed to non-radiative recombination associated with the high number of defects. It must be noted that the $CsPbBr_3$ thin films used in the above studies showed poor film formation and contained a high number of pinholes. Some attempts to improve film formation and to mitigate the impact of defects were based on blending the perovskite with additives, such as ZnO nanoparticles [149] or thiocyanate ethyl acetate [150]. However, the luminescence quantum yield could not be increased beyond 20% in these reports. Two-photon pumped ASE has been reported in $CsPbBr_3$ single crystals, albeit at relatively high threshold levels (0.65 mJ cm^{-2}, 35 fs pulse width) [151].

Unlike the case of thin films, $CsPbX_3$ nanoparticles (size < 10 nm) or nanorods showed a high PLQY of more than 90% and exhibited ASE at room temperature [152-154]. Unfortunately, nanosized grains of lead-halide perovskites have been evidenced to be subject to serious stability issues [155]. Moreover, stabilizing and solubilizing capping ligands are typically required, that not only deteriorate charge transport but may likewise impede thermal transport, which is a particular problem for lasers, especially if electrical and/or continuous wave operation is considered [10, 156, 157]. Nevertheless, the impressive results achieved with $CsPbX_3$ nanoparticles nurtured the paradigm that for efficient light emission from lead halide perovskites at room temperature, one needs to confine the charge carriers/excitons on the nanometer scale to prevent their migration to non-radiative defects [20, 158].

Here, I present results that challenge this paradigm. I demonstrate thin films of caesium lead bromide, which show a high PLQY of 68 % and a low threshold ASE at room temperature. The continuous films (~ 100% coverage of the substrate) are composed of large crystals with a lateral extension on the order of micrometers. My layers result from originally rough as-deposited layers that were recrystallized by thermal imprint. Using these layers, I demonstrate the first caesium lead bromide thin film DFB and vertical cavity surface emitting lasers (VCSELs) with ultralow threshold at room temperature, that do not rely on the use of nanoparticles. My results render this all-inorganic gain medium an excellent material platform for perovskite laser diodes in the future.

Note, this chapter is based on my previously published journal article **"Room Temperature Stimulated Emission and Lasing in Recrystallized Cesium Lead Bromide Perovskite Thin Films", Adv. Mater., 2019, 31, 1903717.**

6.2. Pristine caesium lead bromide layer deposition

The caesium lead bromide thin films used in this study are prepared from a solution of caesium bromide (CsBr) and lead bromide ($PbBr_2$) in anhydrous dimethylsulfoxide (DMSO). The molar ratio of CsBr:$PbBr_2$ is varied between 0.5:1 and 3:1. Initially, a ratio of 1:1 is chosen.

Before demonstrating laser characteristics, planar hot pressing, defined in **Section 5.6**, is applied to pristine caesium lead bromide thin films to study the impact of temperature and pressure on morphological, compositional, and optoelectronic properties of these layers over imprinting.

6.3. Planar hot pressing process

The as-deposited layers are recrystallized by a thermal imprint process at 150 °C and a pressure of 100 bar, using a flat piece of silicon wafer as stamp (**Figure 6.3.1**). More details about the film deposition and the thermal imprint process can be found in the **Appendix A/Experimental data**.

The effect of PHP on perovskite morphology

As illustrated in **Figure 6.3.2a**, spin-coated caesium lead bromide thin films are very rough (roughness 23.8 nm, rms), with a significant number of pinhole defects (which is typical for caesium lead bromide thin films). In contrast, after recrystallization by a PHP process, the perovskite layers get strikingly flattened, and thus roughness goes down to 0.5 nm, rms. As can be seen in **Figure 6.3.2b**, pressed layers consist of large crystals with

micron-sized lateral dimensions despite pristine layers which are composed of nanometer-sized crystallites.

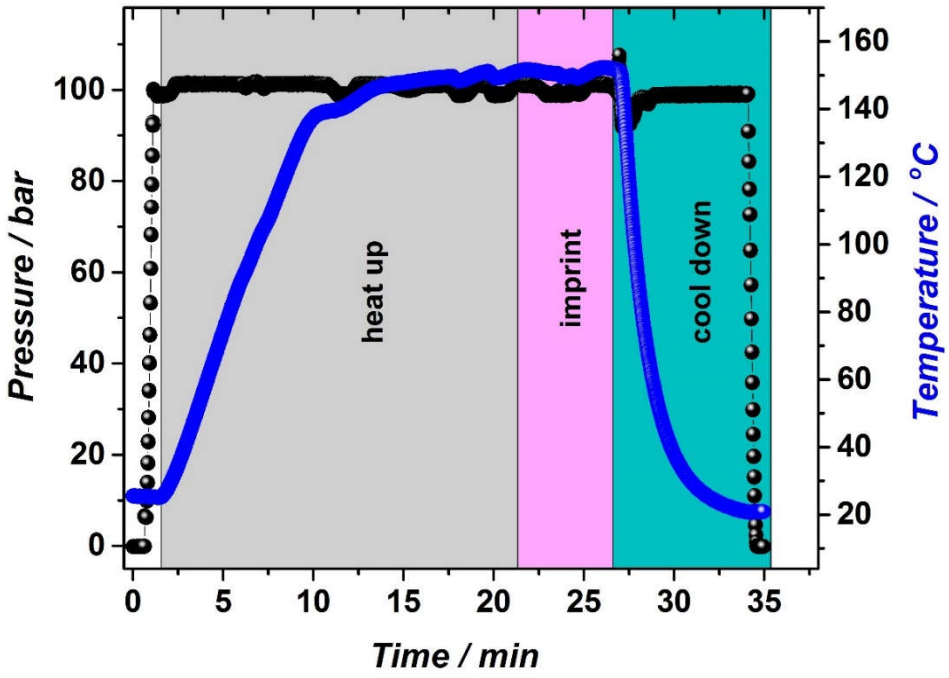

Figure 6.3.1. *Applied temperature and pressure of planar hot pressing.*

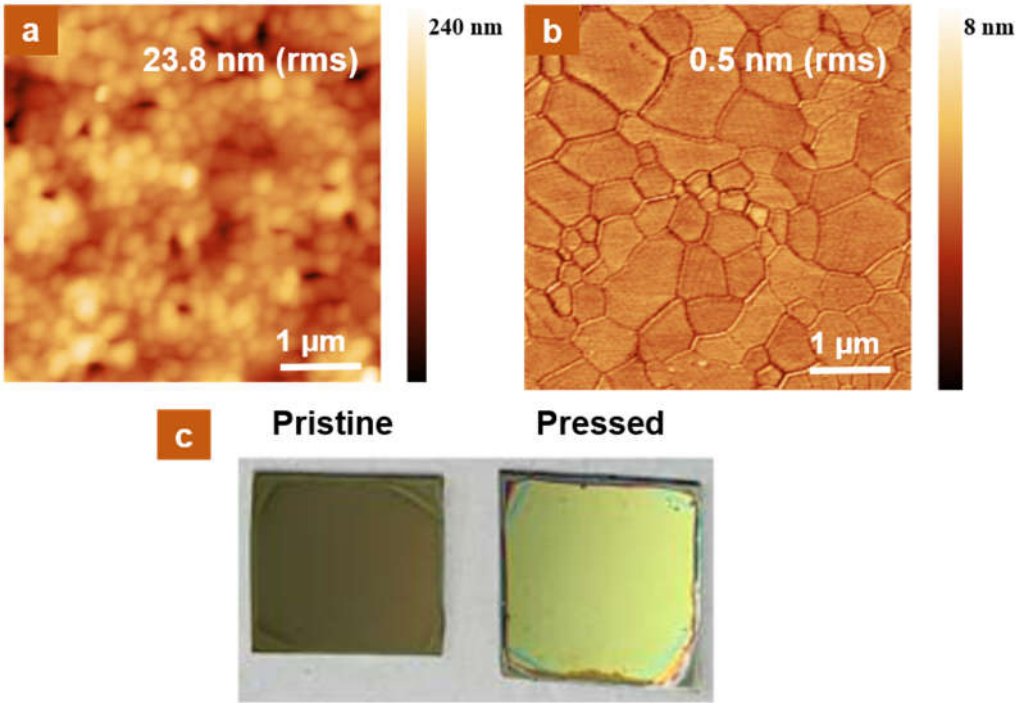

Figure 6.3.2. *AFM images of caesium lead bromide layers (molar ratio of CsBr:$PbBr_2$ is 1:1) a) before and b) after PHP process. c) Photograph of pristine and pressed layers on Silicon substrate.*

To further illustrate the smoothening of spin-coated perovskite layers after PHP process, the photographs of pristine and pressed layers (on silicon substrate) are shown in **Figure 6.3.2.c.** The photographs clearly demonstrate the mirror-like surface of the pressed layers as opposed to the dull impression of the rough pristine layer, evidencing flattening of layers after pressing.

X-ray diffraction (XRD) analysis

To better characterise the impact of the PHP process on the structrul properties of caesium lead bromide layers, X-ray diffractograms for pristine and pressed layers are measured **(Figure 6.3.3a, b**).

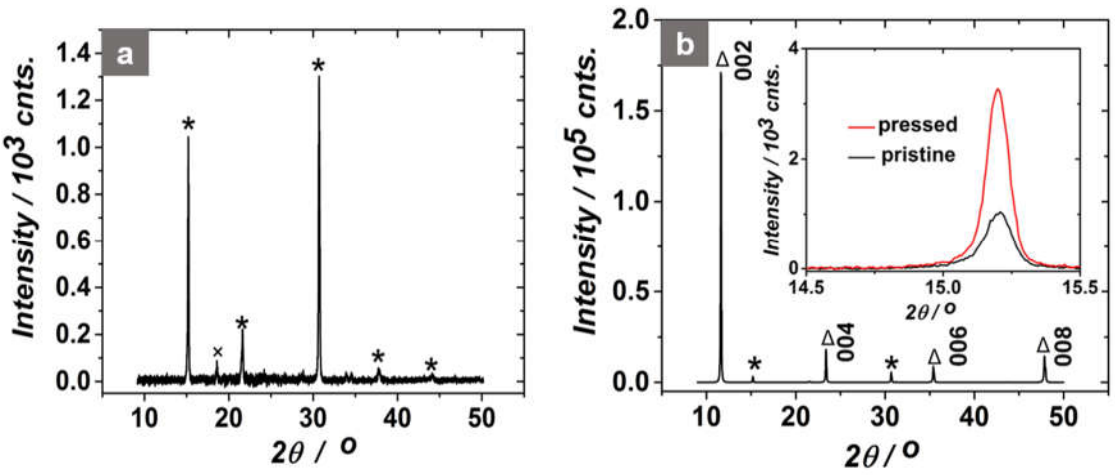

Figure 6.3.3. *X-ray diffractograms of a) pristine and b) pressed films. The symbols mark diffraction peaks due to $CsPbBr_3$ (*), $CsPb_2Br_5$ (Δ) and $PbBr_2$ (×). Note, the y-axis in (b) spans a two orders of magnitude larger scale than that of (a). The inset compares the 110 diffraction peaks of the orthorhombic $CsPbBr_3$ in the pristine and pressed layer.*

The pristine sample exclusively shows reflections attributed to the orthorhombic $CsPbBr_3$ phase (ICSD 97851), with a minor peak at 18.62°, which could be due to $PbBr_2$. In striking contrast, the pressed and recrystallized film shows two orders of magnitude more intense peaks, that can be assigned to the tetragonal 2D phase $CsPb_2Br_5$ (i4mcm, JCPDS No. 025-0211, **Figure 6.3.3b**). The dominance of the 002, 004, 006, 008 peaks indicates

the high degree of orientation of the crystals, which is also evidenced by Electron backscatter diffraction (EBSD) (**Figure 6.3.4**). However, it has to be noted that in the pressed layers the reflections due to the 3D $CsPbBr_3$ phase have also gained by a factor of three in intensity compared to the pristine layer (see inset **Figure 6.3.3b**). As such, XRD provides evidence of substantial recrystallization and an overall improved crystal quality upon thermal imprint.

Scanning electron microscopy (SEM), and electron backscatter diffraction (EBSD)

To elucidate the presence of the 2D and 3D phases in my pressed layers, SEM and EBSD (**Figure 6.3.4a, b**) are performed.

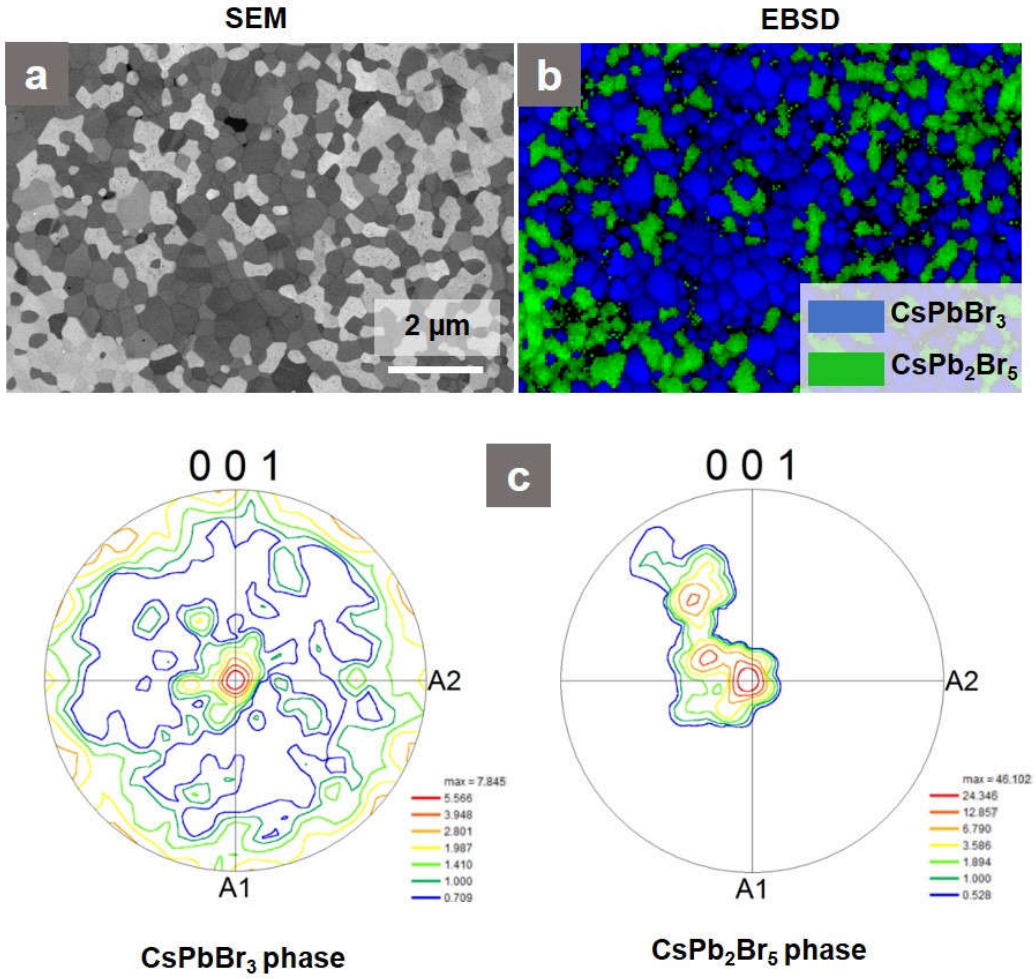

Figure 6.3.4. *a) SEM image obtained with backscattered electrons, and b) EBSD of a pressed/recrystallized layer. c) Pole figures of the two relevant phases, with the compression direction in the center of the pole figure. The directions A1 and A2 are randomly selected.*

Interestingly, the SEM image obtained with backscattered electrons shows a very pronounced contrast of bright and dark crystals, which cannot be explained by topography effects. The higher lead content in the 2D phase is expected to cause stronger scattering of electrons which accounts for the higher brightness in the backscattered SEM image. According to a quantitative analysis of the SEM images using an image processing software, I can determine the relative content of $CsPb_2Br_5$ to be 46% in these samples.

Moreover, EBSD (performed by **Dr. Stefan Zaefferer, Max-Planck-Institut für Eisenforschung**) reveals that the crystals that appear dark in SEM are $CsPbBr_3$ (3D) while those appearing bright are $CsPb_2Br_5$ (2D). The EBSD patterns are of sufficient quality to be crystallographically analysed. A number of crystallographic phases are used for pattern indexing: the cubic $CsPbBr_3$, ICSD-ID 29073, space group 221 with lattice constants 0.5874 nm, the orthorhombic $CsPbBr_3$, ICSD-ID 97851, space group 62, lattice constants a = 0.8207 nm, b = 0.8255 nm and c = 1.1759 nm, and the tetragonal $CsPb_2Br_5$, space group 140, lattice constants a = 0.846 nm and c = 1.595 nm.

Pattern indexing results in two fractions of grains. One fraction is indexed with the tetragonal phase $CsPb_2Br_5$. These grains correspond to the bright grains in **Figure 6.3.4a**. The other fraction can be indexed with the orthorhombic as well as with the cubic phase $CsPbBr_3$. Nevertheless, the cubic phase fits significantly better: not only the angular deviation between experimental and theoretical re-calculated pattern is smaller for the cubic phase but also a unique crystal orientation is obtained per grain with this phase while the orthorhombic phase results, for many grains, in several, pseudosymmetric, solutions. The pattern quality is, unfortunately, too low to decide with certainty whether the cubic or the orthorhombic phase is the actual phase. The cubic phase generally fits better but the additional XRD data suggest that the orthorhombic is the correct phase.

Both, cubic and orthorhombic structures result in sharp textures with a (001) plane normal pointing in the compression direction (CD). The orientation distribution function (i.e. the texture) is calculated by harmonic series expansion up to a series expansion rank 32. The resulting (001) pole figure (here for the cubic phase) is shown in **Figure 6.3.4c** (left). The tetragonal phase shows a very strong (001) || CD fiber texture which is displayed in **Figure 6.3.4c** (right).

Photoluminescence microscopy

The co-existence of the 3D and 2D phase is further evidenced in optical transmission/PL microscopy (**Figure 6.3.5**), which has been measured by **Tobias Haeger**.

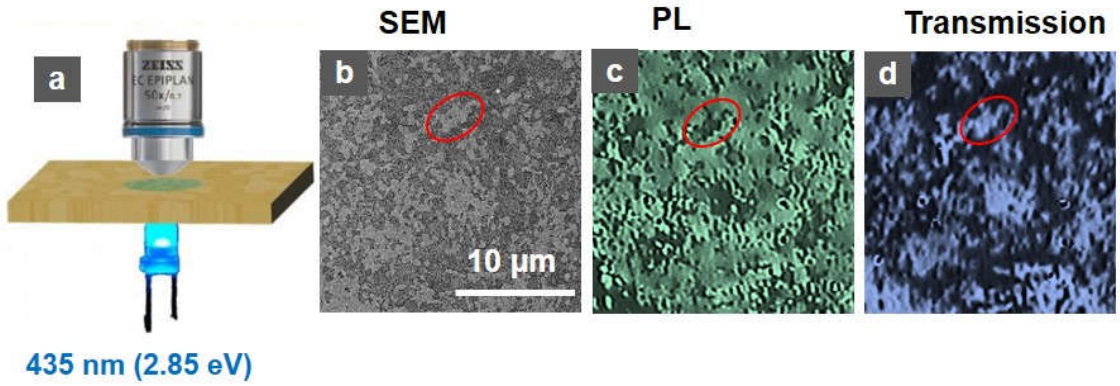

Figure 6.3.5. *a) Schematic of the transmission/emission microscopy using a conventional optical microscope with bottom illumination by a LED emitting at 435 nm (2.85 eV). The PL image has been obtained by blocking the transmitted LED light with a 500 nm long-pass optical filter. b) SEM image of the field of view. For registration purposes a characteristic position is marked with a red ellipse. c) PL image and d) transmission.*

The PL microscopy shows that the light emission results exclusively from the regions that have been identified by EBSD as 3D ($CsPbBr_3$), i.e. the darker regions in the SEM image. On the contrary, the 2D regions are non-emissive. This is in contrast to earlier reports that claimed that the formation of $CsPb_2Br_5$ inferred a substantial improvement in PLQY [159]. This finding is complemented by the transmission image (**Figure 6.3.5d**), where the 2D regions are transparent for the LED light (2.85 eV, 435 nm) due to their large indirect bandgap of 3 eV. Note, the 2D regions remain non-emissive even if I use a different LED with a higher photon energy of 3.3 eV (375 nm), which is then absorbed by the 2D regions (as verified by transmission microscopy, not shown here). Note, thermal microscopy has shown a similar contrast associated with the 2D and 3D phase in thermal conductivity [160].

Absorption analysis

The resulting layers are also analysed through photo-thermal deflection by **David Becker-Koch, Kirchhoff-Institut für Physik Ruprecht-Karls-Universität Heidelberg** (**Figure 6.3.6**). The energy gap derived from the absorption spectra is E_g = 2.32 eV (534 nm) for both the pristine and the pressed layer, corresponding to the direct band gap of $CsPbBr_3$. For $CsPb_2Br_5$, an indirect bandgap of 3 eV or larger has been reported [161, 162].

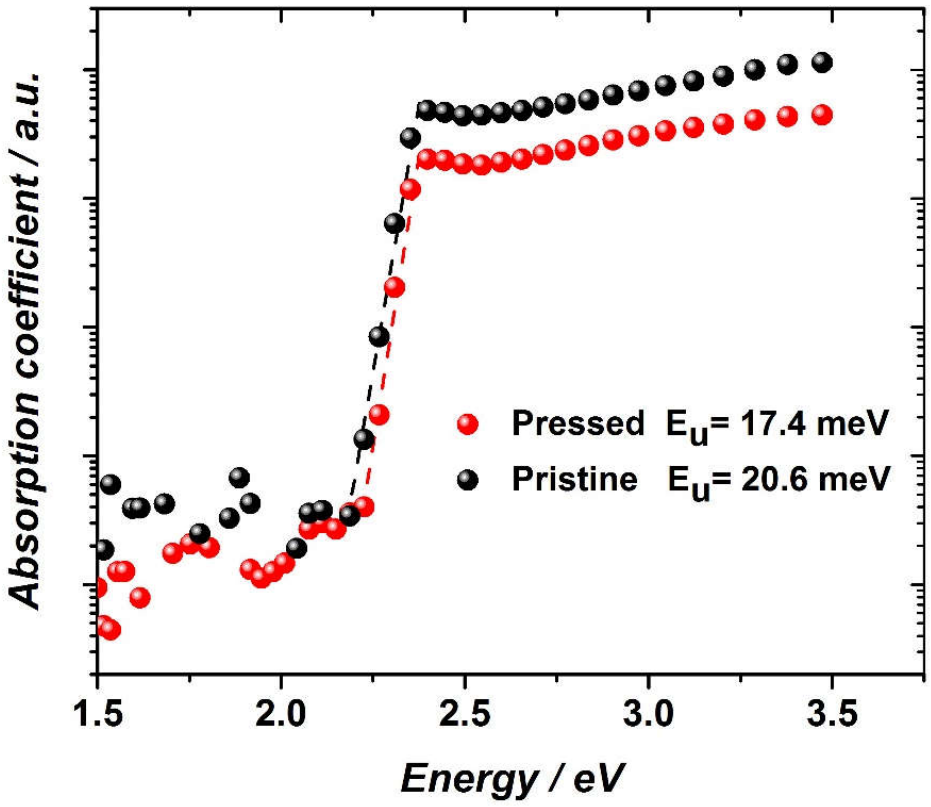

Figure 6.3.6. *Absorption spectra resulting from photo-thermal deflection spectroscopy (PDS).*

The Urbach energy of the recrystallized layer is 17.4 meV, similar to what has been reported for high-quality $CsPbBr_3$ single crystals [163] and substantially lower than that of the pristine film (20.6 meV), suggesting a lower degree of energetic disorder within the recrystallized films and agrees with the narrowed PL-linewidth (**Figure 6.3.7**).

Photoluminescence characterisation

The PL spectra for pristine and pressed layers are also shown in **Figure 6.3.7** Most notably, the spectral width (full-width half-maximum) is substantially reduced from $\Delta\lambda$ = 20.1 nm ($\Delta(h\nu)$ = 91 meV) for the pristine layer to 14.5 nm (66 meV) for the pressed layer. Note, while the short-wavelength edge of the PL spectra is very similar, the high-wavelength edge is significantly red-shifted in the pristine layers, which indicates recombination via near-band-edge defects. As such, the narrowed PL linewidth supports the conclusion of an overall improved material quality in the pressed layers and agrees with the lowered Urbach energy in **Figure 6.3.6.**

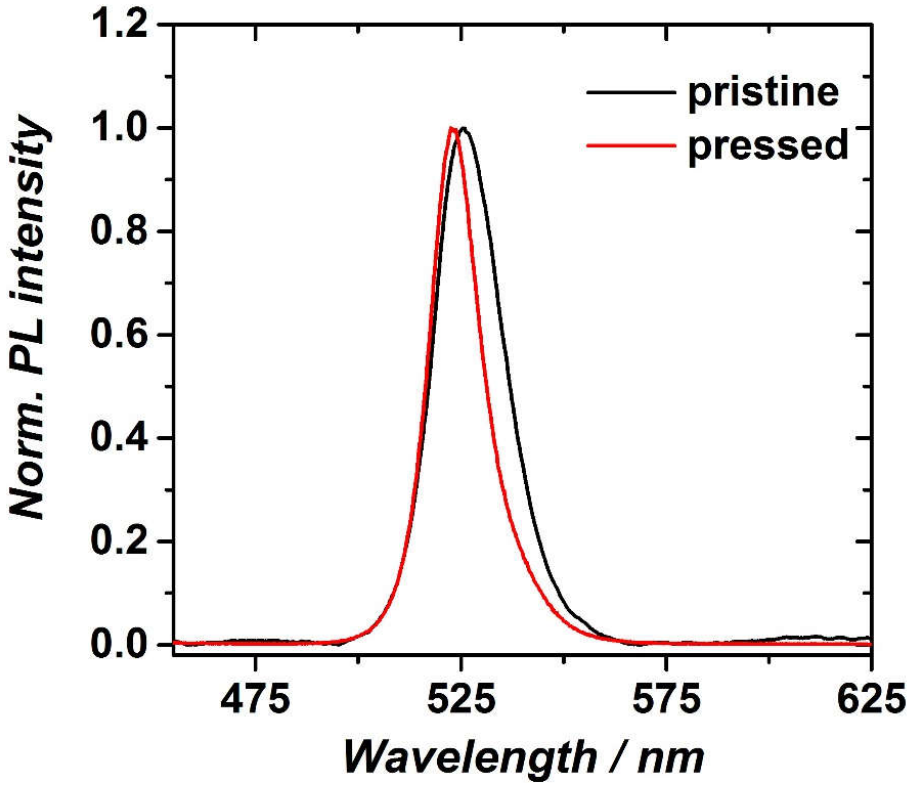

Figure 6.3.7. *PL spectra of pristine and pressed layers at room temperature.*

Time-resolved Photoluminescence investigation

The time-resolved analysis of the PL decay dynamics, measured by **Marko Cehovski, and Ouacef Charfi, Institut für Hochfrequenztechnik Technische Universität Braunschweig**, is shown in **Figure 6.3.8.** The data is fitted by a bi-exponential decay.

For the pristine sample, decay times of τ_1 = 4.1 ns and τ_2 = 10 ns are determined. In the recrystallized layers a notable increase of τ_1 = 5.9 ns and τ_2 = 19 ns is found, which are similar to decay times reported for $CsPbBr_3$ single crystals [163-165], which is another indication of improved material quality after PHP process.

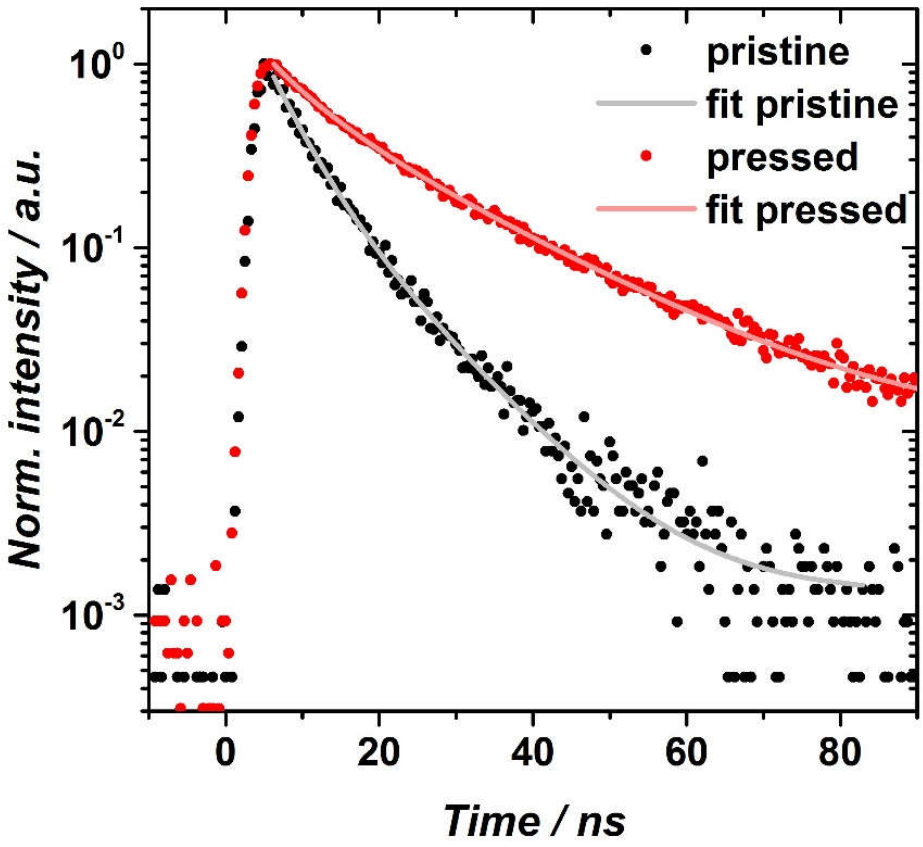

Figure 6.3.8. *Time resolved PL decay for pristine and pressed layers at room temperature.*

External photoluminescence quantum yield (η_{ext})

The external PLQY (η_{ext}) of pristine thin films at room temperature is about 9.3%. This η_{ext} can be translated to an internal PLQY (η_{int}) of about 43% (regarding **Equation 2.2.5.1**, more details can be found in **Section 6.4**). Notably, η_{int} of the recrystallized films increased to 53% proving the quality improvement of $CsPbBr_3$ layers after PHP.

Amplified spontaneous emission (ASE)

Taken together, the optical analysis revealed an improved PLQY, increased PL lifetime, and lowered Urbach energy in the recrystallized layers. All observations point to an effective mitigation of non-radiative recombination in the recrystallized samples, being the key for achieving ASE at room temperature.

While I am not able to achieve ASE from the pristine thin films at room temperature, even under pulsed excitation at levels of 600 μJ/cm^2 (λ = 355 nm, pulse duration ~ 300 ps), which already marks the onset at which the focused laser beam starts to machine the perovskite thin film, the recrystallized films show ASE at room temperature (λ_{ASE} = 541 nm, spectral width~ 2.5 nm) under pulsed excitation with a low threshold of 12.5 μJ/cm^2 (**Figure 6.3.9**).

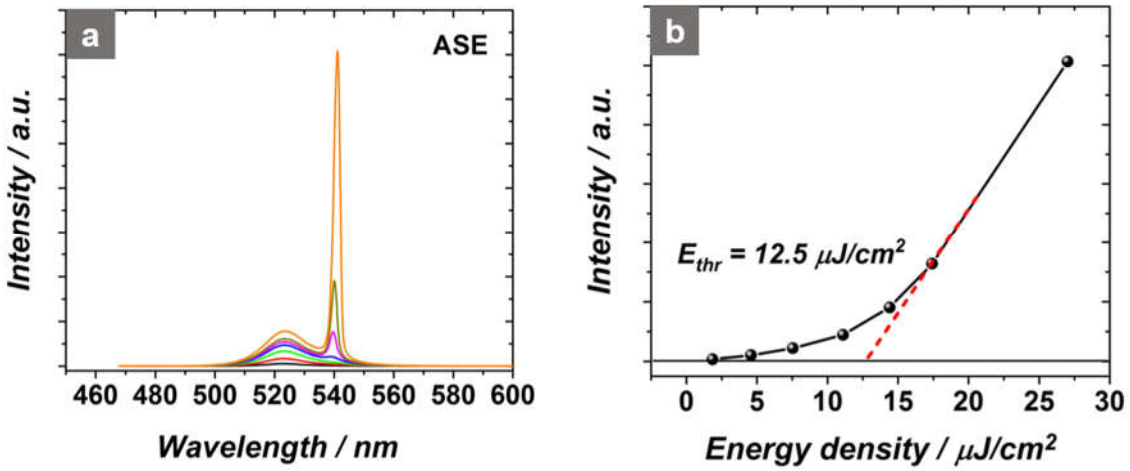

Figure 6.3.9. *Amplified spontaneous emission measurement on a flattened caesium lead bromide thin-film as shown in Figure 6.3.2b. a) Emission spectra and b) corresponding output characteristics.*

Terahertz (THz) absorption spectroscopy

Furthermore, terahertz (THz) absorption spectroscopy (measured by **Markus Stein, Fachbereich Physik Philipps-Universität Marburg**) is studied (**Figure 6.3.10**). THz absorption spectroscopy conducted at room temperature revealed sharp absorption

peaks in the recrystallized layers at 1.025 THz (34 cm^{-1}), 1.428 THz (47.6 cm^{-1}) and 1.965 THz (65.5 cm^{-1}), whereas the spectrum for the pristine layer only shows less-pronounced features at similar positions. These results are indicative of a substantially reduced number of structural defects in the recrystallized layers [166]. The peak positions agree with the energy of lattice vibrations, reported for single crystals of $CsPbBr_3$ and $CsPb_2Br_5$ [167, 168].

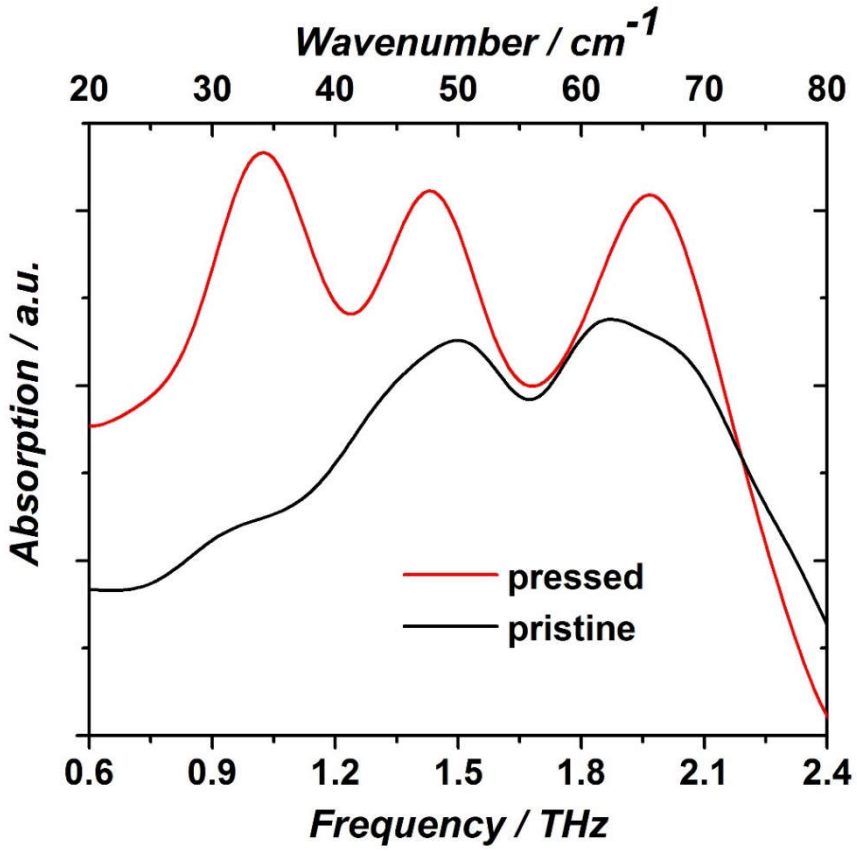

Figure 6.3.10. *Absorption spectra resulting from terahertz absorption spectroscopy of pristine and flattened layers.*

6.4. Impact of 2D caesium lead bromide ($CsPb_2Br_5$) on light emission

To identify whether and to what extent the presence of the non-emissive 2D phase is beneficial for the light emission of the film, i.e. to passivate defects, I aim to reduce the formation of $CsPb_2Br_5$. As formation of $CsPb_2Br_5$ after hot planar pressing is due to the deficiency of the CsBr content in the pristine thin films, in order to reduce its formation,

I need to increase the concentration of CsBr in the precursor solution. Unfortunately, the solubility of CsBr in DMSO is limited and precipitates are forming upon increasing the molar content of CsBr.

Rutherford backscattering spectrometry (RBS), measured by **Dr. Detlef Rogalla, RUBION Ruhr-University Bochum**, shows that precursor solutions with a nominal molar ratio of CsBr:$PbBr_2$ ranging from 0.5:1 to 3:1 afford pristine layers with a substantially lower relative Cs content (**Figure 6.4.1**). For example, for CsBr:$PbBr_2$ = 1:1 in the precursor, I find [Pb]/[Cs] = 1.4 and [Br]/[Pb] = 2.7 in the film.

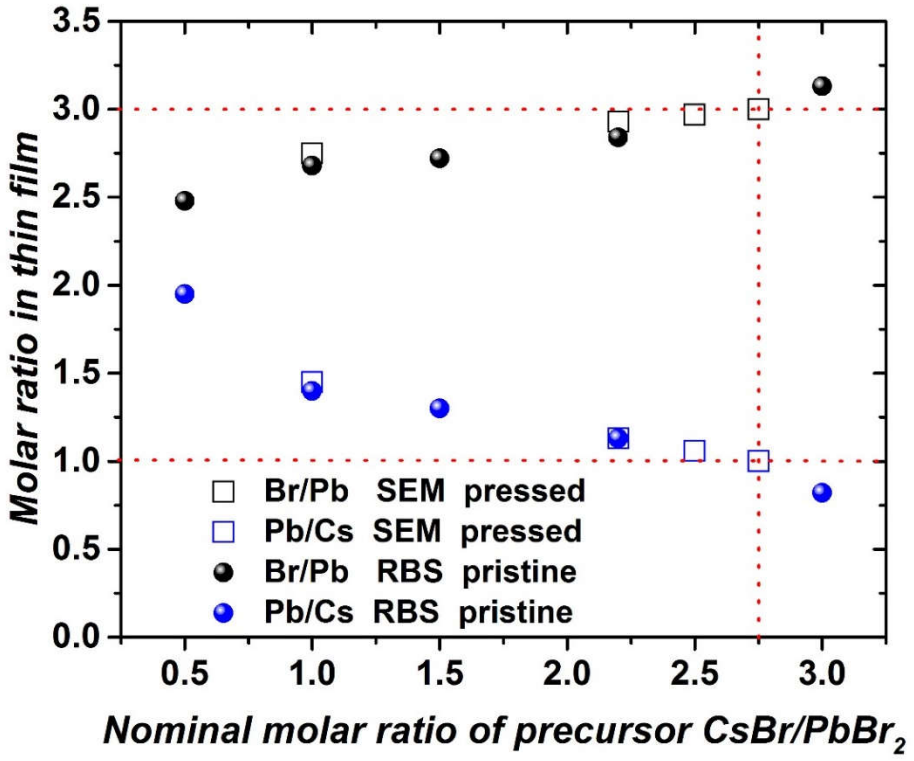

Figure 6.4.1. *Molar ratio Pb/Cs and Br/Pb in the pristine and pressed films vs. nominal molar ratio ($CsBr/PbBr_2$) of the precursor. The ratio in the film has been determined by RBS and SEM (see text), respectively.*

Overall, the [Pb]/[Cs] and [Br]/[Pb] ratio determined by RBS is in favorable agreement with the relative abundance of $CsPb_2Br_5$ and $CsPbBr_3$ identified by the bright (2D) and dark (3D) regions in the SEM images, respectively (**Figure 6.4.2**). Most notably, a ratio

of [Pb]/[Cs] = 1 and [Br]/[Pb] = 3 in the film is found for a nominal ratio of $CsBr:PbBr_2$ = 2.75:1 in the precursor. As can be seen in **Figure 6.4..2c**, there is no indication of bright/dark contrast in the SEM image taken from the 2.75:1 sample as in the mixed phase samples.

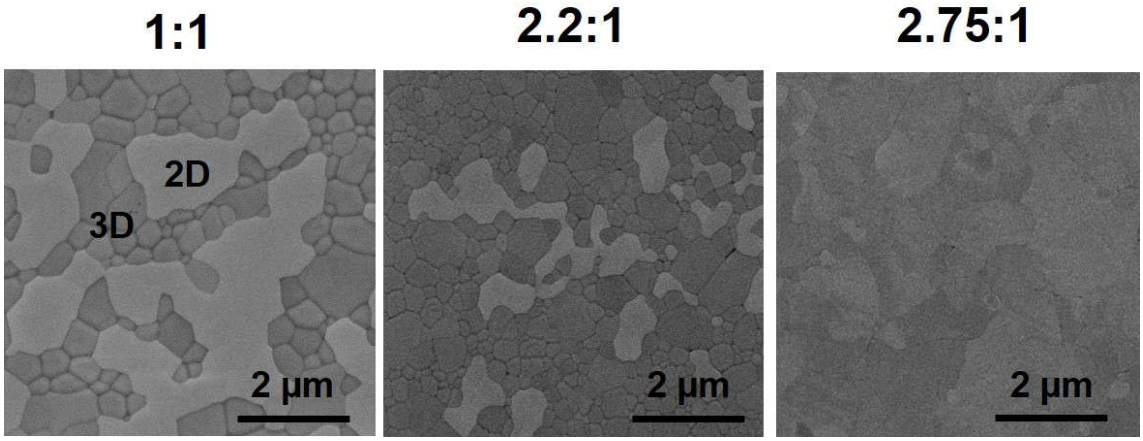

Figure 6.4.2. *SEM images of flattened layers prepared from a nominal precursor ratio ($CsBr:PbBr_2$) in the solution of a)1:1 b) 2.2:1 and c) 2.75:1. The 2D phase appears brighter than the 3D phase in the SEM images of the 1:1 and 2.2:1 ratios, as verified by EBSD (main text), but there is no indication of bright/dark contrast in the SEM image of the 2.75:1 ratio. Note, in this set of experiments, secondary electrons were detected and even in this case a notable material contrast between 2D and 3D phase is found, albeit somewhat less than that in case of backscattered electrons.*

XRD measurements further illustrate the gradual reduction of the abundance of the 2D phase relative to that of the 3D phase in the pressed layers prepared with a $CsBr:PbBr_2$ ratio increased from 1:1 to 2.6:1 (**Figure 6.4.3**). Finally, for CsBr:PbBr2 = 2.75:1, the signal due to the 2D phase is entirely absent and only intense reflections due to the 3D phase are found.

The external PLQY (perforemd by **Ivan Shutsko, Chair of Large Area Optoelectronics, University of Wuppertal**) is measured by using an integrating sphere. An external PLQY (η_{ext}) of 11.2% is determiined for the mixed 2D ($CsPb_2Br_5$)/3D ($CsPbBr_3$) ($CsBr:PbBr_2$=1:1) layer and 12.5% for the pure 3D ($CsPbBr_3$) ($CsBr:PbBr_2$=2.75:1) layer, respectively.

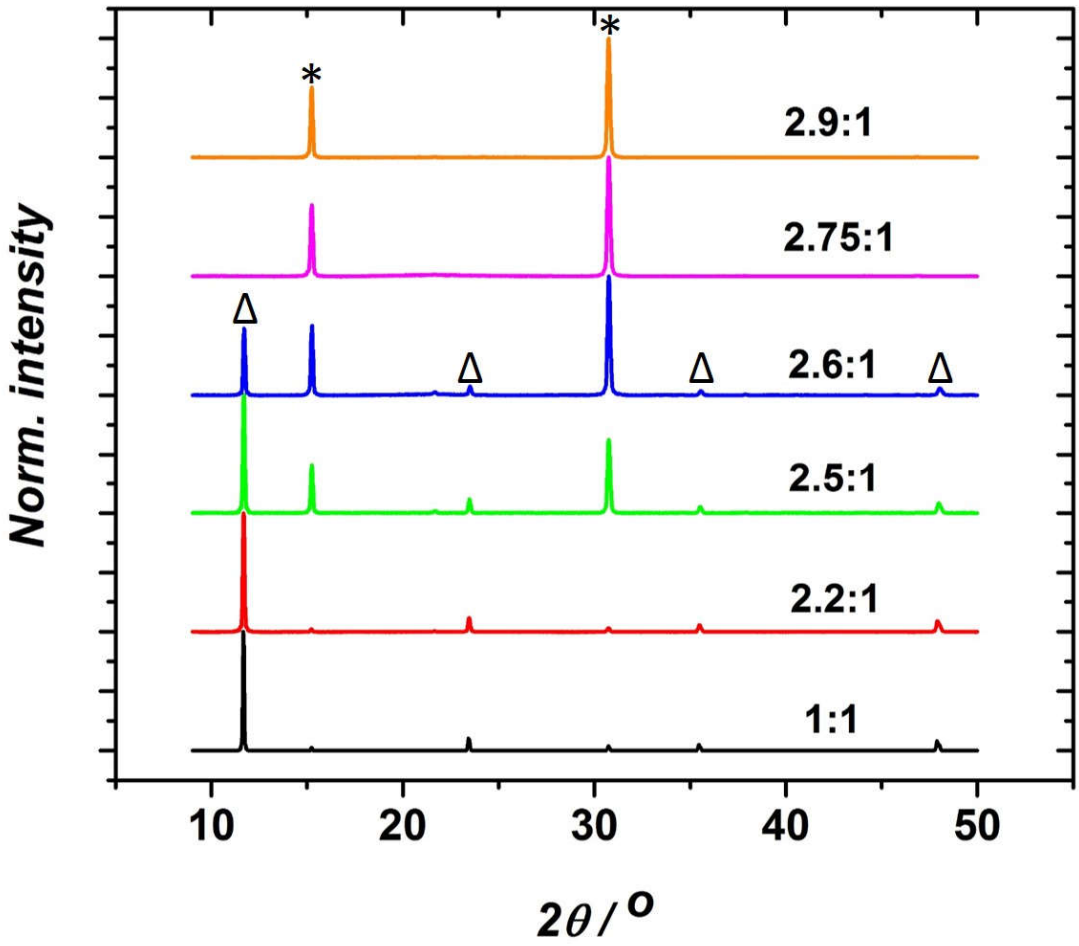

Figure 6.4.3. *X-ray diffractograms of pressed films resulting from a varied $CsBr/PbBr_2$ ratio of the precursor. The symbols mark diffraction peaks due to $CsPbBr_3$ (∗), $CsPb_2Br_5$ (Δ).*

As it was explained in **Section 2.2.5**, photon-recycling has to be taken into consideration to determine the internal PLQY (η_{int}), and regarding **Equation 2.2.5.1**, taking P_{out} for the respective layer, a relation between η_{int} and the external PLQY (η_{ext}) can be derived as follows:

$$\eta_{ext} = \eta_{int} \times P_{out}/(1 - \eta_{int} + \eta_{int} \times P_{out} + \eta_{int} \times P_{Si})$$

where P_{Si} is the portion absorbed by the Si substrate.

To determine P_{out} and P_{Si}, I initially measured the refractive index (n) and extinction coefficient (k) for my flat pressed perovskite layers using ellipsometry (**Figure 6.4.4**).

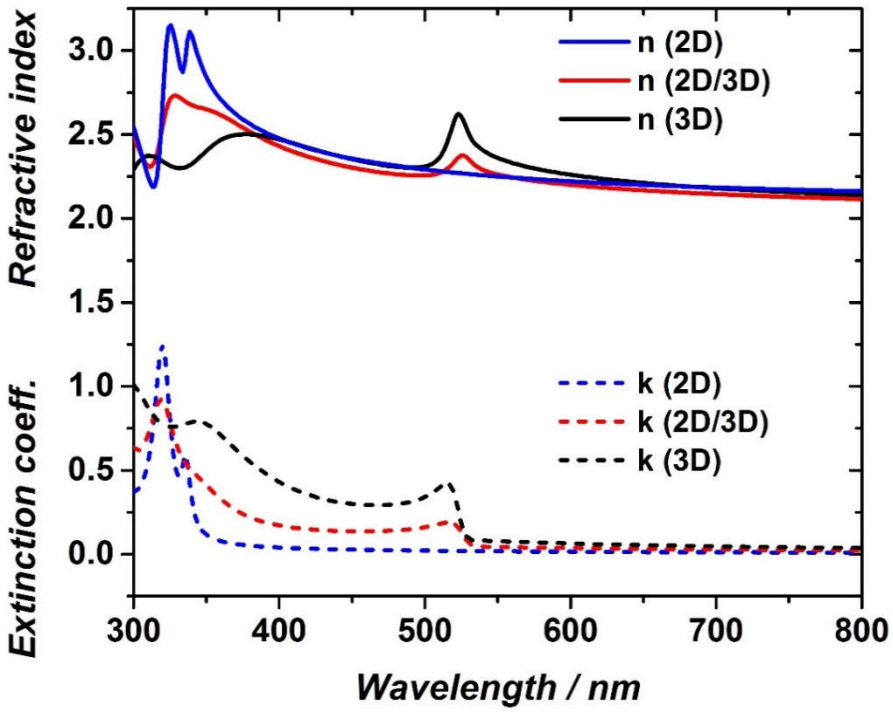

Figure 6.4.4. *Spectra of the refractive index (n) and extinction coefficient (k) for flattened layers where the 3D content is 100% and 54% (i.e. 46% 2D). For comparison, the n and k data of a 2D ($CsPb2Br_5$) layer are also shown.*

Note, to form pure 2D caesium lead bromide after planar hot pressing, the 0.5 to 1 ratio of CsBr:$PbBr_2$ is used for preparing perovskite precursor (**Figure 6.4.5**).

The samples used to assess the PLQY are Si(wafer)/SiO_2(1.5µm)/perovskite/air. This layer sequence has been used to model the outcoupling probability into the upper half sphere (2π) P_{out} (**Figure 6.4.6**). A finite difference time domain (FDTD) electromagnetic simulation method implemented in a commercially available software (Lumerical) has been used to determine P_{out} and P_{Si} (calculations were done by **Dr. Piotr Jacek Cegielski, AMO GmbH**). In these calculations, the materials are represented by their complex refractive indices.

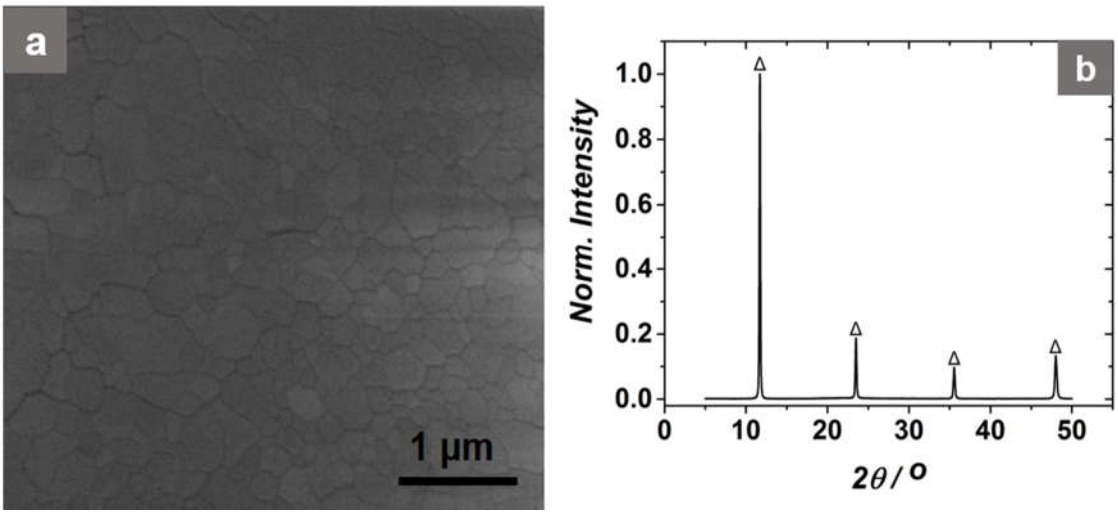

Figure 6.4.5. *a) SEM image, and b) X-ray diffractograms of flattened layer prepared from $CsBr/PbBr_2$ ratio of the 0.5:1 precursor. The symbols mark diffraction peaks due to $CsPb_2Br_5$ (Δ).*

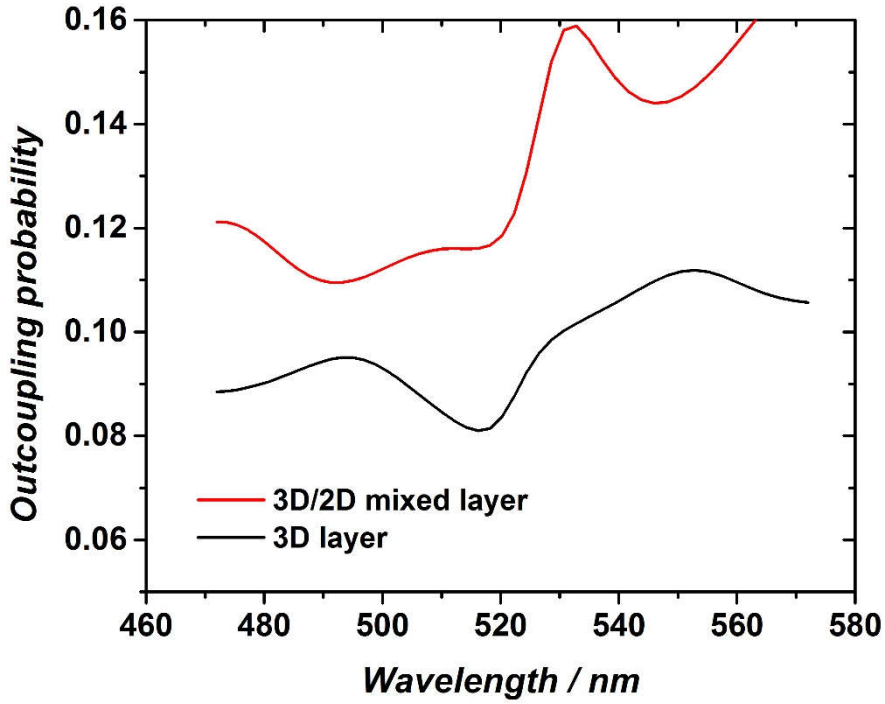

Figure6.4.6. *The n, k data are used to model the outcoupling probability for a 3D and a mixed 3D/2D layers.*

The perovskite is modeled by the corresponding experimental n, k data. In case of the mixed 2D/3D phase, the material is modelled using a mix of 2D and 3D crystal grains represented by experimental n, k data of pure 2D and 3D phases. Magnetic and electric dipoles located at positions linearly distributed across the thickness of the perovskite layer are used to represent emission of p and s polarized photons from different positions inside the film. The dipoles are set to emit a short pulse, the transmission of which through the upper half sphere is monitored giving the outcoupling probability function over a 100 nm band. Further, this data is averaged over the source position and both polarizations to account for an equal probability of emission of randomly polarized photons from various locations within the film. As expected, the large refractive index causes a relatively low P_{out} of about 13.4% for the mixed (3D/2D) layer and of 9.2% in the 3D ($CsPbBr_3$) flattened layers, respectively. Consequently, I determine a η_{int} = 53% for the mixed 2D ($CsPb_2Br_5$)/3D ($CsPbBr_3$) layer and η_{int} = 68% for the 3D ($CsPbBr_3$) layer.

To understand how the presence of the 2D phase affects the ASE threshold, I study the samples under pulsed optical excitation at elevated excitation densities. The corresponding ASE threshold is shown in **Figure 6.4.7**.

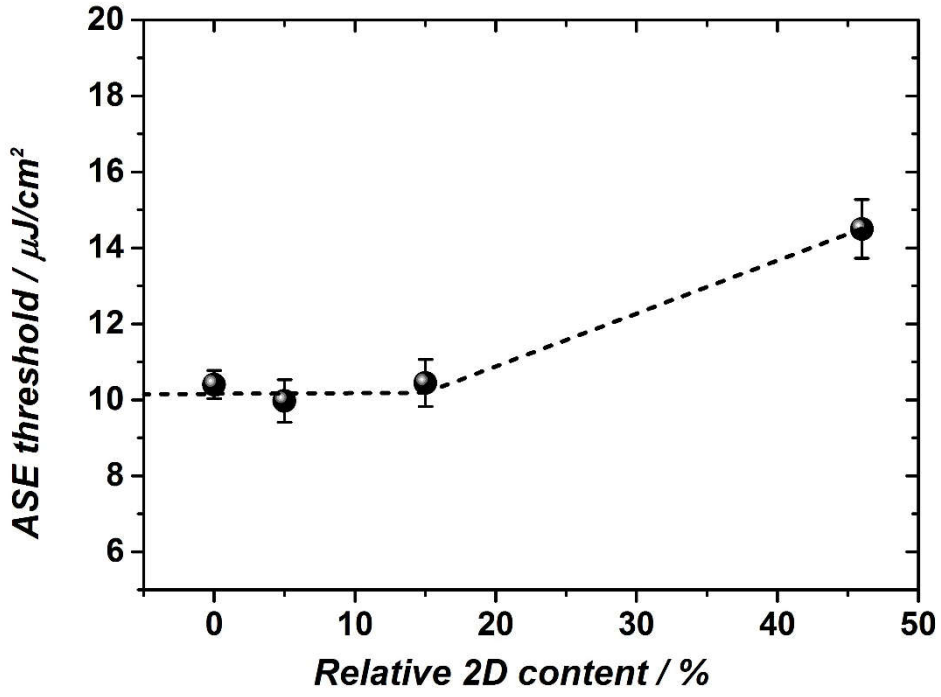

Figure 6.4.7. *ASE threshold of pressed films with varied relative content of the 2D phase ($CsPb_2Br_5$).*

Most importantly, the ASE threshold remains constant for a relative content of the 2D phase in the film below 15%. There is a slightly elevated threshold for layers with a higher 2D content of around 50%. This is in part attributed to a strongly reduced amount of active material, as the wide-gap, indirect 2D-phase does not contribute to the ASE.

Thus, the results clearly demonstrate that the improved optical properties of the layers are not inferred by the formation of 2D $CsPb_2Br_5$, but rather by the overall improved crystal quality due to recrystallization of the $CsPbBr_3$, which mitigates non-radiative recombination. A further important insight results: Efficient light emission in this class of materials is not exclusively linked to nano-crystals, but room-temperature ASE can likewise be provided by thin films, such as my high-quality recrystallized layers.

6.5. Lasing characteristics

6.5.1. Distributed feedback laser (DFB)

In the following, I utilize the outstanding optical properties of the recrystallized caesium lead bromide in laser structures. First, I consider distributed feedback (DFB) resonators. To this end, I employ a stamp with a periodic line pattern (3600 lines/mm, i.e periodicity: Λ = 278 nm) for the thermal imprint. The stamp is a commercially available diffraction grating (ThorLabs®, GH25-36U, **Figure 6.5.1.1a**). The procedure for the imprinting process is similar to planar hot pressing. To fabricate a $CsPbBr_3$ DFB laser, I can either spin-coat perovskite on a substrate and directly imprint it with the stamp or spin-coat the perovskite thin film on a pre-patterned substrate and flattened it by planar hot pressing process.

Direct imprinting

The pristine perovskite layers, spin-coated on glass substrates, are directly patterned by thermal imprint (**Figure 6.5.1.1a**) resulting in a perovskite layer with a sinusoidal grating

structure as shown in the SEM image of the cross section (**Figure 6.5.1.1b**). As can be seen, the pattern of the stamp is perfectly replicated into the $CsPbBr_3$ layers.

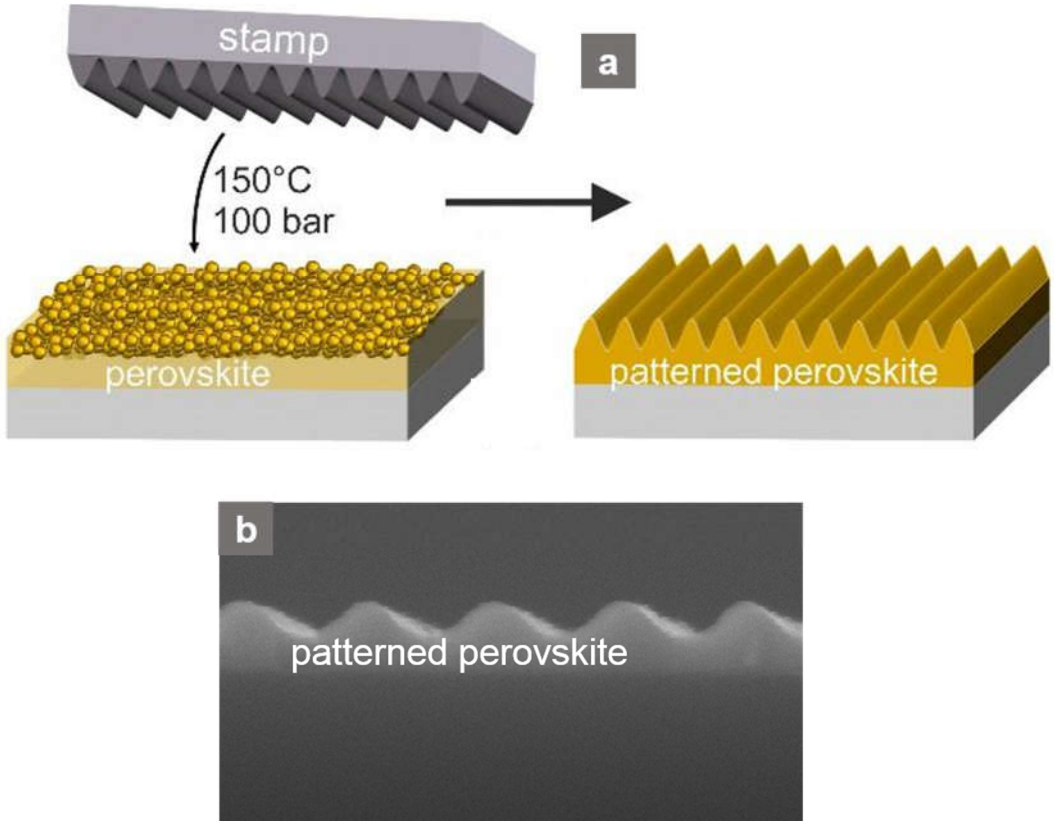

Figure 6.5.1.1. *a) Schematic of the direct thermal imprint of a linear grating (periodicity Λ = 278 nm) into the perovskite layer. Glass is used as a substrate. b) SEM image of the cross section of the patterned perovskite layer.*

Upon pulsed optical pumping by a 355 nm pump laser with a pulse duration of 300 ps, and a repetition rate of 1 kHz (the excitation spot has an area of 0.45 mm^2) , laser emission is found at λ_L = 538.32 nm above a threshold of 10 $\mu J/cm^2$ (**Figure 6.5.1.2a**). The laser emission is detected perpendicular to the sample surface and the emission spectrum shows a full width at half maximum of 0.14 nm (limited by the resolution of the spectrometer) which is significantly narrower than the ASE spectrum (**Figure 6.5.1.2b**). In agreement with the collapse of the width of the emission spectrum, the output power shows an abrupt

increase for excitation levels above the threshold which is the characteristic behaviour for the transition from spontaneous emission to lasing (**Figure 6.5.1.2c**). Note, the emission wavelength can be understood in the framework of a second order DFB laser, where the Bragg condition is given by $\lambda_L = n_{eff} \times \Lambda$. Accordingly, n_{eff} denoting the effective refractive index of the laser mode is $n_{eff} = 1.938$.

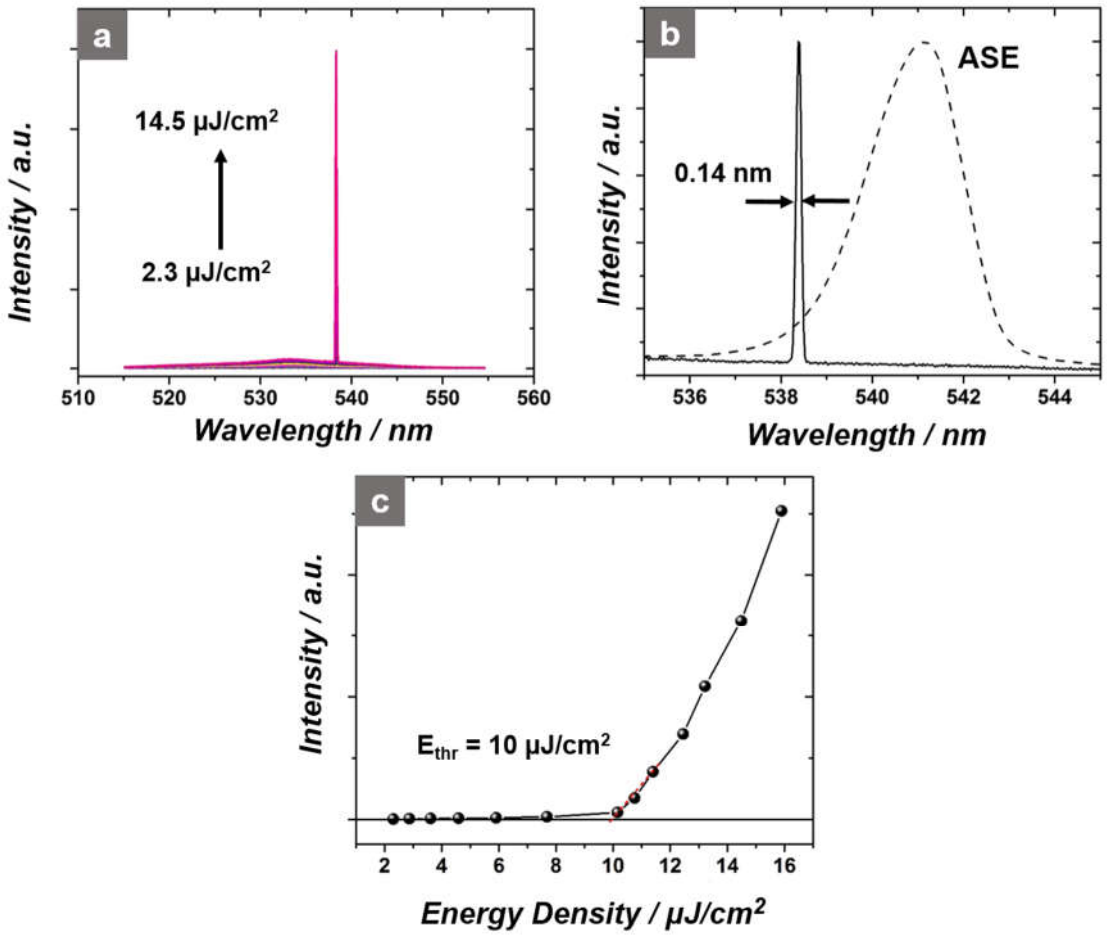

Figure 6.5.1.2. *a) Optical emission spectra upon optical pumping with increasing energy density 2.3–14.5 µJ/cm². b) High resolution spectrum of the DFB laser emission line. The ASE spectrum of a flattened layer is shown for comparison (see also Figure 6.3.9a). c) Laser output characteristics.*

Indirect imprinting

In contrast to the direct patterning of the perovskite layer, I can also use a pre-patterned substrate to form a DFB perovskite laser (**Figure 6.5.1.3**). Specifically, glass substrates

are coated with a resin (Ormocore, micro resist technology GmbH), which is optically highly transparent and can be patterned by thermal imprint. For the patterning of the Ormocore layer, I again use the diffraction grating as stamp (the one used for direct imprinting). The perovskite layer is coated on top of these pre-patterned substrates and is subsequently recrystallized and flattened by thermal imprint using a flat silicon stamp (**Figure 6.5.1.3**). The SEM cross section image shows the perfect filling of the grooves of the substrate with the perovskite and the flat surface of the perovskite layer.

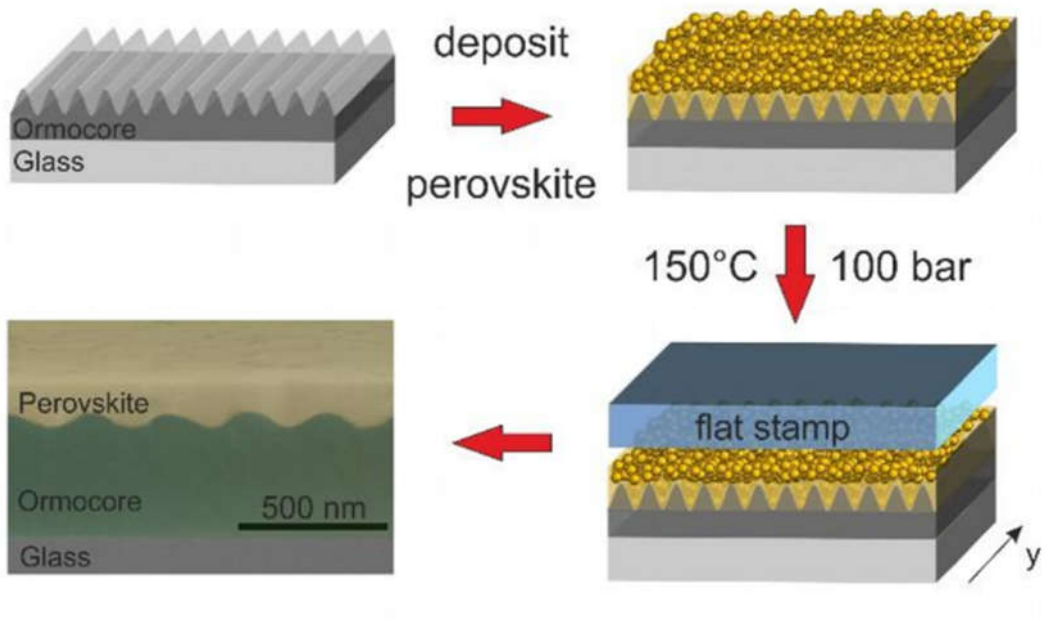

Figure 6.5.1.3. *Schematic of preparing a perovskite DFB laser on a pre-patterned carrier.*

Upon pulsed optical pumping, lasing can be achieved with a likewise low threshold of 7.2 $\mu J/cm^2$ (at λ = 539.1 nm) and narrow linewidth (**Figure 6.5.1.4a-c**). The inset in **Figure 6.5.1.4c** shows the dual lobed far-field emission spectrum above threshold, which is characteristic for DFB lasers with predominant complex coupling [143]. As verified in **Figure 6.5.1.4d**, the emission is characterised by a typical strong linear polarization.

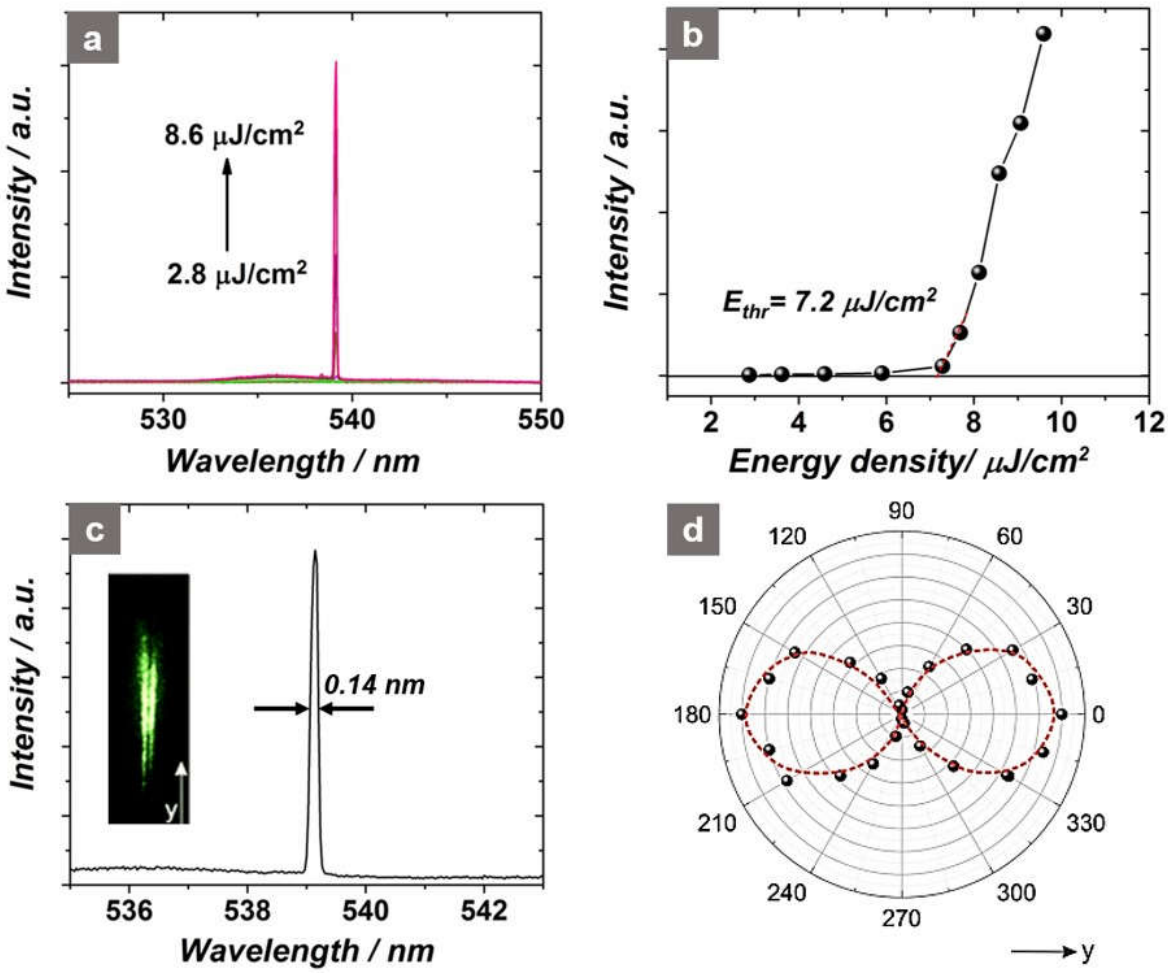

Figure 6.5.1.4. *a) Optical emission spectra, and b) output intensity upon increasing the pumping energy density 2.8–8.6 μJ/cm². c) High resolution spectrum of the laser emission line (inset: photograph of the far-field emission profile). d) Polarization characteristics of the 2nd order DFB laser emission. The results shown in this Figure and in Figure 6.5.1.2 represent the first all-inorganic $CsPbBr_3$ thin-film distributed feedback lasers. Their low-threshold operation at room temperature is made possible by the recrystallization by thermal imprint.*

6.5.2. Vertical cavity surface emitting laser (VCSEL)

Aside from DFB resonators, vertical cavity surface emitting lasers (VCSELs) are very attractive for a number of applications, due to their circular beam profile and potentially small footprint. The only all-inorganic perovskite VCSELs reported so far were based on

$CsPbBr_3$ nanocrystals as gain medium [169, 170]. Here, I employ recrystallized thin films instead to achieve ultralow threshold levels. Specifically, I utilize commercially available dielectric flat mirrors (ThorLabs, FD1M) with transmission characteristics as shown in **Figure 6.5.2.1**. Importantly, these mirrors show a reflection of up to 99.79% in the spectral region of 530-570 nm.

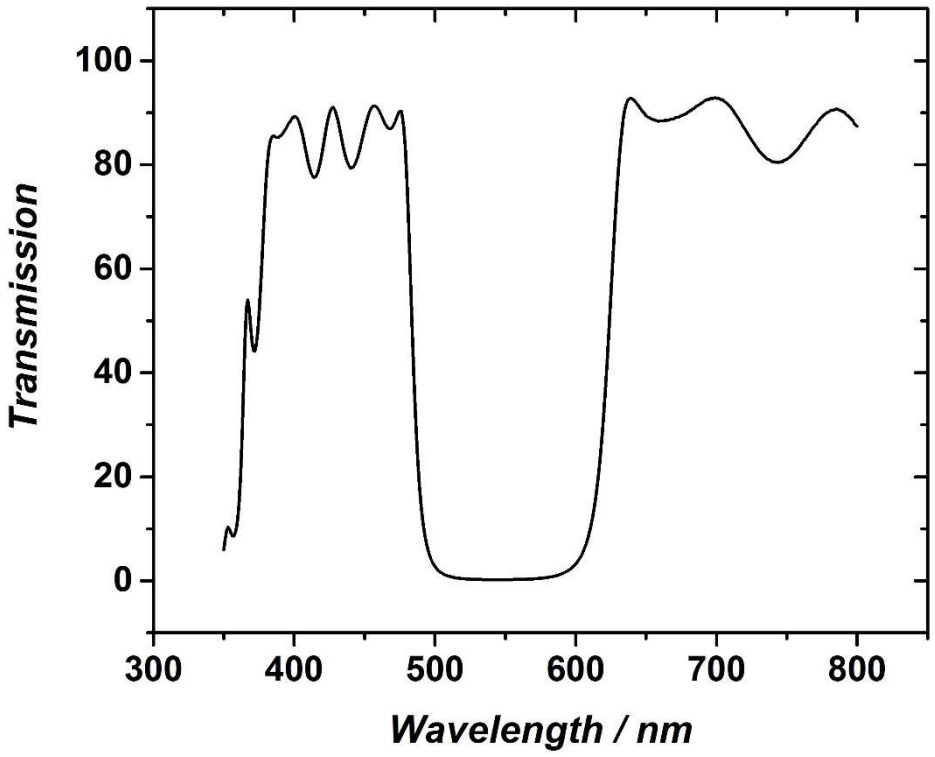

Figure 6.5.2.1. *Transmission spectrum of the dielectric mirrors (ThorLabs FD1M) used to prepare the perovskite VCSEL.*

The VCSEL layout in this study is schematically shown in **Figure 6.5.2.2a**. Briefly, I use one of the dielectric mirrors as a substrate onto which a caesium lead bromide layer is coated. An identical mirror is then used as a stamp for the thermal imprint / recrystallization process (150°C, 100 bar). Afterwards the stamp is left attached on top of the recrystallized perovskite layer, and the entire assembly forms the VCSEL. Below threshold the luminescence spectrum is characterised by marked resonator modes (**Figure 6.5.2.2b**). The respective spacing ($\Delta\lambda$) of these modes allows me to derive the effective

cavity length $L_{eff} = \lambda^2/(2\times\Delta\lambda) \approx 2.3$ µm. Note, the perovskite layer is about 110 nm thick. Upon pulsed excitation, the VCSEL shows lasing with a threshold of 2.2 µJ/cm^2 (**Figure 6.5.2.2c**). Note, for VCSELs based on $CsPbBr_3$ nano-crystals as gain media a threshold of 0.39 µJ/cm^2 has been reported by Huang et al., albeit upon pumping with fs-pulses [169].

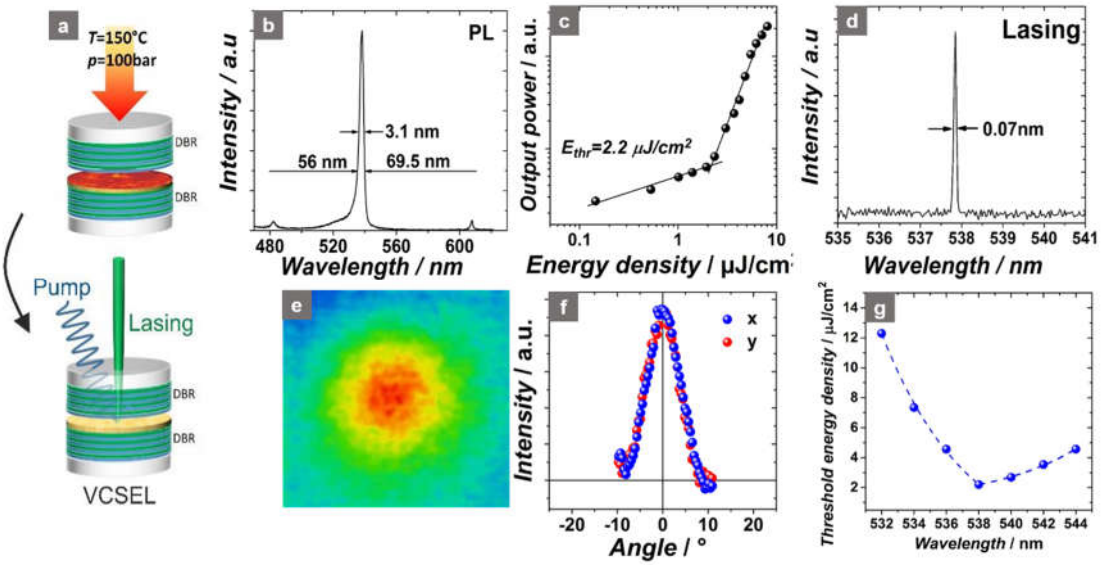

Figure 6.5.2.2. *a) Schematic of VCSEL setup. b) Cavity mode spectrum below threshold. c) Output power vs. pump energy density. d) Emission spectrum and e,f) far-field beam characteristics of the VCSEL above threshold. The laser beam has been directed on a sandblasted glass screen that had been positioned in a distance of 3 cm from the VCSEL surface. g) Laser threshold energy density in dependence on the emission wavelength (wavelength varies due to thickness variation).*

When the authors used ns-pulses instead, they observed an increase of the threshold by more than two orders of magnitude to 98 µJ/cm^2. This striking phenomenon was attributed to an increased thermal load under ns-excitation because the thermally insulating shell of the ligands attached to the nanocrystals prevented efficient thermal transport. At the same time, the authors found a decay time of ~10 ps for stimulated emission, which could likewise account for the marked increase of threshold upon ns-pumping. A similar increase of the ASE threshold from 5.3 µJ/cm^2 to 450 µJ/cm^2 has

been found by Yakunin et al. when going from fs- to ns-excitation [152]. The authors explained their finding with the duration of the pump pulse either being substantially shorter or longer compared with the ASE decay time of ~ 100 ps of the gain medium.

Compared to the fs-data in these reports, my $CsPbBr_3$ thin-film VCSELs were pumped with relatively 'long' pulses of 300 ps. As such, the low threshold level of 2.2 $\mu J/cm^2$ for my lasers is therefore even the more notable and points to the excellent material quality of the gain medium. The VCSEL emission spectrum is very narrow ($\Delta\lambda$ = 0.7 Å, limit of the spectral resolution of the spectrometer) (**Figure 6.5.2.2d**) and the emitted beam shows circular symmetry (**Figure 6.5.2.2e, f**).

Thanks to a (unintentional) variation of the perovskite layer thickness (105-205 nm), which leads to some tuning of the resonator length, I was able to likewise tune the laser emission spectrum between λ = 532-544 nm (**Figure 6.5.2.2g**). Note, the reflectance of the DBR mirrors remains essentially unchanged in this region, which is why I can attribute the variation in the threshold energy density to correspond to the thickness-induced change of spectral shape of the gain spectrum of the active medium.

6.6. Summary

In summary, I have shown highly efficient photoluminescence (PLQY = 68%), amplified spontaneous emission and low-threshold lasing in thin-films of caesium lead bromide at room temperature for the first time. Importantly, the layers are not based on nanocrystals or quantum dots but consist of extended continuous layers, that formed upon recrystallization of as-deposited layers by thermal imprint (100 bar, 150°C). I am able to prepare phase pure 3D $CsPbBr_3$ films, and I provide evidence, that the presence of the 2D $CsPb_2Br_5$ phase is not required to render these layers excellent light emitters and active gain media. Building on these recrystallized layers, I demonstrate the first caesium lead bromide thin-film distributed feedback (DFB) and vertical cavity surface emitting lasers (VCSELs) with ultralow threshold (2.2 $\mu J/cm^2$, 300 ps pump pulses) at room-temperature, that do not rely on the use of nanoparticles. The results render caesium lead

bromide thin-films an excellent material platform for perovskite laser diodes in the future. I also expect that these results will lead to the revision of the paradigm that efficient room-temperature light emission from $CsPbX_3$ perovskites could only be achieved with nanoparticles.

Chapter 7

Conclusions and Outlook

Metal halide perovskite semiconductors have been demonstrated as promising gain materials for tunable semiconductor lasers; it is believed that they pave the way for the fabrication of tunable and low cost electrically operated laser diodes. This is because of their excellent properties, which include: spectral emission tunability, high optical absorption coefficients, solution processability at low temperatures, long carrier lifetimes, being almost defect free and high quantum efficiencies.

I began my study by forming $MAPbI_{3-x}Cl_x$ separated NCs. This decision was made, primarily, because organometal halide perovskites have been investigated to be promising semiconductor materials for achieving low-cost and high-performance optoelectronic devices; and because generally active layers in these applications consist of perovskite NCs sized on the order of 100 nm. A noticeable observation in this study was the fluorescence intermittency from the perovskite NCs (with dimensions of about 100 nm) when illuminated by a laser with a power density of 1.8 W/cm^2. It is demonstrated that by increasing the illumination power density to 18 W/cm^2, fluorescence fluctuation stops. This is an indication that intermittency results from the presence of trap states within the perovskite, and that these states are filled via an increase of laser power density. It was

then determined that this intermittency is dependent on the size of the NCs. An increase in the size of the nanocrystals meant that constant fluorescence was observed. This demonstrates that a key parameter in the formation of high-quality perovskite layers, that will be suitable for optoelectronic devices, is controlling the size of the perovskite grains.

Thereafter, I can show for the first time that thermal imprinting can be applied directly into both all-inorganic and organic-inorganic perovskites (including $MAPbI_3$, $MaPbBr_3$, and $CsPbBr_3$) without any indication of decomposition. It can be demonstrated that over this process, as-deposited spin-coated rough perovskite thin films are recrystallized into substantially flat layers. This smooth morphology is an essential key for unlocking low waveguide losses and affording low thresholds for lasing. Moreover, it is observed that there is a noticeable increase of the perovskite grain sizes. This is necessary for the reduction of defect density regarding the fluorescence intermittency phenomena that was previously discussed. Thereby, lasing at room temperature with extremely low thresholds is achieved.

Thin films of $MAPbI_3$, which have been extensively used in various electronic devices (such as solar cells, LEDs, and Lasers) are deposited through spin-coating. This results in the formation of rough, polycrystalline layers that are typical for spin-coated perovskite layers. These layers are then used as starting films for the NIL process. After imprinting, layers are drastically smoothened and the grain sizes increase. Moreover, it is observed that due to the recrystallization in the NIL process, the density of surface defects is noticeably decreased to levels much lower than those that can be achieved through chemical passivation techniques; thus proving that the material quality is improved after the imprinting process. In regards to the morphological and optical improvements of the perovskite material; considerably low threshold lasing (3.8 $\mu J/cm^2$) at 787.6 nm can be achieved at room temperature. In addition, it is illustrated that the lasing wavelength can be tuned by merely changing the position of the laser beam on the perovskite surface (which results from a spatial inhomogeneity due to the spin-coating process).

Although the fabrication of semiconductor lasers in the "green gap" region has been challenging, it has also been of great interest. This is the leading reason why I decided to replace the $MAPbI_3$ with $MAPbBr_3$ (which emits light in this particular region) in the next stage of the investigation. After this replacement, the NIL process was applied to the $MAPbBr_3$ layers (deposited through spin-coating). As expected, very rough pristine layers are formed as a direct result of spin-coating, which makes them unsuitable for application into the DFB laser. The high percentage of scattering that arises from these layers, leads to an increase in the lasing threshold. Bragg resonator gratings with periodicities of 300 nm are then imprinted into the perovskite layers, resulting in lasing with extremely low thresholds of 3.4 $\mu J/cm^2$ (at room temperature) in the green region. This significantly low threshold is indicative of the remarkable material quality achieved after imprinting. Furthermore, the wavelength can be tuned between 543.3 nm and 557.4 nm by targeting different locations on the sample, as I am already aware that the thickness of the perovskite is continuously changing. Note, this is the first DFB laser that is based on $MAPbBr_3$.

To better analyse the improvement in the perovskite quality, I can use a flat silicon stamp (without any patterns) to apply temperature and pressure via the NIL process, in a controlled experiment (planar hot pressing, PHP). The recrystallization in the PHP process, converts rough and polycrystalline $MAPbBr_3$ layers into extremely flat layers (with a surface roughness of 0.6nm - a value that is limited by the roughness of flat silicon stamp) consisting of extended single crystals. Both the smoothening of the layers (which reduces scattering), and the enlargement of the grains (which decreases the role of defect/trap states), are two important factors for achieving a low lasing threshold. This has already been shown in the fabricated $MAPbI_3$ and $MAPbBr_3$ DFB lasers.

Caesium lead halide perovskites are considered to be more stable than organic-inorganic perovskites. This is because the volatile organic moiety is replaced by an inorganic cation, which in this case is Caesium, thus making it an area of interest for light-emitting diodes and lasers. Until now, thin films of $CsPbX_3$ have typically afforded very low PLQY (< 20%) and ASE only at cryogenic temperatures, since defect related non-radiative

recombination has always been dominating at RT. It is currently thought that, for light emission from lead halide perovskites at RT to be efficient, the charge carriers/excitons need to be confined to the nanometre scale. An example of where this confinement would need to take place would be in $CsPbX_3$ nanoparticles (NPs). Here, thin films of caesium lead bromide, which show a high PLQY of 68% and a low threshold ASE at RT, are presented. As-deposited layers are recrystallized by thermal imprint, which results in continuous films (100% coverage of the substrate), composed of large crystals with micrometre lateral extensions. Using these layers, the first caesium lead bromide thin film DFB and VCSELs with ultralow thresholds at RT (that do not rely on the use of NPs) are demonstrated. The presented results advise a revision of the paradigm that efficient light emission from $CsPbX_3$ perovskites can only be achieved with NPs.

It is foreseen that the results achieved by the thermal NIL process will have a broader impact beyond perovskite lasers, eg., LEDs and solar cells. An in situ investigation of the NIL process is required to better analyse the influence of pressure and temperature on morphological, and optical properties, so that I can have a more accurate control over the process, and by that, for example, lasing threshold could be reduced even further.

In this study, lasing has been achieved in the infrared and green regions by using iodine- and bromine- based perovskite materials. Some applications also require light emission wavelengths in the blue region. To achieve lasing in this area, Cl should be used as the halide part in the perovskite compound. However, until now, room temperature lasing has not yet been achieved from Cl-based perovskite thin films. So far, only methylammonium lead chloride ($MAPbCl_3$) perovskite thin films have shown ASE, but this has been under low temperatures, due to the high defect densities that result from Cl rich compositions.

If I take into consideration the demand for room-temperature lasing in the blue spectral region, and the success in achieving lasing from $CsPbBr_3$ thin films by thermal NIL; I can thereby assume that another individual can now use this information to investigate the influence of NIL on optical, and morphological properties of Cl-based perovskites. From

this they can then see if amplified spontaneous emission can be fulfilled, and by hopefully fabricating the DFB laser, or VCSEL, perovskite blue lasers may come into existence.

References

1. M. Lehnhardt, T. Riedl, T. Weimann, W. Kowalsky, "Impact of triplet absorption and triplet-singlet annihilation on the dynamics of optically pumped organic solid-state lasers", Phys. Rev. B, **2010**, 81, 165206.

2. T. Rabe, P. Görrn, M. Lehnhardt, M. Tilgner, T. Riedl, W. Kowalsky, "Highly Sensitive Determination of the Polaron-Induced Optical Absorption of Organic Charge-Transport Materials", Phys. Rev. Lett., **2009**, 102, 137401.

3. M. Lehnhardt, T. Riedl, U. Scherf, T. Rabe, W. Kowalsky, "Spectrally separated optical gain and triplet absorption: Towards continuous wave lasing in organic thin film lasers", Org. Electron.", **2011**, 12, 1346.

4. H. Zhu, Y. Fu, F. Meng, X. Wu, Z. Gong, Q. Ding, M. V. Gustafsson, M. T. Trinh, S. Jin, X. Y. Zhu, "Lead halide perovskite nanowire lasers with low lasing thresholds and high quality factors", Nat. Mater. ,**2015**, 14, 636.

5. Y. Fu, H. Zhu, A. W. Schrader, D. Liang, Q. Ding, P. Joshi, L. Hwang, X. Y. Zhu, S. Jin, "Nanowire Lasers of Formamidinium Lead Halide Perovskites and Their Stabilized Alloys with Improved Stability", Nano Lett., **2016**, 16, 1000.

6. Q. Zhang, S. T. Ha, X. Liu, T. C. Sum, Q. Xiong, "Room-Temperature Near-Infrared High-Q Perovskite Whispering-Gallery Planar Nanolasers", Nano Lett., **2014**, 14, 5995.

7. F. Deschler, M. Price, S. Pathak, L. E. Klintberg, D.-D. Jarausch, R. Higler, S. Hüttner, T. Leijtens, S. D. Stranks, H. J. Snaith, M. Atatüre, R. T. Phillips, R. H. Friend, "High Photoluminescence Efficiency and Optically Pumped Lasing in Solution-Processed Mixed Halide Perovskite Semiconductors", J. Phys. Chem. Lett., **2014**, 5, 1421.

8. B. R. Sutherland, S. Hoogland, M. M. Adachi, C. T. O. Wong, E. H. Sargent, "Conformal Organohalide Perovskites Enable Lasing on Spherical Resonators", ACS Nano, **2014**, 8, 10947.

9. S. Chen, K. Roh, J. Lee, W. K. Chong, Y. Lu, N. Mathews, T. C. Sum, A. Nurmikko, "A Photonic Crystal Laser from Solution Based Organo-Lead Iodide Perovskite Thin Films", ACS Nano., **2016**, 10, 3959.

10. Y. Jia, R. A. Kerner, A. J. Grede, A. N. Brigeman, B. P. Rand, N. C. Giebink, "Diode-Pumped Organo-Lead Halide Perovskite Lasing in a Metal-Clad Distributed Feedback Resonator", Nano. Lett., **2016**, 16, 4624.

11. V. M. Goldschmidt, "Die Gesetze Der Krystallochemie (The Laws of Cristallochemistry)", .Naturwissenschaften, **1926**,14, 477.

12. L. Liang, L. Wencong, C. Nianyi, "On the Criteria of Formation and Lattice Distortion of Perovskite Type Complex Halides", J. Phys. Chem. Solids., **2004**, 65, 855.

13. C. Li, X. Lu, W. Ding, L. Feng, Y. Gao, Z. Guo, "Formability of ABX_3 (X = F, Cl, Br, I) Halide Perovskites", Acta Crystallogr. Sect. B Struct. Sci., **2008**, 64, 702.

14. A. Kojima, K. Teshima, Y. Shirai, T. Miyasaka, "Organometal Halide Perovskites as Visible-Light Sensitizers for Photovoltaic Cells", J. Am. Chem. Soc., **2009**, 131, 6050.

15. https://www.nrel.gov/pv/assets/pdfs/best-research-cell-efficiencies.20190802.pdf

16. K. Yoshikawa, H. Kawasaki, W. Yoshida, T. Irie, K. Konishi, K. Nakano, T. Uto, D. Adachi, M. Kanematsu, H. Uzu, K. Yamamoto, "Silicon heterojunction solar cell with interdigitated back contacts for a photo conversion efficiency over 26%", Nature Energy, **2017**, 2, 17032.

17. B. R. Sutherland, E. H. Sargent, "Perovskite photonic sources", Nat. Photonics, **2016**, 10, 295.

18. S. D. Stranks, H. J. Snaith, "Metal-halide perovskites for photovoltaic and light-emitting devices", Nat. Nanotechnol. **2015**, 10, 391.

19. S. Adjokatse, H.-H. Fang, M. A. Loi, "Broadly tunable metal halide perovskites for solid-state light-emission applications", Materials Today, **2017**, 20, 413.

20. H. Cho, S.-H. Jeong, M.-H. Park, Y.-H. Kim, C. Wolf, C.-L. Lee, J. H. Heo, A. Sadhanala, N. Myoung, S. Yoo, S. H. Im, R. H. Friend, T.-W. Lee, "Overcoming the electroluminescence efficiency limitations of perovskite light-emitting diodes", Science, **2015**, 350, 1222.

21. W. Xu, Q. Hu, S. Bai, C. Bao, Y. Miao, Z. Yuan, T. Borzda, A. J. Barker, E. Tyukalova, Z. Hu, M. Kawecki, H. Wang, Z. Yan, X. Liu, X. Shi, K. Uvdal, M. Fahlman, W. Zhang, M. Duchamp, J.-M. Liu, A. Petrozza, J. Wang, L.-M. Liu, W. Huang, F. Gao, "Rational molecular passivation for high-performance perovskite light-emitting diodes", Nature Photonics, **2019**, 13, 418.

22. T. Langer, A. Kruse, F. A. Ketzer, A. Schwiegel, L. Hoffmann, H. Jönen, H. Bremers, U. Rossow, A. Hangleiter, "Origin of the “green gap”: Increasing nonradiative recombination in indium-rich GaInN/GaN quantum well structures", physica status solidi c, **2011**, 8, 2170.

23. J.S. Manser, J. A. Christians, P. V. Kama, "Intriguing Optoelectronic Properties of Metal Halide Perovskites", Chem. Rev., **2016**, 116, 12956.

24. N. J. Jeon, J. H. Noh, Y. C. Kim, W. S. Yang, S. Ryu, S. I. Seok, "Solvent engineering for high-performance inorganic-organic hybrid perovskite solar cells", Nat. Mater., **2014**, 13, 897.

25. J. H. Im, I. H. Jang, N. Pellet, M. Grätzel, N.-G. Park, "Growth of $CH_3NH_3PbI_3$ cuboids with controlled size for high-efficiency perovskite solar cells", Nat. Nano-technol., **2014**, 9, 927.

26. M. Liu, M. B. Johnston, H. J. Snaith, "Efficient planar heterojunction perovskite solar cells by vapour deposition", Nature, **2013**, 501, 395.

27. K. Hwang, Y. S. Jung, Y. J. Heo, F. H. Scholes, S. E. Watkins, J. Subbiah, D. J. Jones, D.-Y. Kim, D. Vak, "Toward Large Scale Roll-to-Roll Production of Fully Printed Perovskite Solar Cells", Adv. Mater., **2015**, 27, 1241.

28. A. T. Barrows, A. J. Pearson, C. K. Kwak, A. D. F. Dunbar, A. R. Buckley, D. G. Lidzey, "Efficient planar heterojunction mixed-halide perovskite solar cells deposited via spray-deposition", Energy Environ. Sci., **2014**, 7, 2944.

29. S. Das, B. Yang, G. Gu, P. C. Joshi, I. N. Ivanov, C. M. Rouleau, T. Aytug, D. B. Geohegan, K. Xiao, "High-Performance Flexible Perovskite Solar Cells by Using a Combination of Ultrasonic Spray-Coating and Low Thermal Budget Photonic Curing", ACS Photonics, **2015**, 2, 680.

30. Y. Deng, E. Peng, Y. Shao, Z. Xiao, Q. Dong, J. Huang, "Scalable fabrication of efficient organolead trihalide perovskite solar cells with doctor-bladed active layers", Energy Environ. Sci., **2015**, 8, 1544.

31. D. P. Nenon, J. A. Christians, L. M. Wheeler, J. L. Blackburn, E. M. Sanehira, B. Dou, M. L. Olsen, K. Zhu, J. J. Berry, J. M. Luther, "Structural and Chemical Evolution of Methylammonium Lead Halide Perovskites During Thermal Processing From Solution", Energy Environ. Sci., **2016**, 9, 2072.

32. J. S. Manser, B. Reid, P. V. Kamat, "Evolution of Organic–Inorganic Lead Halide Perovskite from Solid-State Iodoplumbate Complexes", J. Phys. Chem. C., **2015**, 119, 17065.

33. G. E. Eperon, V. M. Burlakov, P. Docampo, A. Goriely, H. J. Snaith, "Morphological Control for High Performance, Solution-Processed Planar Heterojunction Perovskite Solar Cells", Adv. Funct. Mater., **2014**, 24, 151.

34. G. Grancini, S. Marras, M. Prato, C. Giannini, C. Quarti, F. De Angelis, M. De Bastiani, G. E. Eperon, H. J. Snaith, L. Manna, A. Petrozza, "The Impact of the Crystallization Processes on the Structural and Optical Properties of Hybrid Perovskite Films for Photovoltaics", J. Phys. Chem. Lett., **2014**, 5, 3836.

35. J. H. Heo, S. H. Im, J. H. Noh, T. N. Mandal, C. S. Lim, J. A. Chang, Y. H. Lee, H. J. Kim, A. Sarkar, M. K. Nazeeruddin, M. Grätzel, S. I. Seok, "Efficient inorganic–organic hybrid heterojunction solar cells containing perovskite compound and polymeric hole conductors", Nat. Photonics, **2013**, 7, 487.

36. M. Xiao, F. Huang, W. Huang, Y. Dkhissi, Y. Zhu, J. Etheridge, A. Gray-Weale, U. Bach, Y. B. Cheng, L. Spiccia, "A Fast Deposition-Crystallization Procedure for Highly Efficient Lead Iodide Perovskite Thin-Film Solar Cells", Angew. Chem. Int. Ed., **2014**, 53, 9898.

37. N. Yantara, S. Bhaumik, F. Yan, D. Sabba, H. A. Dewi, N. Mathews,P. P. Boix, H. V. Demir, S.Mhaisalkar, "Inorganic Halide Perovskites for Efficient Light-Emitting Diodes", J. Phys. Chem. Lett., **2015**, 6, 4360.

38. Z. Wei, A. Perumal, R. Su, S. Sushant, J. Xing, Q. Zhang, S. T. Tan,H. V. Demir, Q.Xiong, "Solution-processed highly bright and durable cesium lead halide perovskite light-emitting diodes", Nanoscale, **2016**, 8, 18021.

39. P. W. Liang, C. Y. Liao, C. C. Chueh, F. Zuo, S. T. Williams, X. K. Xin, et al., "Additive enhanced crystallization of solution-processed perovskite for highly efficient planar-heterojunction solar cells", Adv. Mater., **2014**, 26, 3748.

40. C. G. Wu, C. H. Chiang, Z. L. Tseng, M. K. Nazeeruddin, A. Hagfeldt, M. Grätzel, "High efficiency stable inverted perovskite solar cells without current hysteresis", Energy Environ. Sci., **2015**, 8, 2725.

41. N. Adhikari, A. Dubey, E. A. Gaml, B. Vaagensmith, K. M. Reza, S. A. A.Mabrouk, et al., "Crystallization of a perovskite film for higher performance solar cells by controlling water concentration in methyl ammonium iodide precursor solution", Nanoscale, **2016**, 8, 2693.

42. Y. Hu, Q. Wang,Y. L. Shi, M. Li, L. Zhang, Z. K. Wang, L. S. Liao. "Vacuum-evaporated all inorganic cesium lead bromine perovskites for high-performance light-emitting diodes", J. Mater. Chem. C, **2017**, 5, 8144.

43. L. Zhang, F. Yuan, H. Dong, B. Jiao, W. Zhang, X. Hou, S. Wang, Q. Gong, Z. Wu, "One-Step Co-Evaporation of All-Inorganic Perovskite Thin Films with Room-Temperature Ultralow Amplified Spontaneous Emission Threshold and Air Stability", ACS Appl. Mater. Interfaces, **2018**, 10, 40661.

44. Y. Liu, Y. Zhang, Z. Yang, D. Yang, X. Ren, L. Pang, S. Liu, "Thinness- and Shape-Controlled Growth for Ultrathin Single-Crystalline Perovskite Wafers for Mass Production of Superior Photoelectronic Devices", Adv. Mater., **2016**, 28, 9204.

45. Y. Dang, Y. Liu, Y. Sun, D. Yuan, X. Liu, W. Lu, G. Liu, H. Xia, X. Tao, "Bulk crystal growth of hybrid perovskite material $CH_3NH_3PbI_3$", CrystEngComm, **2015**, 17, 665.

46. Z. Lian, Q. Yan, T. Gao, J. Ding, Q. Lv, C. Ning, Q. Li, J. l. Sun, "Perovskite $CH_3NH_3PbI_3(Cl)$ Single Crystals: Rapid Solution Growth, Unparalleled Crystalline Quality, and Low Trap Density toward 108 cm^{-3}", J. Am. Chem. Soc., **2016**, 138, 9409.

47. D. Shi, V. Adinolfi, R. Comin, M. Yuan, E. Alarousu, A. Buin, Y. Chen, S. Hoogland, A. Rothenberger, K. Katsiev, Y. Losovyj, X. Zhang, P. A. Dowben, O. F. Mohammed, E. H. Sargent, O. M. Bakr, "Low trap-state density and long carrier diffusion in organolead trihalide perovskite single crystals", Science, **2015**, 347, 519.

48. A. A. Zhumekenov, V. M. Burlakov, M. I. Saidaminov, A. Alofi, M. A. Haque, B. Turedi, B. Davaasuren, I. Dursun, N. Cho, A. M. El-Zohry, M. D. Bastiani, A. Giugni, B. Torre, E. D. Fabrizio, O. F. Mohammed, A. Rothenberger, T. Wu, A. Goriely, O. M. Bakr, "The Role of Surface Tension in the Crystallization of Metal Halide Perovskites", ACS Energy Lett., **2017**, 2, 1782.

49. M. I. Saidaminov, A. L. Abdelhady, B. Murali, E. Alarousu, V. M. Burlakov, W. Peng, I. Dursun, L. Wang, Y. He, G. Maculan, A. Goriely. T. Wu, O. F. Mohammed, O. M. Bakr, "High-quality bulk hybrid perovskite single crystals within minutes by inverse temperature crystallization", Nat. Commun., **2015**, 6, 7586.

50. L. Protesescu, S. Yakunin, M. I. Bodnarchuk, F. Krieg, R. Caputo, C. H. Hendon, R. X. Yang, A. Walsh, M. V. Kovalenko, "Nanocrystals of Cesium Lead Halide Perovskites ($CsPbX_3$, X = Cl, Br, and I): Novel Optoelectronic Materials Showing Bright Emission with Wide Color Gamut", Nano Lett., **2015**, 15, 6, 3692.

51. D. Zhang, Y. Yang, Y. Bekenstein, Y. Yu, N. A. Gibson, A. B. Wong, S. W. Eaton, N. Kornienko, Q. Kong, M. Lai, A. P. Alivisatos, S. R. Leone, P. Yang, "Synthesis of Composition Tunable and Highly Luminescent Cesium Lead Halide Nanowires through Anion-Exchange Reactions", J. Am. Chem. Soc., **2016**, 138, 23, 7236.

52. J. H. Noh, S. H. Im, J. H. Heo, T. N. Mandal, SI.I Seok, "Chemical Management for Colorful, Efficient, and Stable Inorganic–Organic Hybrid Nanostructured Solar Cells", Nano Lett., **2013**, 13, 4, 1764.

53. G. Nedelcu, L. Protesescu, S. Yakunin, M. I. Bodnarchuk, M. J. Grotevent, M. V. Kovalenko, "Fast Anion-Exchange in Highly Luminescent Nanocrystals of Cesium Lead Halide Perovskites ($CsPbX_3$, X= Cl^-, Br^-, I^-)", Nano Lett., **2015**, 15, 5635.

54. Q. A. Akkerman, V. D'Innocenzo, S. Accornero, A. Scarpellini, A. Petrozza, M. Prato, L. Manna, "Tuning the Optical Properties of Cesium Lead Halide Perovskite Nanocrystals by Anion Exchange Reactions", J. Am. Chem. Soc., **2015**, 137, 10276.

55. S. Tao, I. Schmidt, G. Brocks, J. Jiang, I. Tranca, K. Meerholz, S. Olthof, "Absolute energy level positions in tin-and lead-based halide perovskites", Nat. Commun., **2019**, 10, 2560.

56. S. N. Habisreutinger, D. P. McMeekin, H. J. Snaith, R. J. Nicholas, "Research Update: Strategies for improving the stability of perovskite solar cells", APL Mater., **2016**, 4, 091503.

57. D. Song, J. Ji,1 Y. Li, G. Li, M. Li, T. Wang, D. Wei, P. Cui, Y. He, J. M. Mbengue, "Degradation of organometallic perovskite solar cells induced by trap states", Appl. Phys. Lett., **2016**, 108, 093901.

58. J. A. Christians, P. A. M. Herrera, P. V. Kamat, "Transformation of the Excited State and Photovoltaic Efficiency of $CH_3NH_3PbI_3$ Perovskite upon Controlled Exposure to Humidified Air", J. Am. Chem. Soc., **2015**, 137, 1530.

59. B. Conings, J. Drijkoningen , N. Gauquelin , A. Babayigit , J. D'Haen , L. D'Olieslaeger , A. Ethirajan , J. Verbeeck , J. Manca , E. Mosconi , F. D. Angelis , H. G. Boyen, "Intrinsic Thermal Instability of Methylammonium Lead Trihalide Perovskite", Adv. Energy Mater., **2015**, 5, 1500477.

60. E. J. Juarez-Perez, Z. Hawash, S. R. Raga, L. K. Ono, Y. Qi, "Thermal degradation of $CH_3NH_3PbI_3$ perovskite into NH_3 and CH_3I gases observed by coupled thermogravimetry–mass spectrometry analysis", Energy Environ. Sci., **2016**, 9, 3406.

61. G. E. Eperon, S. D. Stranks, C. Menelaou, M. B. Johnston, L. M. Herza, H. J. Snaith, "Formamidinium lead trihalide: a broadly tunable perovskite for efficient planar heterojunction solar cells", Energy Environ. Sci., **2014**, 7, 982.

62. N. J. Jeon, J. H. Noh, W. S. Yang, Y. C. Kim, S. Ryu, J. Seo, S. Il Seok, "Compositional engineering of perovskite materials for high-performance solar cells", Nature, **2015**, 517, 476.

63. G. E. Eperon, G. M. Paternò, R. J. Sutton, A. Zampetti, A. A. Haghighirad, F. Cacialli, H. J. Snaith, "Inorganic caesium lead iodide perovskite solar cells", J. Mater. Chem. A, **2015**, 3, 19688.

64. R. E. Beal, D. J. Slotcavage, T. Leijtens, A. R. Bowring, R. A. Belisle, W. H. Nguyen, George F. Burkhard, E. T. Hoke, M. D. McGehe, "Cesium Lead Halide Perovskites with Improved Stability for Tandem Solar Cells", J. Phys. Chem. Lett., **2016**, 7, 746.

65. A. F. Akbulatov, S. Yu. Luchkin, L. A. Frolova, N. N. Dremova, K. L. Gerasimov, I. S. Zhidkov, D. V. Anokhin, E. Z. Kurmaev, K. J. Stevenson, P. A. Troshin, "Probing the Intrinsic Thermal and Photochemical Stability of Hybrid and Inorganic Lead Halide Perovskites", J. Phys. Chem. Lett., **2017**, 8, 6, 1211.

66. M. Kulbak, S. Gupta, N. Kedem, I. Levine, T. Bendikov, G. Hodes, D. Cahen, "Cesium Enhances Long-Term Stability of Lead Bromide Perovskite-Based Solar Cells", J. Phys. Chem. Lett., **2016**, 7, 167.

67. Y. Li, L. Ji, R. Liu, C. Zhang, C. H. Mak, X. Zou, H. H. Shen, S. Y. Leuf, H. Y. Hsu, "A review on morphology engineering for highly efficient and stable hybrid perovskite solar cells", J. Mater. Chem. A, **2018**, 6, 12842.

68. N. Pellet, P. Gao, G. Gregori, T. Y. Yang, M. K. Nazeeruddin, J. Maier, M. Grätzel, "Mixed-Organic-Cation Perovskite Photovoltaics for Enhanced Solar-Light Harvesting", Angew. Chem. Int. Ed., **2014**, 53, 3151.

69. R. Prasanna, A. Gold-Parker, T. Leijtens, B. Conings, A. Babayigit, H. G. Boyen, M. F. Toney , M. D. McGehee, "Band Gap Tuning via Lattice Contraction and Octahedral Tilting in Perovskite Materials for Photovoltaics", J. Am. Chem. Soc., **2017**, 139, 11117.

70. K. A. Bush, K. Frohna, R. Prasanna, R. E. Beal, T. Leijtens, S. A. Swifter, M. D. McGehee, "Compositional Engineering for Efficient Wide Band Gap Perovskites with Improved Stability to Photoinduced Phase Segregation", ACS. Energy Lett., **2018**, 3, 428.

71. Z. Li, M. Yang, J. S. Park, S. H. Wei, J. J. Berry, K. Zhu, "Stabilizing Perovskite Structures by Tuning Tolerance Factor: Formation of Formamidinium and Cesium Lead Iodide Solid-State Alloys", Chem. Mater., **2016**, 28, 284.

72. M. Saliba. T. Matsui, J. Y. Seo, K. Domanski, J. P. Correa-Baena, M. K. Nazeeruddin, S. M. Zakeeruddin, W. Tress, A. Abate, A. Hagfeldtd, M. Grätzel, "Cesium-containing triple cation perovskite solarcells: improved stability, reproducibility and highefficiency", Energy Environ. Sci., **2016**, 9, 1989.

73. W. Rehman, D. P. McMeekin, J. B. Patel, R. L. Milot, M. B. Johnston, H. J. Snaith, L. M. Herz, "Photovoltaic mixed-cation lead mixed-halide perovskites: links between crystallinity, photo-stability and electronic properties ", Energy Environ. Sci., **2017**, 10, 361.

74. M. Saliba, T. Matsui, K. Domanski, J. Y. Seo, A. Ummadisingu, S. M. Zakeeruddin, J. P. Correa-Baena, W. R. Tress, A. Abate, A. Hagfeldt, M. Grätzel, "Incorporation of rubidium cations into perovskite solar cells improves photovoltaic performance", Science., **2016**, 354, 206.

75. N.G. Park, "Perovskite solar cells: an emerging photovoltaic technology", Mater. Today, **2015**, 18, 65.

76. G. Xing, N. Mathews, S.S. Lim, N. Yantara, X. Liu, D. Sabba, M. Grätzel. S. Mhaisalkar, T.C. Sum, "Low-temperature solution-processed wavelength-tunable perovskites for lasing", Nat. Mater., **2014**, 13, 476.

77. W. J. Yin, T. Shi, Y. Yan, "Unique properties of halide perovskites as possible origins of the superior solar cell performance", Adv. Mater., **2014**, 26, 4653.

78. W.-J. W. Yin, J.-H. J. Yang, J. Kang, Y. Yan, S.-H. Wei, "Halide perovskite materials for solar cells: a theoretical review", J. Mater. Chem. A, **2015**, 3, 8926.

79. W.-J. Yin, T. Shi, Y. Yan, "Superior Photovoltaic Properties of Lead Halide Perovskites: Insightsfrom First-Principles Theory", J. Phys. Chem. C, **2015**, 119, 5253.

80. S. De Wolf, J. Holovsky, S.J Moon, P. Löper, B. Niesen, M. Ledinsky, F.J Haug, J.H Yum, C. Ballif, "Organometallic Halide Perovskites: Sharp Optical Absorption Edge and Its Relation to Photovoltaic Performance," J. Phys. Chem. Lett., **2014**, 5, 1035.

81. J. M. Richter, M. Abdi-Jalebi, A. Sadhanala, M. Tabachnyk, J. P. H. Rivett, L. M. PazosOutón, K. C. Gödel, M. Price, F. Deschler, R. H. Friend, "Enhancing photoluminescence yields in lead halide perovskites by photon recycling and light outcoupling", Nat. Commun., **2016**, 7, 13941.

82. **N. Pourdavoud**, T. Haeger, A. Mayer, P. J. Cegielski, A. L. Giesecke, R. Heiderhoff, S. Olthof, S. Zaefferer, I. Shutsko, A. Henkel, D. Becker-Koch, M. Stein, M. Cehovski, O. Charfi, H.-H. Johannes, D. Rogalla, M. Lemme, M. Koch, Y. Vaynzof, K. Meerholz, W. Kowalsky, H.-C. Scheer, P. Görrn, and T. Riedl, "Room Temperature Stimulated Emission and Lasing in Recrystallized Cesium Lead Bromide Perovskite Thin Films", Adv. Mater., **2019**, 31, 1903717.

83. K. Zhang, D. Li, "Electromagnetic Theory for Microwaves and Optoelectronics", 2nd edition. Springer-Verlag, Berlin Heidelberg., **2008**.

84. G. P. Agrawal, N. K. Dutta, "Long Wavelength Semiconductor Lasers", Van Nostrand Reinhold Co.: New York, **1986**.

85. Q. Chen, H. Zhou, T.-B. Song, S. Luo, Z. Hong, H.-S. Duan, L. Dou, Y. Liu, Y. Yang, "Controllable Self-Induced Passivation of Hybrid Lead Iodide Perovskites toward High Performance Solar Cells", Nano Lett., **2014**, 14, 4158.

86. N. K. Noel, A. Abate, S. D. Stranks, E. S. Parrott, V. M. Burlakov, A. Goriely, H. J. Snaith, "Enhanced Photoluminescence and Solar Cell Performance via Lewis Base Passivation of Organic-Inorganic Lead Halide Perovskites", ACS Nano, **2014**, 8, 9815.

87. Y. Tian, A. Merdasa, M. Peter, M. Abdellah, K. Zheng, C. S. Ponseca, T. Pullerits, A. Yartsev, V. Sundström, I. G. Scheblykin, "Giant Photoluminescence Blinking of Perovskite Nano crystals Reveals Single-Trap Control of Luminescence", Nano Lett., **2015**, 15, 1603.

88. Y.-S. Park, S. Guo, N. S. Makarov, V. I. Klimov, "Room Temperature Single-Photon Emission from Individual Perovskite Quantum Dots", ACS. Nano, **2015**, 9, 10386.

89. T. Tachikawa, I. Karimata, Y. Kobori, "Surface Charge Trapping in Organolead Halide Perovskites Explored by Single-Particle Photoluminescence Imaging", J. Phys. Chem. Lett., **2015**, 6, 3195.

90. X. Wen, A. Ho-Baillie, S. Huang, R. Sheng, S. Chen, H.-C. Ko, M. A. Green, "Mobile Charge-Induced Fluorescence Intermittency in Methylammonium Lead Bromide Perovskite", Nano Lett., **2015**, 15, 4644.

91. A. Ruth, M. Hayashi, P. Zapol, J. Si, M. P. McDonald, Y.V. Morozov, M. Kuno, B. Janko´, " Fluorescence intermittency originates from reclustering in two-dimensional organic semiconductors", Nat. Commun., **2017**, 8, 1452.

92. F. Zhang, H. Zhong, C. Chen, X.-g. Wu, X. Hu, H. Huang, J. Han, B. Zou, Y. Dong, "Brightly Luminescent and Color-Tunable Colloidal $CH_3NH_3PbX_3$(X = Br, I, Cl) Quantum Dots: Potential Alternatives for Display Technology", ACS Nano, **2015**, 9, 4533.

93. R. F. Heuff, J. L. Swift, D. T. Cramb, "Fluorescence correlation spectroscopy using quantum dots: advances, challenges and opportunities", Phys. Chem. Chem. Phys., **2007**, 9, 1870.

94. W. E. Moerner, "Examining Nanoenvironments in Solids on the Scale of a Single, Isolated Impurity Molecule", Science, **1994**, 265, 46.

95. J. Schuster, F. Cichos, C. von Borczyskowski, "Blinking of Single Molecules in Various Environments", Opt. Spectrosc., **2005**, 98, 712.

96. M. Nirmal, B. O. Dabbousi, M. G. Bawendi, J. J. Macklin, J. K. Trautman, T. D. Harris, L. E. Brus, "Fluorescence intermittency in single cadmium selenide nanocrystals", Nature, **1996**, 383, 802.

97. V. Protasenko, S. Gordeyev, M. Kuno, "Spatial and Intensity Modulation of Nanowire Emission Induced by Mobile Charges", J. Am. Chem. Soc., **2007**, 129, 13160.

98. A. L. Efros, M. Rosen, "Random Telegraph Signal in the Photoluminescence Intensity of a Single Quantum Dot", Rev. Lett., **1997**, 78, 1110.

99. D. I. Chepic, A. L. Efros, A. I. Ekimov, M. G. Ivanov, V. A. Kharchenko, I. A. Kudriavtsev, T. V. Yazeva, "Auger ionization of semiconductor quantum drops in a glass matrix", J. Lumin., **1990**, 47, 113.

100. D. E. Gomez, M. Califano, Mulvaney, "Optical properties of single semiconductor nanocrystals", Phys. Chem. Chem. Phys., **2006**, 8, 4989.

101. A. A. Cordones, S. R. Leone, "Mechanisms for charge trapping in single semiconductor nanocrystals probed by fluorescence blinking", Chem. Soc. Rev., **2013**, 42, 3209.

102. W. Wang, Z. Zhang, Y. Ca1, J. Chen, J. Wang, R. Huang, X. Lu, X. Gao, L. Shui, S. Wu, J.-M. Liu1, "Enhanced performance of $CH_3NH_3PbI_{3-x}Cl_x$ perovskite solar cells by CH_3NH_3I modification of TiO2-perovskite layer interface", nano scale Res. Lett., **2016**, 11, 316.

103. V. D'Innocenzo, A. R. Srimath Kandada, M. De Bastiani, M. Gandini, A. Petrozza, "Tuning The Light Emission Properties ByBand Gap Engineering In Hybrid Lead Halide Perovskite", J. Am. Chem.Soc., **2014**, 136, 17730.

104. Kuno, M.; Fromm, D. P.; Hamann, H. F.; Gallagher, A.; Nesbitt, D. J., "Nonexponential "blinking" kinetics of single CdSe quantum dots: A universal power law behavior", J. Chem. Phys., **2000**, 112, 3117.

105. J. Tang, R. A. Marcus, "Diffusion-Controlled Electron Transfer Processes and Power-Law Statistics of Fluorescence Intermittency of Nanoparticles", Phys. Rev. Lett., **2005**, 95, 107401.

106. K. T. Shimizu, R. G. Neuhauser, C. A. Leatherdale, S. A. Empedocles, W. K. Woo, M. G Bawendi, " Blinking statistics in single semiconductor nanocrystal quantum dots", Phys. Rev. B, **2001**, 63, 205316.

107. R. W. Meulenberg, J. R. I. Lee, A. Wolcott, J. Z. Zhang, L. J. Terminello, T. van Buuren, "Determination of the Exciton Binding Energy in CdSe Quantum Dots", ACS Nano, **2009**, 3, 325.

108. G. Giorgi, J.-I. Fujisawa, H. Segawa, K. Yamashita, "Small Photocarrier Effective Masses Featuring Ambipolar Transportin Methylammonium Lead Iodide Perovskite: A Density Functional Analysis", J. Phys. Chem. Lett., **2013**, 4, 4213.

109. E. J. Juarez-Perez, R. S. Sanchez,L. Badia, G. Garcia-Belmonte, Y. S. Kang, I. Mora-Sero, J. Bisquert, "Photoinduced Giant Dielectric Constant in Lead Halide Perovskite Solar Cells", J. Phys. Chem. Lett., **2014**, 5, 2390.

110. Q. Lin, A. Armin, R. C. R. Nagiri, P. L. Burn, P. Meredith, "Electro-optics of perovskite solar cells", Nat. Photonics, **2015**, 9, 106.

111. L.-y. Huang, W. R. L. Lambrecht, "Electronic band structure, phonons, and exciton binding energies of halide perovskites $CsSnCl_3$, $CsSnBr_3$, and $CsSnI_3$", Phys. Rev. B, **2013**, 88, 165203.

112. E. Menéndez-Proupin, P. Palacios, P. Wahnón, J. C. Conesa, "Self-consistent relativistic band structure of the $CH_3NH_3PbI_3$ perovskite", Phys. Rev. B, **2014**, 90, 045207.

113. V. D'Innocenzo, G. Grancini, M. J. P. Alcocer, A. R. S. Kandada, S. D. Stranks, M. M. Lee, G. Lanzani, H. J. Snaith,A., Petrozza, "Excitons versus free charges in organo-lead tri-halide perovskites", Nat. Commun., **2014**, 5, 3586.

114. C. Sheng, C. Zhang, Y. Zhai, K. Mielczarek, W. Wang, W. Ma, A. Zakhidov, Z. V. Vardeny, "Exciton versus Free Carrier Photogeneration in Organometal Trihalide Perovskites Probed by Broadband Ultrafast Polarization Memory Dynamics", Phys. Rev. Lett., **2015**, 114, 116601.

115. Y. Tian, M. Peter, E. Unger, M. Abdellah, K. Zheng, T. Pullerits, A. Yartsev, V. Sundstrom, I. G. Scheblykin, "Mechanistic insights into perovskite photoluminescence enhancement: light curing with oxygen can boost yield thousandfold", Phys. Chem. Chem. Phys., **2015**, 17, 24978.

116. J. F. Galisteo-López, M. Anaya, M. E. Calvo, H. Míguez, "Environmental Effects on the Photophysics of Organic−Inorganic Halide Perovskites", J. Phys. Chem. Lett., **2015**, 6, 2200.

117. F. Deschler, M. Price, P. Sandeep, L. E. Klintberg, D.-D. Jarausch, R. Higler, S. Hüttner, T. Leijtens, S. D. Stranks, H. J. Snaith, M. Atatüre, R. T. Phillips, R. H. Friend, "High Photoluminescence Efficiency and Optically Pumped Lasing in Solution-Processed Mixed Halide Perovskite Semiconductor", J. Phys. Chem. Lett., **2014**, 5, 1421.

118. S. D. Stranks, V. M. Burlakov, T. Leijtens, J. M. Ball, A. Goriely, H. J. Snaith, "Recombination Kinetics in Organic-Inorganic Perovskites: Excitons, Free Charge,and Subgap States", Phys. Rev. Applied, **2014**, 2, 034007.

119. S. Chen, A. Nurmikko, "Stable Green Perovskite Vertical-Cavity Surface-Emitting Lasers on Rigid and Flexible Substrates", ACS Photonics, **2017**, 4, 2486.

120. G. Niu, W. Li, F. Meng, L. Wang, H. Dong, Y. Qiu, "Study on the stability of $CH_3NH_3PbI_3$ films and the effect of post-modification by aluminium oxide in all-solid-state hybrid solar cells", J. Mater. Chem. A, **2014**, 2, 705.

121. J. M. Frost, K. T. Butler, A. Walsh, "Molecular ferroelectric contributions to anomalous hysteresis in hybrid perovskite solar cells", APL. Mater., **2014**, 2, 081506.

122. Z. Xiao, C. Bi, Y. Shao, Q. Dong, Q. Wang, Y. Yuan, C. Wang, Y. Gao, J. Huang, "Efficient, high yield perovskite photovoltaic devices grown by interdiffusion of solution-processed precursor stacking layers", Energy Environ. Sci., **2014**, 7, 2619.

123. D. A. Egger, L. Kronik, "Role of Dispersive Interactions in Determining Structural Properties of Organic–Inorganic Halide Perovskites: Insights from First-Principles Calculations", J. Phys. Chem. Lett., **2014**, 5, 2728.

124. J. Emara, T. Schnier, N. Pourdavoud, T. Riedl, K. Meerholz, and S. Olthof, "Impact of Film Stoichiometry on the Ionization Energy and Electronic Structure of $CH_3NH_3PbI_3$ Perovskite", Adv. Mater., **2016**, 28, 553.

125. D. W. deQuilettes, S. M. Vorpahl, S. D. Stranks, H. Nagaoka, G. E. Eperon, M. E. Ziffer, H. J. Snaith, D. S. Ginger, "Impact of microstructure on local carrier lifetime in perovskite solar cells", **2015**, 348, 683.

126. J. W. Lee, H. S. Kim, N. G. Park, "Lewis Acid−Base Adduct Approach for High Efficiency Perovskite Solar Cells", Acc. Chem. Res., **2016**, 49, 311.

127. R. J. Stewart, C. Grieco, A. V. Larsen, J. J. Maier, J. B. Asbury, "Approaching Bulk Carrier Dynamics in Organo-Halide Perovskite Nanocrystalline Films by Surface Passivation", J. Phys. Chem. Lett., **2016**, 7, 1148.

128. N. K. Noel, A. Abate, S. D. Stranks, E. Parrott, V. Burlakov, A. Goriely, H. J. Snaith, "Enhanced Photoluminescence and Solar Cell Performance via Lewis Base Passivation of Organic-Inorganic Lead Halide Perovskites", ACS Nano, **2014**, 8, 9815.

129. D. W. deQuilettes, S. Koch, S. Burke, R. K. Paranji, A. J. Shropshire, M. E. Ziffer, D. S. Ginger, "Photoluminescence Lifetimes Exceeding 8 μs and Quantum Yields Exceeding 30% in Hybrid Perovskite Thin Films by Ligand Passivation", ACS Energy Lett., **2016**, 1, 438.

130. M. Meier, A. Mekis, A. Dodabalapur, A. Timko, R. E. Slusher, J. D. Joannopoulos, O. Nalamasu, "Laser action from two-dimensional distributed feedback in photonic crystals", Appl. Phys. Lett., **1999**, 74, 7.

131. H.-Y. Ryu, S.-H. Kwon, Y.-J. Lee, Y.-H. Lee, J.-S. Kim, "Very-low-threshold photonic band-edge lasers from free-standing triangular photonic crystal slabs", Appl. Phys. Lett., **2002**, 80, 3476.

132. I. D. W. Samuel, E. B. Namdas, G. A. Turnbull, "How to recognize lasing", Nat. Photonics, **2009**, 3, 546.

133. M. Meier, A. Dodabalapur, J. A. Rogers, R. E. Slusher, A. Mekis, A. Timko, C. A. Murray, R. Ruel, O. Nalamasu, "Emission characteristics of two-dimensional organic photonic crystal lasers fabricated by replica molding", J. Appl. Phys., **1999**, 86, 3502.

134. X. Liu, P. Stefanou, B. Wang, T. Woggon, T. Mappes, U. Lemmer, "Organic semiconductor distributed feedback (DFB) laser as excitation source in Raman spectroscopy", Opt. Express, **2013**, 21, 28941.

135. P. Brenner, M. Stulz, D. Kapp, T. Abzieher, U. W. Paetzold, A. Quintilla, I. A. Howard, H. Kalt, U. Lemmer, "Highly stable solution processed metal-halide perovskite lasers on nanoimprinted distributed feedback structures", Appl. Phys. Lett., **2016**, 109, 141106.

136. J.-S. Park, S. Choi, Y. Yan, Y. Yang, J. M. Luther, S.-H. Wei, P. Parilla, K. Zhu, "Electronic Structure and Optical Properties of α-$CH_3NH_3PbBr_3$ Perovskite Single Crystal", J. Phys. Chem. Lett., **2015**, 6, 4304.

137. M. I. Saidaminov, A. L. Abdelhady, B. Murali, E. Alarousu, V. M. Burlakov, W. Peng, I. Dursun, L. Wang, Y. He, G. Maculan, A. Goriely, T. Wu, O. F. Mohammed, O. M. Bakr, "High-quality bulk hybrid perovskite single crystals within minutes by inverse temperature crystallization", Nat. Commun., **2015**, 6, 7586.

138. M. C. M. Morris, F. Howard, E. H. Evans, B. Paretzkin, C. R. Hubbard, S. J. Carmel, digital.library.unt.edu/ark:/67531/metadc13209/ (accessed: April **2017**).

139. H. Kusumoto, T. Kaito, S.-i. Yanagiya, A. Mori, T. Inoue, "Growth of single crystals of $PbBr_2$ in silica gel", J. Cryst. Growth, **2005**, 277, 536.

140. F. J. Martínez-Casado, M. Ramos-Riesco, J. A. Rodríguez-Cheda, F. Cucinotta, E. Matesanz, I. Miletto, E. Gianotti, L. Marchese, Z. Matěj, "Unraveling the Decomposition Process of Lead(II) Acetate:Anhydrous Polymorphs, Hydrates, and Byproducts and RoomTemperature Phosphorescence" , Inorg. Chem. **2016**, 55, 8576.

141. J. H. Heo, D. H. Song, S. H. Im, "Planar $CH_3NH_3PbBr_3$ Hybrid Solar Cells with 10.4% Power Conversion Efficiency, Fabricated by Controlled Crystallization in the Spin-Coating Process", Adv. Mater., **2014**, 26, 8179.

142. H.-J. Yen, P.-W. Liang, C.-C. Chueh, Z. Yang, A. K. Y. Jen, H.-L. Wang, "Large Grained Perovskite Solar Cells Derived from Single-Crystal Perovskite Powders with Enhanced Ambient Stability", ACS Appl. Mater. Interfaces, **2016**, 8, 14513.

143. M. Kasraian, D. Botez, "Single-lobed far-field radiation pattern from surface-emitting complex-coupled distributed-feedback diode lasers", Appl. Phys. Lett., **1995**, 67, 2783.

144. R. J. Noll, S. H. Macomber, "Analysis of grating surface emitting lasers", IEEE J. Quantum Electron., **1990**, 26, 456.

145. N. Pourdavoud, S. Wang, A. Mayer, T. Hu, Y. Chen, A. Marianovich, W. Kowalsky, R. Heiderhoff, H.-C. Scheer, T. Riedl, "Photonic Nanostructures Patterned by Thermal Nanoimprint Directly into Organo-Metal Halide Perovskites", Adv. Mater., **2017**, 29, 1605003.

146. N. Pourdavoud, A. Mayer, M. Buchmüller, K. Brinkmann, T. Häger, T. Hu, R. Heiderhoff, I. Shutsko, P. Görrn, Y. Chen, H.-C. Scheer, T. Riedl, "Distributed Feedback Lasers Based on $MAPbBr_3$", Adv. Mater. Technol., **2018**, 3, 1700253.

147. S. A. Veldhuis, P. P. Boix, N. Yantara, M. Li, T. C. Sum, N. Mathews, S. G. Mhaisalkar, "Perovskite Materials for Light-Emitting Diodes and Lasers", Adv. Mater., **2016**, 28, 6804.

148. M. L. De Giorgi, A. Perulli, N. Yantara, P. P. Boix, M. Anni, "Amplified Spontaneous Emission Properties of Solution Processed $CsPbBr_3$ Perovskite Thin Films", J. Phys. Chem. Lett. C, **2017**, 121, 14772.

149. C. Li, Z. Zang, C. Han, Z. Hu, X. Tang, J. Du, Y. Leng, K. Sun, "Highly compact CsPbBr3 perovskite thin films decorated by ZnO nanoparticles for enhanced random lasing", Nano Energy, **2017**, 40, 195.

150. X. Zhang, Z. Jin, J. Zhang, D. Bai, H. Bian, K. Wang, J. Sun, Q. Wang, S. F. Liu, "All-Ambient Processed Binary $CsPbBr_3$−$CsPb_2Br_5$ Perovskites with Synergistic Enhancement for High-Efficiency Cs−Pb−Br-Based Solar Cells", ACS Appl. Mater. Interfaces, **2018**, 10, 7145.

151. C. Zhao, W. Tian, J. Liu, Q. Sun, J. Luo, H. Yuan, B. Gai, J. Tang, J. Guo, S. Jin, "Stable Two-Photon Pumped Amplified Spontaneous Emission from Millimeter-sized CsPbBr3 Single Crystals", J. Phys. Chem. Lett., **2019**, 10, 2357.

152. S. Yakunin, L. Protesescu, F. Krieg, M. I. Bodnarchuk, G. Nedelcu, M. Humer, G. De Luca, M. Fiebig, W. Heiss, M. V. Kovalenko, " Low-threshold amplified spontaneous emission and lasing from colloidal nanocrystals of caesium lead halide perovskites", Nat. Commun., **2015**, 6, 8056.

153. S. Kondo, K. Takahashi, T. Nakanish, T. Saito, H. Asada, H. Nakagawa, " High intensity photoluminescence of microcrystalline CsPbBr3 films: Evidence for enhanced stimulated emission at room temperature", Current Appl. Phys., **2007**, 7, 1.

154. Y. Fu, H. Zhu, C. C. Stoumpos, Q. Ding, J. Wang, M. G. Kanatzidis, X. Zhu, S. Jin, "Broad Wavelength Tunable Robust Lasing from Single-Crystal Nanowires of Cesium Lead Halide Perovskites ($CsPbX_3$, X = Cl, Br, I)", ACS Nano, **2016**, 10, 7963.

155. Q. Sun, P. Fassl, D. Becker-Koch, A. Bausch, B. Rivkin, S. Bai, P. E. Hopkinson, H. J. Snaith, Y. Vaynzof, "Role of Microstructure in Oxygen Induced Photodegradation of Methylammonium Lead Triiodide Perovskite Films", Adv. Energy Mater., **2017**, 7, 1700977.

156. H. Huang, M. I. Bodnarchuk, S. V. Kershaw, M. V. Kovalenko, A. L. Rogach, "Lead Halide Perovskite Nanocrystals in the Research Spotlight: Stability and Defect Tolerance", ACS Energy Lett., **2017**, 2, 2071.

157. M. Cadelano, V. Sarritzu, N. Sestu, D. Marongiu, F. Chen, R. Piras, R. Corpino, C. M. Carbonaro, F. Quochi, M. Saba, A. Mura, G. Bongiovanni, "Can trihalide lead perovskites support continuous wave lasing?", Adv. Opt. Mater., **2015**, 3, 1557.

158. Z. Xiao, R. A. Kerner, L. Zhao, N. L. Tran, K. M. Lee, T.-W. Koh, G. D. Scholes, B. P. Rand, "Efficient perovskite light-emitting diodes featuring nanometre-sized crystallites", Nature Photonics, **2017**, 11, 108.

159. B. Turedi, K. J. Lee, I. Dursun, B. Alamer, Z. Wu, E. Alarousu, O. F. Mohammed, N. Cho, O. M. Bakr, "Water-Induced Dimensionality Reduction in Metal-Halide Perovskites", The Journal of Physical Chemistry C, **2018**, 122, 14128.

160. T. Haeger, M. Wilmes, R. Heiderhoff, T. Riedl, "Simultaneous Mapping of Thermal Conductivity, Thermal Diffusivity, and Volumetric Heat Capacity of Halide Perovskite ThinFilms: A Novel Nanoscopic Thermal Measurement Technique", The Journal of Physical Chemistry Letters, **2019**, 10, 3019.

161. I. Dursun, M. De Bastiani, B. Turedi, B. Alamer, A. Shkurenko, J. Yin, A. M. El-Zohry, I. Gereige, A. AlSaggaf, O. F. Mohammed, M. Eddaoudi, O. M. Bakr, "$CsPb_2Br_5$ Single Crystals: Synthesis and Characterization", ChemSusChem, **2017**, 10, 3746.

162. G. Li, H. Wang, Z. Zhu, Y. Chang, T. Zhang, Z. Song, Y. Jiang, "Shape and phase evolution from $CsPbBr_3$ perovskite nanocubes to tetragonal $CsPb_2Br_5$ nanosheets with an indirect bandgap", ChemComm., **2016**, 52, 11296.

163. Y. Rakita, N. Kedem, S. Gupta, A. Sadhanala, V. Kalchenko, M. L. Böhm, M. Kulbak, R. H. Friend, D. Cahen, G. Hodes, "Low-Temperature Solution-Grown $CsPbBr_3$ Single Crystals and Their Characterization Crystal Growth & Design", **2016**, 16, 5717.

164. J. Song, Q. Cui, J. Li, J. Xu, Y. Wang, L. Xu, J. Xue, Y. Dong, T. Tian, H. Sun, H. Zeng, "Ultralarge All-Inorganic Perovskite Bulk Single Crystal for High-Performance Visible–Infrared Dual-Modal Photodetectors ", Adv. Opt. Mater., **2017**, 5, 1700157.

165. X. Li, Y. Wu, S. Zhang, B. Cai, Y. Gu, J. Song, H. Zeng, "$CsPbX_3$ Quantum Dots for Lighting and Displays: RoomTemperature Synthesis, Photoluminescence Superiorities, Underlying Origins and White Light-Emitting Diodes", Adv. Funct. Mater., **2016**, 26, 2435.

166. J. Wang, E. Motaharifar, L. N. S. Murthy, M. Higgins, D. Barrera, T. B. Daunis, Y. Zheng, A. V. Malko, F. Ely, M. Quevedo-Lopez, M. Lee, J. W. P. Hsu, "Revealing lattice and photocarrier dynamics of high-quality $MAPbBr_3$ single crystals by far infrared reflection and surface photovoltage spectroscopy", J. Appl. Phys., **2019**, 125, 025706.

167. H. Shi, X. Zhang, X. Sun, X. Zhang, "Phonon mode transformation in size-evolved solution-processed inorganic lead halide perovskite", Nanoscale, **2018**, 10, 9892.

168. O. Yaffe, Y. Guo, L. Z. Tan, D. A. Egger, T. Hull, C. C. Stoumpos, F. Zheng, T. F. Heinz, L. Kronik, M. G. Kanatzidis, J. S. Owen, A. M. Rappe, M. A. Pimenta, L. E. Brus, "Local Polar Fluctuations in Lead Halide Perovskite Crystals", Phys. Rev. Lett., **2017**, 118, 136001.

169. C.-Y. Huang, C. Zou, C. Mao, K. L. Corp, Y.-C. Yao, Y.-J. Lee, C. W. Schlenker, A. K. Y. Jen, L. Y. Lin, "CsPbBr3 Perovskite Quantum Dot Vertical Cavity Lasers with Low Threshold and High Stability", ACS Photonics, **2017**, 4, 2281.

170. Y. Wang, X. Li, V. Nalla, H. Zeng, H. Sun, "Solution-Processed Low Threshold Vertical Cavity Surface Emitting Lasers from All-Inorganic Perovskite Nanocrystals ", Adv. Funct. Mater., **2017**, 27, 1605088.

171. A. Mayer, S. Moellenbeck, K. Dhima, S. Wang, H.-C. Scheer, "A novel tool for frequency assisted thermal nanoimprint (T-NIL)", J. Vac. B Sci. Technol. B, **2011**, 29, 06FC13.

172. A. M. A. Leguy, Y. Hu, M. Campoy-Quiles, M. I. Alonso, O. J. Weber, P. Azarhoosh, M. van Schilfgaarde, M. T. Weller, T. Bein, J. Nelson, P. Docampo, P. R. F. Barnes, "Reversible Hydration of $CH_3NH_3PbI_3$ in Films, Single Crystals, and Solar Cells", Chem. Mater., **2015**, 27, 3397.

173. Y. Han, S. Meyer, Y. Dkhissi, K. Weber, J. M. Pringle, U. Bach, L. Spiccia, Y. B Cheng, "Degradation observations of encapsulated planar $CH_3NH_3PbI_3$ perovskite solar cells at high temperatures and humidity", J. Mater. Chem. A, **2015,** 3, 8139.

174. Gu. Niu, X.Guo, L. Wang, "Review of recent progress in chemical stability of perovskite solar cells", J. Mater. Chem. A, **2015**, 3, 8970.

175. J. M. Frost, K. T. Butler, F. Brivio, C. H. Hendon, M. van Schilfgaarde, A. Walsh, "Atomistic Origins of High-Performance in Hybrid Halide Perovskite Solar Cells", Nano Lett., **2014**, 14, 2584.

176. J. Yang, B. D. Siempelkamp, D. Liu, T. L. Kelly, "Investigation of $CH_3NH_3PbI_3$ Degradation Rates and Mechanisms in Controlled Humidity Environments Using in Situ Techniques", ACS Nano, **2015**, 9, 1955.

177. K.O. Brinkmann, J. Zhao, N. Pourdavoud, T. Becker, T. Hu, S. Olthof, K. Meerholz, L. Hoffmann, T. Gahlmann, R. Heiderhoff, M.F. Oszajca, N.A. Luechinger, D. Rogalla, Y. Chen, B. Cheng, T. Riedl, "Suppressed decomposition of organometal halide perovskites by impermeable electron-extraction layers in inverted solar cells", Nat. Commun., **2017**, 8, 13938.

178. A. Mayer, M. Buchmueller, S. Wang, C. Steinberg, M. Papenheim, N. Pourdavoud, T. Haeger, T. Riedl, H.-C. Scheer, "Thermal nanoimprint to improve the morphology of $MAPbX_3$ (MA=methylammonium, X=I or Br)", Vac. Sci. Technol. B, **2017**, 35, 6.

179. C. Steinberg, K. Dhima, D. Blenskens, A. Mayer, S. Wang, M. Papenheim, H.-C. Scheer, J. Zajadacz, K. Zimmer, "A scalable anti-sticking layer process via controlled evaporation", Microelectron. Eng., **2014**, 123, 4.

180. M. Papenheim, C. Steinberg, K. Dhima, S. Wang, H.-C. Scheer, "Flexible composite stamp for thermal nanoimprint lithography based on Ormo Stamp", J. Vac. Sci. Technol., B: Nanotechnol. Microelectron: Mater., Process., Meas., Phenom., **2015**, 33, 06F601.

Author's Publications and Conference Contributions

Publications

1. C. Kriso, M. Stein, T. Haeger, **N. Pourdavoud**, M. Gerhard, Arash R.-I., T. Riedl, M. Koch, "Nonlinear refraction in CH3NH3PbBr3 single crystals", Optics Lett., **2020**, 45, 2431.

2. T. Haeger, M. Ketterer, J. Bahr, N. Pourdavoud, M. Runkel, R. Heiderhoff, T. Riedl, "Thermal properties of $CsPbCl_3$ thin films across phase transitions", J. Phys. Mater., **2020**, 3, 024004.

3. **N. Pourdavoud**, T. Haeger, A. Mayer, P. J. Cegielski, A. L. Giesecke, R. Heiderhoff, S. Olthof, S. Zaefferer, I. Shutsko, A. Henkel, D. Becker-Koch, M. Stein, M. Cehovski, O. Charfi, H.-H. Johannes, D. Rogalla, M. Lemme, M. Koch, Y. Vaynzof, K. Meerholz, W. Kowalsky, H.-C. Scheer, P. Görrn, and T. Riedl, "Room Temperature Stimulated Emission and Lasing in Recrystallized Cesium Lead Bromide Perovskite Thin Films", Adv. Mater., **2019**, 31, 1903717.

4. **N. Pourdavoud**, A. Mayer, M. Buchmüller, K. Brinkmann, T. Häger, T. Hu, R. Heiderhoff, I. Shutsko, P. Görrn, Y. Chen, H.-C. Scheer, and T. Riedl, "Distributed Feedback Lasers Based on $MAPbBr_3$", Adv. Mater. Technol., **2018**, 3, 1700253.

5. **N. Pourdavoud**, S. Wang, A. Mayer, T. Hu, Y. Chen, A. Marianovich, W. Kowalsky, R. Heiderhoff, H.-C. Scheer, and T. Riedl, "Photonic Nanostructures

Patterned by Thermal Nanoimprint Directly into Organo-Metal Halide Perovskites", Adv. Mater., **2017**, 29, 1605003.

6. R. Heiderhoff, T. Haeger, **N. Pourdavoud**, T. Hu, M. Al-Khafaji, A. Mayer, Y. Chen, H.-C. Scheer, and T. Riedl, "Thermal Conductivity of Methylammonium Lead Halide Perovskite Single Crystals and Thin Films – A Comparative Study", J. Phys. Chem. C, **2017**, 121, 28306.

7. T. Hu, T. Becker, **N. Pourdavoud**, J. Zhao, K. Brinkmann, R. Heiderhoff, T. Gahlmann, Z. Huang, S. Olthof, K. Meerholz, D. Többens, B. Cheng, Y. Chen, and T. Riedl, "Indium-Free Perovskite Solar Cells Enabled by Impermeable Tin-Oxide Electron Extraction Layers", Adv. Mater., **2017**, 29, 1606656.

8. J. Zhao, K. Brinkmann, T. Hu, **N. Pourdavoud**, T. Becker, T. Gahlmann, R. Heiderhoff, A. Polywka, P. Görrn, Y. Chen, B. Cheng, and T. Riedl, "Self-Encapsulating Thermostable and Air-Resilient Semitransparent Perovskite Solar Cells", Adv. Energy Mater., **2017**, 7, 1602599.

9. K. Brinkmann, J. Zhao, **N. Pourdavoud**, T. Becker, T. Hu, S. Olthof, K. Meerholz, L. Hoffmann, T. Gahlmann, R. Heiderhoff, M. F. Oszajca, N. A. Luechinger, D. Rogalla, Y. Chen, B. Cheng, and T. Riedl, "Suppressed decomposition of organo-metal halide perovskites by impermeable electron extraction layers in inverted solar cells", Nat. Commun., **2017**, 7, 13938.

10. A. Mayer, M. Buchmüller, S. Wang, C. Steinberg, M. Papenheim, H.-C. Scheer, **N. Pourdavoud**, T. Haeger, and T. Riedl, "Thermal nanoimprint to improve the morphology of $MAPbX_3$", J. Vac. Sci. & Technol. B, **2017**, 35, 06G803.

11. J. Emara, T. Schnier, **N. Pourdavoud**, T. Riedl, K. Meerholz, and S. Olthof, "Impact of Film Stoichiometry on the Ionization Energy and Electronic Structure of $CH_3NH_3PbI_3$ Perovskite", Adv. Mater., **2016**, 28, 553.

Conference contributions

1. T. Haeger, M. Wilmes, J. Bahr, N. Pourdavoud, S. Zaefferer, R. Heiderhoff , T. Riedl, "Thermal properties of highly oriented all-inorganic $CsPbX_3$ (X=Br, Cl) perovskite films dependence on halide, dimensionality, and crystal-phase", MRS (Fall Meeting), Boston (USA), EN09.15.02, **2019**.

2. Mayer, N. Pourdavoud, T. Haeger, R. Heiderhoff, M. Leifels, J. Rond, J. Staabs, P. Görrn, T. Riedl, H. Scheer, "Imprint-induced grain growth in perovskite layers", 45th International Conference on Micro & Nano Engineering, Rhodes (Greece), **2019**.

3. T. Haeger, M. Ketterer, **N. Pourdavoud**, R. Heiderhoff, T. Riedl T, "Thermal properties of all-inorganic halide perovskites: dependence on dimensionality and crystal-phase", EMRS (Fall Meeting), Warsaw (Poland), T.9.1, **2019**.

4. A. Mayer, **N. Pourdavoud**, T. Haeger, R. Heiderhoff, M. Leifels, J. Rond, J. Staabs, P. Görrn, T. Riedl, H-C Scheer, "Imprint-induced grain growth in perovskite layers", NNT, Boston (USA), **2019**.

5. A. Mayer, **N. Pourdavoud**, T. Haeger, R. Heiderhoff, M. Leifels, J. Rond, J. Staabs, P. Görrn, T. Riedl, H-C Scheer, "Imprint-induced grain growth in perovskite layers", poster presentation, MNE, Rhodes (Greece), **2019**.

6. A. Mayer, **N. Pourdavoud**, J. Staabs, J. Rond, M. Leifels, R. Heiderhoff, P. Görrn, T. Riedl, H.-C Scheer, "Characteristics of thermal imprint with perovskite layers", The 63rd International Conference on Electron, Ion, and Photon Beam Technology and Nanofabrication, Hyatt Regency Minneapolis (USA), **2019**.

7. **N. Pourdavoud**, A. Mayer, T. Haeger, R. Heiderhoff, I. Shutsko, H.-C. Scheer, P. Görrn, and T. Riedl, "Ultra-smooth perovskite thin films for lasers", **Invited** , SPIE, San Diego (USA), 107240C, **2018**.

8. T. Haeger, M. Wilmes, **N. Pourdavoud**, R. Heiderhoff, and T. Riedl, "Mapping the low thermal conductivity of lead-halide based perovskite films with high spatial resolution", MRS (Fall Meeting), Boston (USA), TP02, **2018**.

9. **N. Pourdavoud**, A. Mayer, S. Wang, T. Hu, J. Zhao, K. Brinkmann, R. Heiderhoff, A. Marianovich, W. Kowalsky, H.-C. Scheer, T. Riedl, "Photonic nanopatterns in organo-metal halide perovskites by thermal nanoimprint lithography", **Invited paper,** SPIE, Physical Chemistry of Semiconductor Materials and Interfaces XVI, San Diego (USA), Paper 10348-31, **2017**.

10. **N. Pourdavoud**, A. Mayer, S. Wang, T. Hu, J. Zhou, K. Brinkmann, R. Heiderhoff, A. Marianowich, H.-C. Scheer, T. Riedl, "Photonic nanopatterns in organo-metal halide perovskites by thermal nanoimprint lithography", **Invited**, SPIE, San Diego (USA) 10363-32, **2017**.

11. **N. Pourdavoud**, A. Mayer, S. Wang ,M. Buchmüller, K. Brinkmann, T. Haeger, T. Hu, R. Heiderhoff, A. Marianovich, I. Shutsko, P. Görrn,Y. Chen, W.

Kowalsky, H.-C. Scheer, T. Riedl, "Low-threshold Distributed Feedback Lasers Prepared By Direct Thermal Nanoimprint Of Resonator Gratings Into Organo-metal Halide Perovskites", **Best Student Paper Award**, Nature Photonics, Photonics @ SG, Singapore, 3-1D-5, **2017**.

12. **N. Pourdavoud**, A. Mayer, R. Heiderhoff, H.C. Scheer, T. Riedl, "NIR Lasing in Hybrid Metal-Halide Perovskites", **Invited**, E-MRS (Fall Meeting), Warsaw (Poland), R02.1, **2017**.

13. **N. Pourdavoud**, A. Mayer, M. Buchmüller, K. Brinkmann, T. Häger, T. Hu, R. Heiderhoff, I. Shutsko, P. Görrn, Y. Chen, H.-C. Scheer, and T. Riedl, "Low-Threshold Distributed Feedback Lasers Based on Thermally Imprinted $MAPbBr_3$", MRS (Fall Meeting), Boston (USA), ES01.12.09, **2017**.

14. K. O. Brinkmann, J. Zhao, T. Hu, **N. Pourdavoud**, T. Gahlmann, R. Heiderhoff, S. Olthof, K. Meerholz, A. Polywka, B. Cheng, Y. Chen, P. Görn, and T. Riedl, "Self-Encapsulating Air-Resilent Semitransparent Perovskite Solar Cells with Superior Thermal Stability Beyond 2000h", MRS (Spring Meeting), Phoenix (USA), ES1.2.10, **2017**.

15. K. O. Brinkmann, J. Zhao, T. Hu, T. Becker, **N. Pourdavoud**, S. Olthof, K. Meerholz, L. Hoffmann, T. Gahlmann, R. Heiderhoff, M. Oszajca, D. Rogalla, N. A. Lüchinger, Y. Chen, B. Cheng, T. Riedl: "Pushing the lifetime of perovskite solar cell beyond 4500 h by the use of impermeable tin oxide electron extraction layers", SPIE, San Diego (USA), 10363-32, **2017**.

16. K. O. Brinkmann, T. Hu, T. Becker, **N. Pourdavoud**, J. Zhao, R. Heiderhoff, T. Gahlmann, Z. Huang, S. Olthof, K. Meerholz, D. Többens, B. Cheng, Y. Chen, T. Riedl: "Interface Electronic Structure of ALD-Grown SnOx and MAPbI3 in In-Free Perovskite Solar Cells", ISOS-10, Malta, ID13, **2017**.

17. **N. Pourdavoud**, S. Wang, A. Mayer, T. Hu, Y. Chen, R. Heiderhoff, H.-C. Scheer, and T. Riedl, "Low-Threshold Perovskite Distributed Feedback Lasers Based on the Direct Thermal Nanoimprint of Two-Dimensional Photonic Gratings into Methyl-Ammonium Iodide", **Best Poster Award Nomination**, MRS (Fall Meeting), Boston (USA), NM4.5.10, **2016**.

18. K. Brinkmann, **N. Pourdavoud**, T. Becker, T. Hu, J. Zhao, Y. Chen, S. Olthof, K. Meerholz, L. Hoffmann, T. Gahlmann, R. Heiderhoff, M. Oszajca, N. Luechinger, and T. Riedl, "Suppressed Decomposition of Organo-Metal Halide Perovskites by Impermeable Electron Extraction Layers in Inverted Solar Cells", **Best Poster Award Winner**, MRS (Fall Meeting), Boston (USA), ES3.9.09, **2016**.

19. **N. Pourdavoud**, and T. Riedl, "Losses, gain, and lasing in organic and perovskite active materials", **Invited**, Proc. SPIE 9941, 99411G, **2016**.

20. **N. Pourdavoud**, K.-J. Kass, U. Scherf, A. Polywka, P. Görrn, R. Heiderhoff, T. Riedl, "Structure formation and light emitting properties of organometal halide perovskites prepared by sequential deposition", MRS (Fall Meeting), Boston (USA), W3.02, **2014**.

21. **N. Pourdavoud**, K.-J. Kass, U. Scherf, A. Polywka, P. Görrn, R. Heiderhoff, T. Riedl, "Intense luminescence of mixed organometal halide perovskite nano-crystals prepared in a sequential process", 10th Int. Conf. on Electroluminescence and Optoelectronic Devices, ICEL-10, Cologne (Germany), P-2.402, **2014**.

Supervised Student Thesis

1. Felix Talmond: Two step processing of thick mixed halide perovskite layers for thin film solar cells, Bachelor thesis (**2015**).

Appendix A

Experimental Data

A.1. Substrate cleaning

Borofloat glass substrates are used for the lasers and XRD, and silicon wafers for SEM, EBSD, and RBS characterization. For PLQY measurements, silicon wafers with 1.5 µm of thermal oxide on top are used. For PDS and THz spectroscopy, quartz substrates are used. In **Chapter 3**, ITO coated glass substrates are used for SEM measurements

For deposition of $CH_3NH_3PbI_{3-x}Cl_x$ NCs, and $MAPbI_3$, and $MAPbBr_3$ thin films, all substrates are cleaned by sonication in acetone for 5 min and then rinsing in isopropanol. After a further sonication in citric acid for another 5 min, the samples are rinsed in distilled water and isopropanol. After drying the substrates, they are transferred to a nitrogen-filled glovebox. Except samples used for $CH_3NH_3PbI_{3-x}Cl_x$ NCs, other samples are heated for 15 min at 100 °C on a hot-plate. They are then cooled down to room temperature before deposition of the perovskite. For $CsPbBr_3$ deposition, the substrates are cleaned by sonication in citric acid, deionized water, and isopropanol sequentially, each for 15 min. After being dried, the substrates are transferred to a nitrogen-filled glovebox.

A.2. Perovskite deposition

$CH_3NH_3PbI_{3-x}Cl_x$ NCs formation

I first evaporate a thin layer of lead iodide (PbI_2) or lead chloride ($PbCl_2$) in an evaporation chamber inside a nitrogen-filled glovebox and subsequently form perovskite NCs by immersing the layer in an alcoholic anhydrous methylammonium iodide (CH_3NH_3I) solution (10 mg CH_3NH_3I (Solaronix) dissolved in 1ml anhydrous Isopropanol); the immersing time depends on the thickness of the evaporated lead halide layer. After immersion, the perovskite film is heated at 70ºC on a hotplate for 10 min for final crystallization. Note, the whole perovskite deposition process is done in a nitrogen-filled glovebox.

$MAPbI_3$ thin film deposition

For preparing the perovskite precursor, $Pb(Ac)_2$ (purity 99.999%, Sigma-Aldrich), anhydrous CH_3NH_3I (purity >98%, Dyesol), and DMF (purity 99.9%, Sigma-Aldrich) are used. The perovskite solution is prepared by mixing 3:1 (molar ratio) of CH_3NH_3I:$Pb(OAc)_2$ in anhydrous DMF (35 wt%) in a nitrogen-filled glovebox. The solution is then stirred and heated at 60 °C for 1 h, and cooled down inside the glovebox to room temperature. The perovskite layers are prepared by spin-coating the precursor solution at 4000 r.p.m, for 30 s. After spin-coating, the films are annealed on a hotplate at 100 °C for 10 min for evaporation of remained DMF within perovskite film and therefore, final crystallization.

TOPO passivation

For TOPO passivation, a solution of 0.008 m TOPO in anhydrous chlorobenzene was prepared. After the formation of the perovskite layer, 70 μL of the TOPO solution was spin coated at 2000 rpm for 60 s onto the perovskite layer.

$MAPbBr_3$ thin film deposition

$Pb(Ac)_2$ (purity 99.999%, Sigma-Aldrich) and CH_3NH_3Br (Dyesol) are dissolved in anhydrous DMF (purity 99.9%, Sigma-Aldrich) with a 3:1 molar ratio of CH_3NH_3Br:$Pb(Ac)_2$, and then stirred and heated over night at 60 °C in a nitrogen-filled glovebox, and the next day, they are cooled down to room temperature. The perovskite layers are prepared by spin-coating the precursor solution at 5000 r.p.m, for 3 min. After spin-coating, the films are annealed on a hotplate at 100 °C for 2 min.

$CsPbBr_3$ thin film deposition

The pristine caesium lead bromide thin films used in this study are prepared by a spin-coating process. $PbBr_2$ (purity 99.999%, ultradry, Alfa Aeser) and CsBr (99.999%, trace metal basis, Sigma-Aldrich) are dissolved in anhydrous DMSO with molar ratio of CsBr to $PbBr_2$ varied between 0.5:1 and 3:1. The perovskite precursor is then stirred and heated overnight at 60^{o}C in a nitrogen-filled glovebox. The next day, the solution should rest for about 1 hour, and then the upper transparent part of the solution is filtered by 0.2 μm filter inside the glovebox. The perovskite precursor is spin-coated on substrates at 4000 rpm, for 120s, with 11s ramp. As the last step, the spin-coated films are annealed at 100^{o}C on a hotplate for 20 min for final crystallization.

A.3. Thermal nanoimprint and planar hot pressing process

Thermal nanoimprint and planar hot pressing processes are performed in the same parallel plate-based imprint system for all perovskite thin films. This system consists of a piezo system (including ceramic piezo actors and three piezo force sensors), two parallel hotplates (the lower hotplate sits on the piezo system), and a stepper motor [171].

The stamp sits on top of the sample which needs to be imprinted or flattened, and both of them are placed between two cushion layers, a combination of a 200 μm thick thermally conductive foil (KU-CG30/R, Kunze) and a 50 μm thick Aluminium sheet (EN AW-1050A, 0/H111, Alujet Universal) and the final stack is located on the lower hotplate.

Applying the static force provided by the stepper motor, the upper hotplate moves downward with defined acceleration and speed. The piezo actors adjust the parallelization of the two hotplates by driving them separately into a position where a similar force is measured for each of the three piezo sensors. When the upper hotplate gets in touch with the stack, the sample is heated up to a specified temperature. The stack is kept under constant temperature and pressure for an adjusted time. After that time, the system is cooled down to about 30 °C, and the upper hotplate gets released. Separation of stamp and sample after finishing the imprint process is performed manually by carefully inserting a razor blade along the periphery.

Note, the whole imprinting process is done in ambient air. Therefore, as typical organometal halide perovskites such as $MAPbI_3$ degrade in humid air [120, 172-176], after preparing the perovskite thin films in a nitrogen-filled glovebox, the samples are packed in a nitrogen-filled box, sealed and transferred to the imprinting laboratory. However, the samples are exposed to air for a very short time over being placed into the imprinting machine. During the imprinting process, the samples are under high pressure where stamp and substrate function as permeation barriers (**Figure A.3.1a**), confining the decomposition products, such as MAI, MA, and etc., within the perovskite layer, and therefore, the equilibrium of decomposition/formation reaction would stabilize the perovskite [177]. As an example, in **Figure A.3.1b**, you can see a photograph of the imprinted grating , which is taken under oblique white-light. The brown colour is the part of the sample which was under pressure from the imprinting machine over the imprinting process, and the yellow part was exposed to ambient air which is decomposed to PbI_2, and CH_3NH_3I.

Note, the adjusted imprinting and hot pressing temperatures, and pressures are the optimal parameters, in order to achieve the highest imprinting quality without decomposing the perovskites, which at the end result in achieving the lowest lasing threshold [178].

The stamps used for imprinting consist of a backplane of 500 µm thick Si and an ≈20 µm thick patterned top layer from Ormostamp (microresist, Berlin) [179, 180], and the stamp surface is functionalized with an antisticking layer in a gas-phase process. For planar hot pressing the stamp was unpatterned silicon, again provided with an antisticking layer.

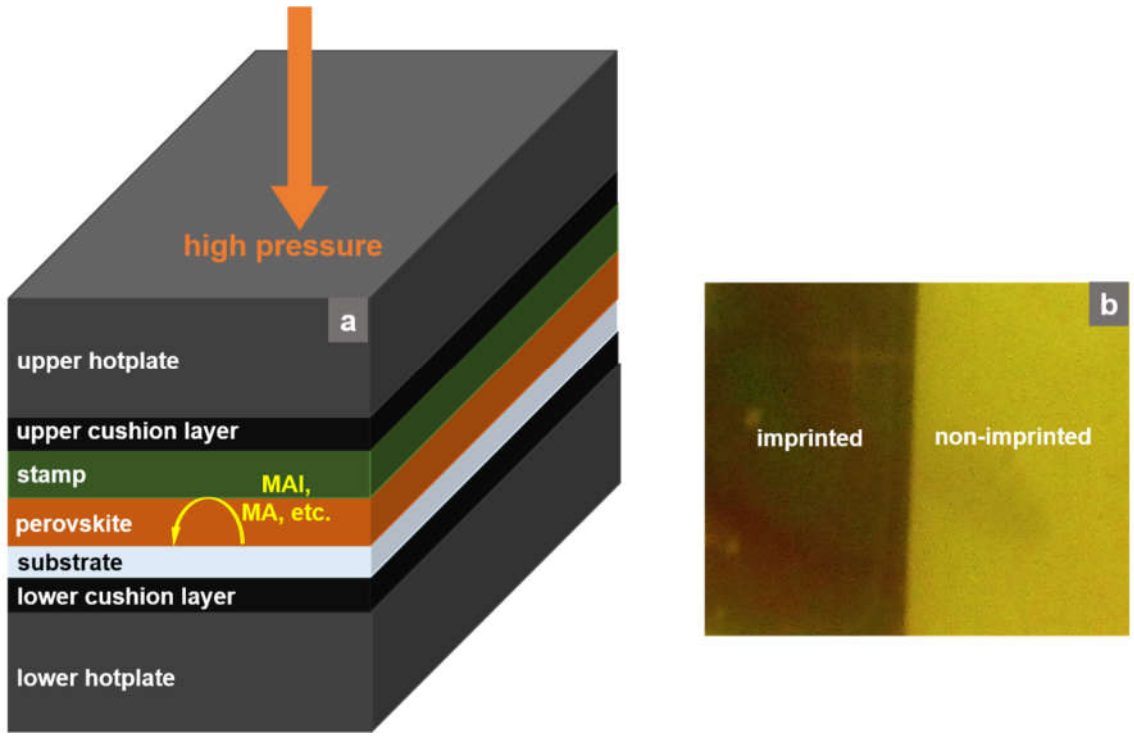

***Figure A.3.1**. a) A schematic of the imprinting system; showing that the application of a high pressure through the movement of the upper hotplate, in which the stamp and substrate function act as a permeation barrier, confines the decomposition products (MAI, MA, etc.) of the perovskite. b) A photograph of the partially imprinted $MAPbI_3$ under oblique while-light illumination.*

NIL of methylammonium lead iodide

The thermal imprint process follows the protocol shown in **Figure 4.2.2**. The starting pressure when the upper hotplate touches the stack is set to 25 bar, under which, temperature rises to 100 °C. When the desired temperature is reached, the pressure increases to 100bar, and the sample is kept under a constant temperature of 100 °C, and pressure of 100 bar for 15 min. Then, the system is cooled down to 30 °C, the upper hotplate gets released, and the sample is separated from the stamp.

NIL of methylaamonium lead bromide

The imprint procedure follows a temperature/pressure sequence presented in **Figure 5.3.2**. During the heat-up of the system to the processing temperature, which in this case,

takes about 10 min, a pre-pressure of 25 bar is applied. When the imprint temperature is reached, the pressure is raised to 100 bar. After an imprint time of 3 min, while keeping the pressure at 100 bar, the system is cooled down to about 30 °C, the upper hotplate gets released, and the sample is separated from stamp. The planar hot pressing procedure follows the same protocol except the temperature which is set to 150 °C for this special presented example. Note, no noticeable variation of optical properties is observed for temperatures in the range of 100 to 150 °C.

NIL of caesium lead bromide

The imprint procedure and planar hot pressing follows a temperature/pressure sequence presented in **Figure 6.3.1.** During heat-up of the system to the processing temperature of 150 °C, which, in this case, takes about 20 min, the pressure of 100 bar is applied. When the imprint and hot pressing temperature is reached, the pressure is kept constant for 5 min. Thereafter, the system is cooled down and the pressure is released slowly as soon as the temperature gets below 30 °C.

Thermal nanoimprinting processes were done by **Dr. Si Wang**, **Dr. André Maye**, and **Andreas Henkel** (Chair of Large Area Optoelectronics, University of Wuppertal)

A.4. Measurements

PL:

In this work, the PL signal was coupled into a monochromator (Princeton Instruments, Acton SP2500) via a multimode optical fiber, and spectrally dispersed light was detected by a thermoelectrically cooled charge coupled device camera (Princeton Instruments). Typically, a 300 lines mm^{-1} grating was used; only for the high-resolution spectra a grating with 1200 lines mm^{-1} was chosen.

***SEM**:*

A Philips XL30S FEG microscope with a field emission cathode was used for SEM measurements.

AFM:

For **$MAPbI_3$** layers in **Chapter 4**, AFM measurement was done by Sylwia Adamczyk from the Macromolecular Chemistry Group (University of Wuppertal, Germany).

For **$MAPbBr_3$** and **$CsPbBr_3$** thin films, AFM measurements were conducted in our group (by **Kai Brinkmann** and **Tobias Haeger**) with a Bruker Innova system in tapping mode (tip: RTESPA-300; tip radius: <12 nm).

XRD:

$MAPbI_{3-x}Cl_x$, and **$MAPbI_3$** layers in **Chapters 3**, and **4**: Layer crystallinity was assessed by XRD using a monochromatic Cu Kα1, 2- source (Philips X'Pert Pro MPD).

$MAPbBr_3$: X-ray diffraction (XRD) was measured using a Cu Kα1, 2-source with Ni filter in a Bruker D2 Phaser system. Alternatively, a Philips X'Pert Pro MPD system with a monochromatic Cu-Kα1, 2-source was used.

$CsPbBr_3$: XRD was measured using a Panalytical Empyrean system with a Cu Kα anode (λ = 1.54056 Å).

The **XRD** measurements were conducted by the support of **Jan-Christoph Gasse** and **Prof. Dirk Lützenkirchen-Hecht** (Condensed Matter Physics, University of Wuppertal), **Dr. Irma Päschke** (Lehrstuhl für Neue Fertigungstechnologien und Werkstoffe, University of Wuppertal), and **Dr. Selina Olthof** (Department of Chemistry, University of Cologne).

Pump laser power and energy density:

Power density was obtained by calculating the area of laser beam using the radius (r) in cm and dividing the beam's power intensity by that area:

$$power\ density(\frac{W}{cm^2}) = \frac{power}{\pi r^2}$$

and then, energy density was calculated by just dividing the power density by the pulse repetition rate. The power intensity (W) of the pump laser was measured with a thermal sensor head (S470C, ThorLabs). To measure the laser beam spot, the laser beam was focused on a piece of graph paper, and its picture is taken by a CCD camera. Then,

The excitation density was varied by placing a neutral density filter wheel in front of the laser.

Time-resolved PL:

$MAPbI_3$ in **Chapter 4**: Time-resolved PL was measured using an actively q-switched diode pumped solid state laser (AOT-YVO-25QSPHP/MOPA, Nd:YVO4, 355 nm) for excitation (pulse width = 600 ps (full width at half maximum), repetition rate 2 kHz). The pulse energy density was 0.2 μJ cm^{-2}.

$CsPbBr_3$: The time-resolved PL measurements were done using a Streak camera (Hamamatsu Streak scope C4334). The samples were optically pumped with a Nd:YVO laser (3^{rd} harmonic, wavelength: 355 nm, pulse width: 700 ps, repetition rate: 1 kHz, energy density: 1.5 μJ cm^{-2}). An optical fiber attached to the Streak camera and a lens system collected a part of the emitted light from the samples.

Time-resolved PL measurements were done by **André Marianovich**, **Marko Cehovski**, and **Ouacef Charfi** (Institut für Hochfrequenztechnik Technische Universität Braunschweig).

Far field measurements:

For the far field measurements of the laser emission, a sand-blasted glass was placed at a distance of about 2-3 cm to the sample surface. The far-field pattern was detected by a Si based complementary metal-oxide semiconductor camera (DCC1545M, ThorLabs) with a 25 mm fixed focal length objective equipped with an optical filter to suppress the excitation laser.

Diffuse reflectance:

$MAPbBr_3$: The diffuse reflectance was measured with an integrating sphere (RTC-060-SF Labsphere) in double beam mode using a fiber-coupled collimated LED light source (MWWHF2, Thorlabs) with an output power of about 16 mW. The spectra in the range from 430 to 670 nm were recorded with an integration time of 8 s and an optical resolution of around 1.9 nm (spectrometer USB 2000+XR1-ES, Ocean Optics). Luminescence of the films (below 630 nm) was blocked with an optical filter.

Diffuse reflectance measurements were done by **Ivan Shutsko** (Chair of Large Area Optoelectronics, University of Wuppertal)

PLQY:

$MAPbBr_3$: The PLQY was measured in an integrating sphere (RTC-060-SF Labsphere) using a focused laser beam (450 nm, 0.286 W cm^{-2}, CPS450, Thorlabs) for excitation. The power was measured with a power meter (PM100USB, Thorlabs). The excitation wavelength was blocked with a low-pass filter (03FCG065, Melles Griot) to selectively detect the PL signal.

$CsPbBr_3$:

External PLQY was measured using a focused continuous wave laser beam (RLDE405M-50-5, Roithner-Lasertechnik, wavelength: 405 nm, power density: 15 W cm^{-2}). As substrates for the perovskite layers, Si wafers covered with 1.5 µm thermal SiO_2 were used. The sample was attached to one of the ports of an integrating sphere (RTC-060-SF, Labsphere). The excitation signal was blocked from entering the detector by a filter (03FCG065, Melles Griot) and the PL signal was detected with a power meter (PM100USB, Thorlabs).

The **PLQY** measurements and calculations were conducted by the support of **Ivan Shutsko** (Chair of Large Area Optoelectronics, University of Wuppertal), and **Dr. Piotr Jacek Cegielski** (AMO GmbH), respectively.

EBSD:

No specific sample preparation was applied. A Bruker nanosystem with an X-flash EBSD camera, installed on a Zeiss Merlin SEM, was used for the measurements. The measurements were done at 30 kV acceleration voltage and 2 nA beam current. The patterns were binned to 160 × 120 pixel size and exposed for 30 ms, resulting in a measurement rate of 33 frames per second. The analysis of the measured maps was carried out using the EDAX/TSL software OIM DC.

EBSD measurements were performed by **Dr. Stefan Zaefferer** (Max-Planck-Institut für Eisenforschung).

Absorption:

Absorption spectra were measured by photothermal deflection spectroscopy (PDS). The samples were submerged in an inert liquid (Fluorinert FC-770), which acts as deflecting medium for a probing laser beam (REO R-31008) of 633 nm wavelength while passes parallel to the samples surface. Its deflection, measured by a position sensitive detector

(Thorlabs PDP90A) amplified by a lock-in amplifier (Ametec 7230), was directly linked to the absorption of the sample, and caused by the heat created from the absorbed pumping light in the sample. The chopped excitation light was provided by a Xenon arc lamp (Ushio 150W with Abet housing) and a subsequent monochromator.

Absorption measurements were performed by **David Becker-Koch** (Kirchhoff-Institut für Physik Ruprecht-Karls-Universität Heidelberg) .

RBS:

RBS was performed at the 4 MV tandem accelerator of the RUBION facility (University of Bochum, Germany). A 2 MeV 4He+ ion beam (beam current of 20–40 nA) in combination with a silicon surface barrier detector at an angle of 160° was used.

RBS measurements were done by the support of **Dr. Detlef Rogalla** (RUBION Ruhr-University Bochum).

THz spectroscopy:

The THz absorption spectroscopy was conducted using the output of a 1 kHz titanium-sapphire-based regenerative amplifier system with 35 fs pulses spectrally centered at 800 nm. The output of the amplifier was split into two parts. One part drove a low-temperature grown large aperture Galliumarsenide antenna, which emitted spectrally broad THz pulses ranging from 0.2 to 3 THz. The THz radiation was focused onto the sample by a pair of parabolic mirrors. The transmitted THz pulse was detected phase-sensitive via electro-optical sampling in an 800 µm thick Zinctelluride crystal by the other part of the amplifier output and autobalanced photodiodes. The beam path of the THz radiation was purged with nitrogen gas to avoid water vapor absorption. Two measurements were performed, one with the pure quartz substrate as the sample ($E_0(t)$) and one with the quartz substrate spin-coated by the perovskite layers (Ep(t)). Fourier

transformation converted the THz pulses into the frequency domain where the absorption can be calculated using:

$$\alpha \sim ln\left(\frac{|E_0(w)|^2}{|E_p(w)|^2}\right)$$

Optical constants were determined by spectroscopic ellipsometry at 75.48° angle (J.A. Wollam M-2000F).

THz measurements were performed by the support of **Markus Stein** (Fachbereich Physik Philipps-Universität Marburg).